Simulation of blood microcirculation and its coupling to biochemical signaling

Hengdi Zhang

Communauté
UNIVERSITÉ Grenoble Alpes

THÈSE

Pour obtenir le grade de

DOCTEUR DE LA COMMUNAUTÉ UNIVERSITÉ GRENOBLE ALPES

Spécialité : Physique pour les Sciences du Vivant

Arrêté ministériel : 25 mai 2016

Présentée par

Hengdi ZHANG

Thèse dirigée par **Chaouqi MISBAH**, CNRS

préparée au sein du **Laboratoire Laboratoire Interdisciplinaire de Physique**
dans **l'École Doctorale Physique**

Simulation de la microcirculation sanguine et son couplage à la signalisation biochimique

Simulation of Blood Microcirculation and Its Coupling to Biochemical Signaling

Thèse soutenue publiquement le **4 décembre 2018**,
devant le jury composé de :

Monsieur MARC LEONETTI
CHARGE DE RECHERCHE, CNRS DELEGATION ALPES, Examinateur
Monsieur JENS HARTING
PROFESSEUR, INSTITUT DE HELMHOLTZ ERLANGEN NÜRNBERG, Rapporteur
Monsieur BENOÎT POLACK
PROFESSEUR DES UNIV - PRATICIEN HOSP., CHU GRENOBLE ALPES, Président
Monsieur TIMM KRÜGER
PROFESSEUR ASSISTANT, UNIVERSITE D'EDIMBOURG - ROYAUME-UNI, Rapporteur
Monsieur ABDUL I BARAKAT
PROFESSEUR, ÉCOLE POLYTECHNIQUE, Invité

Simulation of Blood Microcirculation and its Coupling to Biochemical Signaling

Hengdi Zhang

Laboratoire Interdisciplinaire de Physique

Université Grenoble Alpes

A thesis submitted for the degree of

Doctor of Physics

December 4, 2018

Acknowledgements

I would like to express my gratitude to all those who helped and stood with me during the writing of this thesis.

My sincere gratitude goes first and foremost to Chaouqi Misbah, my supervisor, for his professional guidance, constant encouragement and everlasting patience throughout the research and the writing of this thesis. The great freedom he offered me was always accompanied by wise advice. He was extremely understanding and supportive when I was at rock bottom during the development of numerical method and code. Under the careful guidance on the topic of vesicle dynamics I was able to enter an impressive new world of dynamical system, at where I started to realize how complexity can emerge from even simple rules.

I would like to express my gratitude to Abdul Barakat, for his supports and guidance on the topic of mechanotransduction, I also thank him for the inspirations and encouragement in many fruitful communications. I would like to thank Alexander for his patience in answering my basic and silly questions in boundary integral method and in the code. I thank Philippe for his guidance on using GPU cluster and installation of CUDA.

I would like to thank the referees of my thesis, Jens Harting and Timm Krüger for having accepted this task. I also thank the other members of the defense committee, Marc Léonetti, Benoit Polack and Abdul Barakat.

I express my gratitude to my bachelor supervisor Ying He, who encouraged me to start the journey of biophysics. I also thank my master supervisor Ping Li, who brought me into the field of numerical simulations and high performance computing.

I would like to thank Abdessamad and Suhail for the inspiring discussions on vesicle dynamics. I would like to thank Zaiyi for sharing me extremely helpful experiences in Lattice-Boltzmann Method and vesicle simulation. I also thank Brenna for the fruitful discussions in flow shear stress and the

simulations of chemical dispersion. I thank all my friends from Liphy and outside. Many thanks for the coffee breaks, weekend dinners, interesting discussions and hanging out that I enjoyed with Deepak, Madhav, Zaiyi, Chen, Qiujing, Brenna, Abdessamad, Dongliang, Suhail, Swapnil, Andrey, Keshav and Weifan. Special thanks to Deepak for the careful correction of the thesis manuscript. With these lovely people, my life in Grenoble was happy and colorful. Thank Salima and Kirsten for their frequent concerns on my working progress and well being.

I would like to thank for the financial support from China Scholarship Council, French-German University Programme "Living Fluids" and Campus France. I thank the considerate supports from all my colleagues in Institute of Fluid Physics.

Finally I would like to thank my parents for their constant and unconditional beliefs for me, I am thankful beyond words. I thank with love to Ting Zhou, my wife, who has always stood by my side. We overcame all the harsh difficulties together. All these endeavors would be meaningless without her.

Abstract

Blood flow in microcirculation is vital for oxygen, carbon dioxide and nutrients transport. Most of blood cells are red blood cells (RBCs), so that by blood flow we mean flow of a suspension of RBCs. For long time blood flow has been mainly considered as a passive phenomenon, in which RBCs are viewed as passive carriers of oxygen. The modern view is completely different: blood flow is more active than we thought. The RBCs as well as vascular endothelial cells covering the internal walls of blood vessels are involved in a number of biochemical signaling processes that are triggered by shear stress eliciting a number of biochemical events, and ultimately resulting into vasomotor regulation without participation of the nerve system. For example, RBCs do not only carry oxygen but also ATP (adenosine triphosphate) , the release of which occurs thanks to changes of RBC membrane protein conformations caused by shear stress. Released ATP reacts with some endothelial membrane receptors leading to vasodilation. This thesis is devoted to blood flow and its coupling to biochemical signaling. More precisely, we investigate i) the dynamics of RBCs, ii) the advection diffusion of chemicals in blood flow and the role of iii) the geometry of vessel networks, in the mentioned signaling processes in microcirculations. Firstly, we study the RBC dynamics in a pipe flow with realistic viscosity contrast values, where a link between shape dynamics and rheology is established. Secondly, we develop an advection-diffusion solver that can handle general moving curved boundaries based on lattice-Boltzmann method (LBM); we then implement it for the study of the problem of ATP release from RBCs under shear flow. Membrane tension and deformation induced by shear stress together with vessel network geometry contribute to ATP release. Finally we demonstrate the capability of applying our model and our numerical tool to the complete problem of blood under flow involving ATP release from RBCs and endothelial calcium signaling as a preliminary step to the ambitious task of mechano-involved local regulation events in microcirculation.

Keywords: blood flow, red blood cells, vesicle, rheology, microcirculation, biochemical signaling, advection-diffusion, lattice-Boltzmann method

Résumé

La circulation sanguine joue un rôle vital en microcirculation, et ce pour le transport de l'oxygène, le dioxide de carbone et d'autres nutriments. Les globules rouges (GR) constituent la majorité des cellules du sang, c'est pourquoi par "écoulement sanguin", nous entendrons "écoulement d'une suspension de GR". Pendant longtemps l'écoulement sanguin était vu comme un phénomène passif où les GR sont considérés comme des cargos d'oxygène. La vision moderne est tout autre : l'écoulement sanguin est bel et bien un phénomène actif. Les GR ainsi que les cellules endothéliales (qui tapissent les faces internes des vaisseaux sanguins) sont impliquées dans un grand nombre de signalisations biochimiques induites par les contraintes hydrodynamiques, la route vers des régulations vasomotrices sans l'intervention du système nerveux. Par exemple, les GR ne transportent pas que l'oxygène, mais également de l'ATP (adenosine triphosphate), qui est libérée suite à des changements de conformation de protéines membranaires induite par les contraintes hydrodynamiques. Cette thèse est dédiée à la circulation sanguine et son couplage avec la signalisation biochimique ayant lieu en microcirculation. Plus précisément, les questions traités dans cette thèse sont i) la dynamique des GR, ii) le problème de la diffiusion-advection d'espèces chimiques au sein des écoulements sanguins, et iii) le rôle de la géométrie des réseaux vasculaires dans le processus de la signalisation biochimique mentionnés plus haut. Dans un premier temps nous analysons la dynamique de GR dans un écoulement de Poiseuille en présence de valeurs réalistes de contraste de viscosité. Dans un deuxième temps nous développons un modèle de diffusion-advection et le couplons aux écoulements sanguins en adoptant la méthode de Boltzmann sur réseaux ; nous exploitons ensuite formulation en l'appliquant au problème de la libération de l'ATP par les GR sous écoulement. Enfin nous présentons des résultats préliminaires pour la problématique générale de l'écoulement sanguin mettant en jeu l'ATP libéré par les GR et la signalisation de calcium par les cellules endothéliales. Cette étude constitue un

premier pas vers le problème général et ambitieux de la régulation locale mechano-biochimique impliquée dans la microcirculation.

Mots Clefs : écoulement sanguin, globules rouges, vésicules, rhéologie, microcirculation, signalisation biochimique, advection-diffusion, méthode Boltzmann sur réseau

Contents

List of Figures

Chapter 1

Introduction

1.1 Major Functions and Mechanisms of Circulatory Systems

Transport of oxygen, carbon dioxide, nutrients and metabolic wastes are vital for almost all animals. A straightforward way of transport is, a priori, by diffusion. It is known that for some animals such as flatworms, oxygen and nutrients, indeed, pass through their bodies by simple diffusion thanks to their flattened shapes. When we look at more complex life forms, several sophisticated strategies can be found. For example, in the arthropods, the circulatory system is open, namely one side of the vasculature is in direct contact with air and the other side in contact with organs (Fig. 1.1, middle). In this circulatory system, a solution of oxygen and nutrients (hemolymph) is constantly pumped by heart, the hemolymph is in direct contact with organs. The presence of advection due to hemolymph flow permits the anthropods to enjoy 3D shapes, because it is likely that if only diffusion were operating, then flat shapes would have prevailed. In other words, convection can be viewed as a necessary factor for metabolism of three-dimensional body shapes. Mammals and other vertebrates who have higher demand in consumption of oxygen and nutrients, have more complex circulatory systems. The human circulatory system essentially consists of three parts: a heart that pumps the blood; a hierarchical branching vessel network which is composed of arteries, capillaries and veins that collectively distribute blood into lungs and other organs; the blood, which is a complex fluid mainly consists of red blood cells (RBCs), platelets and immune cells. In fact, RBCs take up around 45% percent of the total volume of the human blood, and this ratio is termed as hematocrit. The adoption of specialized oxygen-carrying cells (RBCs) allows for a higher oxygen concentration and larger diffusivity to tissues. Brief schematics of these

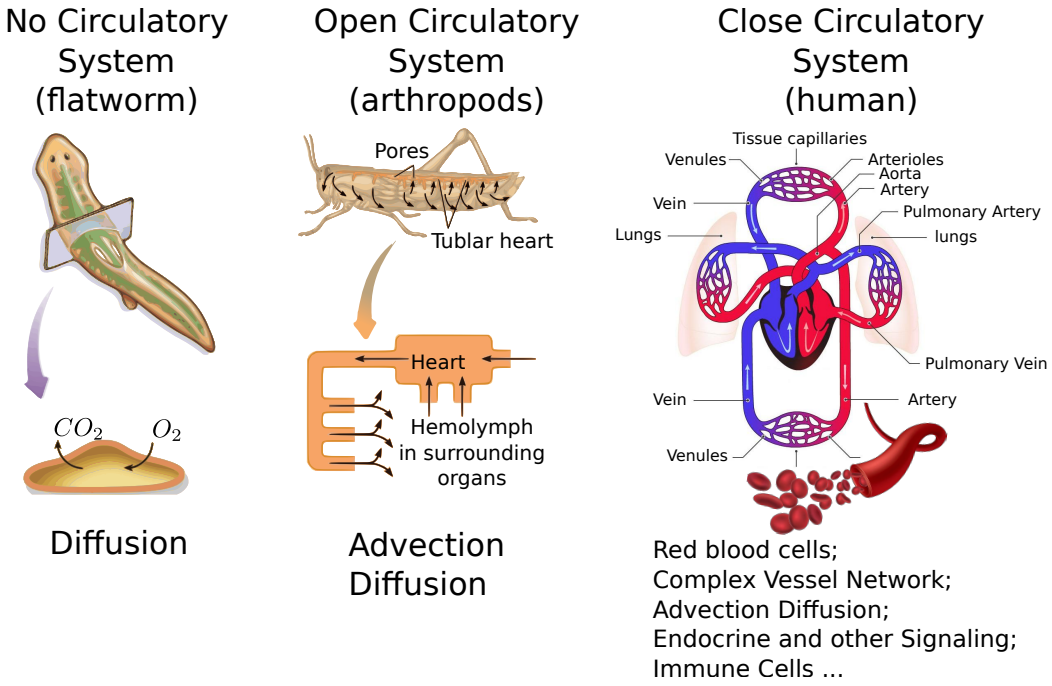

Figure 1.1: Schematics for three different strategies of gas and nutrients transport. Left: flatworms has no circulatory system, a branched cavity formed by digestive system allows direct diffusion of nutrients to cells; Middle: arthropods, exemplified by a grasshopper, posseses an open circulatory system. The hemolymph, as a solution of nutrients and gaseous solutes, is advected all through the body and perfuses the organs via local diffusion; Right: Human circulatory system mainly consists of heart, vessel network and blood. Blood essentially differs from hemolymph by adopting red blood cells as the main oxygen carrier. The colormap represents the relative oxygen level (higher in red and lower in blue). Courtesies of Pearson Education, Inc., www.urgo.co.uk, laoblogger.com and www.netxplica.com

different transport strategies and corresponding mechanisms can be found in Fig. 1.1.

Diffusion as the primary mechanism for transport exists in all three examples. The advection mechanism is introduced with the adoption of an open circulatory system. In human circulatory system, besides advection and diffusion, mechanisms such as RBC dynamics, vessel network, signaling process (e.g. the nitric oxide paracrine signaling pathway that leads to vessel dilation) all come into the picture. The adoption of this complex solution in the human circulatory system endows us with higher efficiency of oxygen delivery and other chemical substances (nutrients, hormones, salts etc.). It also ensures faster metabolism and stronger immune response. At the same time, its complexity raises challenges for understanding its physiology and pathology.

The human circulatory system is closed, which means a RBC always stays in the

blood stream and never leaves the vessel network (during its life time, about 120 days). Fig. 1.1(right) shows a schematic diagram, where we can see that there are two distinct circulations in series. The first one is termed as systemic circulation, which distributes oxygen to tissues throughout the body. In this system, an RBC with high oxygen concentration is propelled out from the left atrium (upper part of the heart labeled in red, see Fig. 1.1(right)), then, it travels through a large spectrum of vessel sizes, branching from aorta (with the diameter around $2cm$) to capillaries (with diameters ranging approximately from 3 to $20\mu m$). In capillaries the RBC delivers most of its oxygen to the surrounding tissues by diffusion, after that it enters the veins and returns to the right ventricle with a low oxygen and high carbon dioxide level, before reaching subsequently the pulmonary circulation. In the pulmonary circulation, a RBC starts from right ventricle, passes through the highly branched alveolars in lung getting oxygenated and returns back to heart again. This circulation has a lower pressure state comparing to the first one as it is dedicated to the process of oxygen inhaling and carbon dioxide exhaling, with the help of respiratory system. In both circulations, the exchange of gases and delivery of nutrients with surrounding tissues are mainly conducted via capillary networks.

1.2 Red Blood Cells in Microcirculation

1.2.1 A Brief Introduction to The Red Blood Cell

Appearance of RBCs in vertebrates is considered as an epoch-making event from the evolutionary point of view [Snyder and Sheafor, 1999]. Although RBCs have diverse properties in different vertebrates, we will limit the introduction to human RBCs. A typical adult human being has around 5 litres of blood, corresponding to 25 trillion RBCs in number. In fact, RBCs account for more than 99% of cells in blood flow, thus these RBCs and the blood plasma dominate the flow properties. A mature human RBC has no nucleus and mitochondria, which implies it doesn't express protein. and thus has more space to accommodate hemoglobin. The hemoglobin is the most prevalent cytoplasmic protein functioning as the oxygen carrier. Thus, cytoplasmic viscosity of RBC is dominated by haemoglobin, its typical value ranges from 2 to 10 $mPa \cdot s$ [Tomaiuolo, 2014]. Blood plasma has a viscosity around 1.3 to 1.7 $mPa \cdot s$ at 37 °C. The RBC has a biconcave disk-like shape when it is relaxed in quiescent blood plasma. Although inflatable under some circumstances, it typically maintains a volume around $90\mu m^3$ and a surface area around $130\mu m^2$ [Tomaiuolo, 2014]. The membrane of a RBC is composed of a lipid-bilayer and a spectrum of network beneath

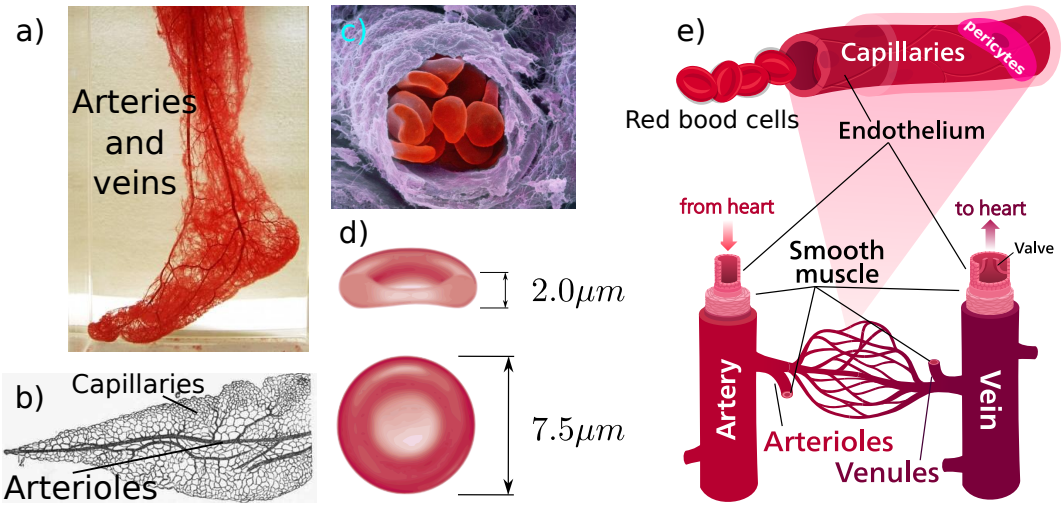

Figure 1.2: Photos of vessel networks scaling from decimeter to micrometer; Schematics showing the dimensions of a typical RBC and the main components of vessel networks. a) The intricate blood vessel networks on human foot, at this scale, arteries with large diameter branch into smaller ones, forming a complex network that adapts the shape of surrounding organs. b) Capillary network in a fat tissue, at this scale, capillaries no longer branch into smaller vessels, instead, they tend to form a dense network with diameters at the same magnitude of RBCs. c) A colored photo from scanning electron microscope, showing RBCs deforming and travelling in an arteriole. d) a schematic plot of a relaxed RBC of typical size with a spontaneous biconcave disk-like shape. e) schematics of vessel network from artery and vein to capillary. The inner most layer of blood vessel is typically covered by a single layer of endothelial cells. Smooth muscles (sphincter) are present on large and intermediate vessels (artery, vein, arterioles, velues, etc.) but not on capillary, devoting to pressure / diameter control. Courtesies of imgur.com, A Manual Of Physiology, ANATOMY and PHYSIOLOGY in Health and Illness and wikipedia.org

it, namely the cytoskeleton [Liu et al., 1987], plus a plethora of transmembrane proteins, and a forest of other elements such as glycocalyx. The lipid-bilayer and cytoskeleton endows RBCs with a bending modulus around $3 \times 10^{-19} J$ [Scheffer et al., 2001, Kaoui et al., 2011] and a shear modulus around $4 \times 10^{-6} N/m$ [Farutin and Misbah, 2012], respectively. A schematic plot and photo from scanning electron microscope of RBCs is shown in Figs. 1.2 c and d.

1.2.2 A Brief Introduction to The Microcirculation

Blood viscosity plays an important role in blood circulation. In principle, low viscosity is preferred in order to have high perfusion rate in the blood vessel when the pressure drop is fixed. However, due to the presence of RBCs (in particular, their

Table 1.1: Typical Total Cross-Section Area and Velocity of Blood flow in Different Vessel Types, Cortesy of wikipedia.org.

Type of blood vessels	Total cross-section area	Blood velocity
Aorta	3 - $5cm^2$	$40cm/s$
Capillaries	4500 - $6000cm^2$	$0.03cm/s$
Vena cavae inferior and superior	$14cm^2$	$15cm/s$

deformability), blood can hardly be treated as a simple fluid with a constant viscosity. In aorta or other large vessels, blood is often regarded as a non-Newtonian fluid which enjoys a shear thinning effect [Gijsen et al., 1999]. In capillaries and arterioles, where the vessel diameter is only one order larger or even comparable to the size of RBCs, viscosity of blood flow becomes sensitive to details of the RBC dynamics and to their spatio-temporal organization. The circulation sites which correspond to microcirculation are made of arterioles, capillaries and venules. The microcirculation takes up around 80% of the total pressure drop in the systemic circulation (known as haemodynamics dissipation). Due to the dissipative nature and the increase of total cross-section area in capillaries with the branching levels towards smaller scales, the blood flow is heavily damped such that the pulsatile pressure originated from heart beat is negligibly small. The typical velocity in capillaries is of $0.03cm/s$ (see table 1.1). Because the size of the vessels is of the order of the RBCs it is a priori essential to take RBCs explicitly into account in order to analyze blood flow in microcirculation. This will be the strategy of this work.

Here we shall present some fundamental general comments and facts about microcirculation. Firstly, the Reynolds number, which is a dimensionless number that quantifies the ratio of inertial effect over the viscous effect in arteriole (where the shear stress is the highest) is estimated to be around 0.03 to 0.2 [Pries et al., 1992] (if one takes as a typical size the vessel diameter; that number would be even smaller if one takes the RBC diameter as a length scale), while in capillaries, it drops to around 3×10^{-4} [Pries et al., 1992]. These values all suggest that the blood flow in the microcirculation is dominated by viscous forces.

The second fact is the Fahraeus effect [Barbee and Cokelet, 1971, Pries et al., 1992] (see Fig. 1.3b), which states that blood circulating in successive bifurcations with smaller and smaller vessel diameters will have a hematocrit which decreases (i.e. hematocrit decreases when the vessel diameter decreases). This effect is important as long as the vessel diameter is less than $500\mu m$ and lasts until the channel width becomes comparable to the RBC size. This effect results from the tendency of RBCs to accumulate in the center, acquiring thus a higher mean velocity than that of the

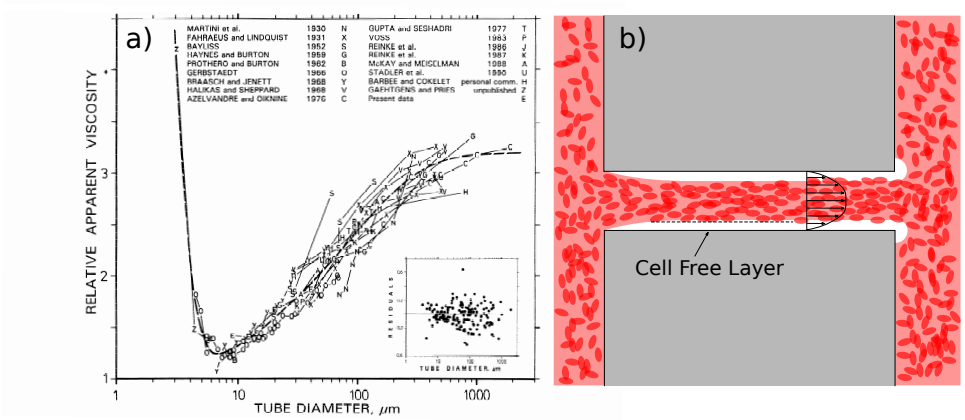

Figure 1.3: a) The Fahraeus-Lindqvist effect; b) a schematic showing the Fahraeus effect and the existence of a marginal cell-free layer.

plasma and leading to a diluted flow in smaller and smaller channels. The accumulation of RBCs at the center leaves a cell-free layer close to the vessel wall. A schematic is shown in Fig. 1.3b, highlighting the decrease of hematocrit level, which is attributed to the existence of the cell-free layer. Finally, note that in capillaries the hematocrit may significantly drop that the RBCs hydrodynamic interaction becomes small, meaning that studying a single cell dynamics may provide information on flow in capillaries. This question will be tackled in this work.

Another important phenomenon is known under the name of the Fahraeus-Lindqvist effect. It states that with decreasing vessel diameter, the apparent viscosity of blood decreases. This is a somehow counterintuitive result: the more blood is confined the better it flows. This effect is quite significant in vessel diameters ranging from approximately $10\mu m$ to $300\mu m$, see Fig. 1.3a. The existence of cell-free layer evoked above is one of the identified indirect cause for the Fahraeus-Lindqvist effect.

Finally, the complexity of capillary networks needs to be mentioned. Blood vessels branch from aorta to arterioles in a cascading manner, which means the diameter of a parent branch is typically larger than that of daughter branches (see Fig. 1.2a). However, this cascading terminates at the capillaries. In microcirculations, capillaries are the smallest vessels with diameters around few micrometers (5 to $10\mu m$, mentioned in wikipedia/Capillary). Capillary segments typically are several hundreds micrometer in length. They collectively interweave a network of complex topology and geometry (see Fig. 1.2b).

1.3 Advection Diffusion Events in Microcirculation

1.3.1 Examples of Gas & Nutrient Transport

As we mentioned above, comparing the chemical transport strategies such as the lack of circulatory system in flatworms (Fig. 1.1(left)) or open circulatory system in grasshoppers (Fig. 1.1(middle)), the human circulatory system (Fig. 1.1(right)) is far more sophisticated owing to the existence of RBCs and complex branching vessel networks. However, in capillary networks, diffusion is still the most important mechanism especially for molecules of small sizes. The diffusion mechanism relies on the different concentrations of solutes in blood and surrounding tissue. Normally, solutes diffuse from spaces with higher concentration to lower ones spontaneously (passive diffusion), but the contrary may happen (active diffusion, which requires energy). Passive diffusion can be exemplified by oxygen, amino acids and glucose which diffuse from blood to tissue, or carbon dioxide or metabolic waste, which diffuse in the reverse direction. Example of active diffusion are re-absorption of glucose, amino acids and salts by the proximal convoluted tubule of the nephron in the kidney. Additionally, the capillary wall is covered by a mono-layer formed by endothelial cells (see the schematic in Fig. 1.2e), which is the only barrier between capillary and tissues. The endothelial cells are differentiated into mainly three categories viz. continuous, fenestrated or sinusoid in order to adapt to the functions of surrounding tissue. In general, the barrier effect from continuous endothelial cells can often be simplified and described by Fick's law of diffusion, where the flux across the barrier is positively correlated to the concentration difference on either side of the membrane. For fenestrated or sinusoid endothelial cells in particular, the advection of bulk flow will also contribute to the transport due to their porous structures.

The dimensionless Peclet number characterizes the relative level of advection effect over diffusion effect at a particular spatial scale. A Peclet number far greater than one implies a slow diffusion comparing to flow advection. In the case of oxygen transport in capillaries, advection follows the downstream direction, whereas the diffusion is omnidirectional. Thus, a low Peclet number is preferred since in this case the oxygen can diffuse from hemoglobin to plasma and then to surrounding tissue, before it gets flushed away by the blood flow. The typical value of oxygen diffusivity in blood is around $2 \times 10^{-5} cm^2/s$, which yields a Peclet number around 1 in capillary flow (estimated using the capillary diameter and blood flow speed). Additionally, the RBCs often squeeze into narrow capillary, undergoing high deformation making a large proportion of their surfaces in the close vicinity of the endothelial cells. This

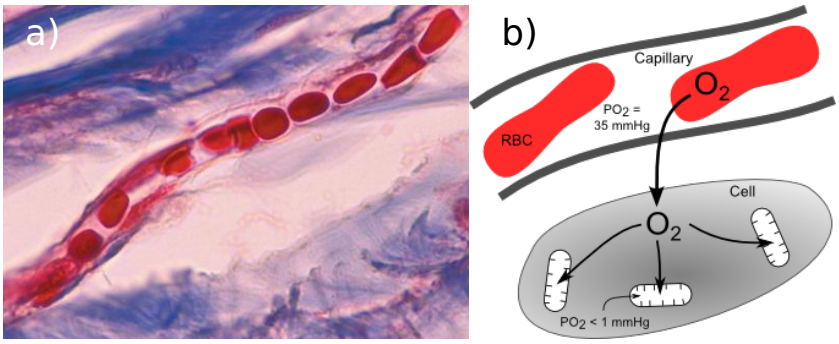

Figure 1.4: (a) Capillaries are so narrow that RBCs squeeze and move through them in a single file. (b) A schematic for oxygen diffusion. Oxygen dissociating from hemoglobin in RBCs diffuse into plasma and then into tissue. Low oxygen partial pressure (P_{O2}) is maintained in tissue due to the presence of mitocondria, which generates ATP and consumes oxygen. Courtesies of thoughtco.com and cvphysiology.com

fact should enhance the diffusion process over the advection one (see Fig. 1.4a). It is worth to mention that the lipid bilayer barrier against small molecules, such as oxygen, is expected to be quite small [Subczynski et al., 1992], meaning that oxygen dissociates from hemoglobin inside RBC and reach tissue cells by diffusion, and then rapidly consumed by mitochondria (see Fig. 1.4b). We will see below several examples where advection plays a decisive role.

1.3.2 Examples from Regulations based on Endocrine and Local Signaling

The circulatory system is regulated (say the control of perfusion rate) by many factors either originating from the circulatory system itself (like eNOS=endothelial Nitric Oxyde Sensing that may originate from vessel shear stress) or from nerve and endocrine systems (some glands may secrete hormones and feed the circulatory system in order to raise blood pressure).

Arteries, veins and arterioles have muscular walls (annular smooth muscles which encircles blood vessels) which are in close contact through gap junctions with endothelial cells and nerve ends from autonomic nervous system (see Fig. 1.2e where the endothelial cells are mentioned, nerve ends are omitted in the plot). This endows the vessel system with the capability of responding to hormones or nerve signals. The circulatory system interacts with the other systems (endocrine and nerve system) in a concerted fashion. The endocrine system is the chemical counterpart of nervous system: the nervous system transmits information using electrical potential, while endocrine system reacts via chemical compounds (hormones) towards blood

circulation. Like the nervous system has its neurons well branched in the body, the endocrine system uses the circulatory system as its highway. In certain circumstances, only special sites of the circulatory system are involved in the regulation process. For examples, there are some gland (called posterior pituitary gland) which act globally on the circulatory system. They secrete a hormone called vasopressin that can raise blood pressure everywhere by inducing vasoconstriction. In contrast, there are other hormones, secreted by the adrenal gland (adrenalin) which acts on specific sites of the circulatory systems, namely the smooth muscles of the arterioles, in two different pathways (suppressing blood perfusion rate in internal organs while increasing it in skeletal muscle) in order to improve athletic performance. The transport of all these hormones mainly relies on blood flow.

The above mentioned regulations by the endocrine system are achieved following a top to bottom approach (i.e. the hormone delivery is made everywhere in the circulatory system despite the fact that the hormone function may be selective). However, an inverse regulation mechanism may take place. Signaling can have a starting point at capillaries, and is then transmitted to higher branches, such as arterioles or even larger vessels. Indeed, and as mentioned at the beginning of this section, pre-capillary arterioles are wrapped by smooth muscles (which are absent in capillaries), so that tissue perfusion rate can be controlled by arterioles via constriction or relaxation in smooth muscles. When tissues are experiencing higher metabolism, the increase of catabolic products' concentration will be sensed by capillary endothelial cells. The signal will then be transmitted from endothelial cells to smooth muscle in parent arteriole via secretion of vasodilator chemicals.

In recent decades, a growing number of experimental evidences have shown the importance of mechanical properties in blood flow regulation. The blood vessel wall shear stress seems to play key roles in many regular or pathological processes including angiogenesis, atherosclerosis, tumor growth, wound healing and embryonic development, etc. [Risau, 1997, Yamamoto et al., 2003, Galie et al., 2014]. The first candidate of mechanical sensors is the endothelium [Yamamoto and Ando, 2011, Resnick et al., 2003], where endothelial cells form the innermost layer of blood vessel and have their lumen sides directly exposed to the blood flow. Both rapid and long term endothelial responses are observed (see Fig. 1.5).

Endothelial response in an attempt to regulate flow rate operate on a time scale of seconds or minutes. Endothelial cells release adenosine triphosphate (ATP) to blood vessel lumen in response to shear stress. Endothelial cells have the ability to conduct a complex process consisting in translating shear stress changes and surface

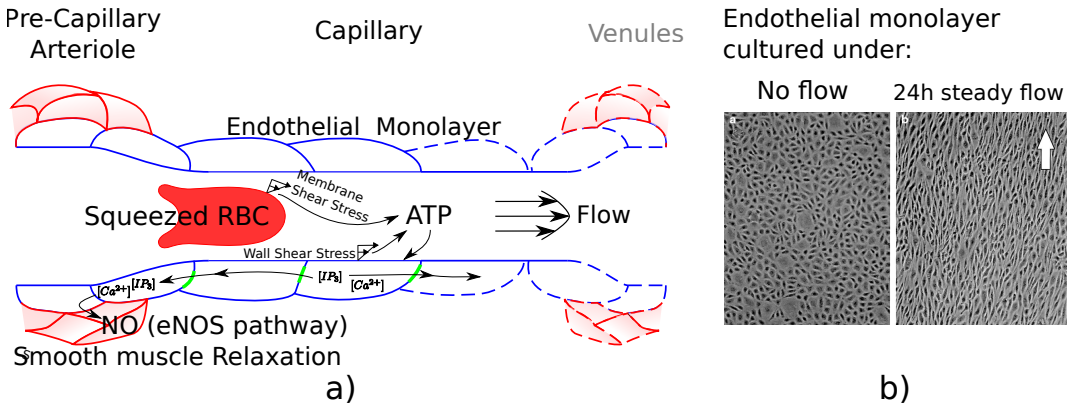

Figure 1.5: Endothelial cells acute and chronic responses to flow: (a) A hypothesized acute response (few seconds to minutes) triggerred by flow shear stress and RBC deformation. ATP release from RBC and endothelial cells trigger a calcium response that propagates bidirectionally, eventually initiate eNOS pathway in smooth muscle and conduct vasodilation in pre-capillary arteriole. $[Ca^{2+}]$ and $[IP_3]$ represents the free calcium ion concentration and inositol trisphosphate (abbreviated as IP_3, a secondary messenger molecule used in signal transduction) concentration. (b) Chronic response from bovine aorta endothelial cells, observed in *in vitro* experiment. The photo on the left side represents cells cultured under no flow condition, while photo on the right side is obtained after 24 hours exposure to steady flow, with an elongated cell pattern.

ATP concentration variations into oscillation in plasma calcium level (see Fig. 1.5a). These changes in calcium concentration is crucial for endothelial nitric oxide synthase (eNOS) pathway involved in vasomotor control [Topper et al., 1996]. Chronic responses (hours to days) may also occur implying changes in gene expression and de novo protein synthesis. With these metabolic alterations, endothelial cells tend to have an elongated shape aligned with blood flow (in laminar regimes), while they assume a more round shape under low flow rate or turbulent flow condition [Topper and Gimbrone Jr, 1999, Barakat, 2013]. These sites of low flow amplitude are believed to play important roles in dysfunctions such as initiation of atherosclerosis and the formation of thrombosis [Park et al., 2010, Barakat, 2013, Malek et al., 1999, Schwartz, 1962].

On the other hand, experimental studies on RBCs reveal that they can release ATP when subjected to shear stress originated from flow [Wan et al., 2008, Forsyth et al., 2011]. This implies that RBCs may actively participate in the signaling events and local regulations. How and by which mechanism the ATP release takes place will be discussed in chapter 4. A schematic showing how RBCs may interact with endothelial cells is presented in Fig. 1.5a.

1.4 Contributions of the thesis

To date, experimental and numerical studies have revealed the importance of RBC shape dynamics in microcirculation. Due to the hematocrit drop in microcirculation as a consequence of Fahraeus effect, numerical and theoretical studies on a single RBC yielded surprisingly persuasive results in explaining rheological observations. Although complex three dimensional RBC models are suitable for a quantitative analysis, simple models in two dimensional systems (such as vesicles in 2D Stokes flow) also capture several essential behaviors of RBCs, which implies, that those complex RBC shapes and dynamics may be only a disguized form of few prototypes. We will encounter several examples in this work.

This thesis is devoted to tackling the first main step towards linking RBCs dynamics to chemical solute dispersion in microcirculation, by focusing on both a single entity and collective effects. Since the introduced chemical dispersion itself is an ample increment of complexity to already-rich RBC dynamics, we restrict our work here to a 2D geometry, where the main features can still be captured. It must be kept in mind, as will be recognized throughout this work, that the extensions of the model and algorithms to 3D are straightforward. Here below we summarize the original contributions of each chapter.

1.4.1 The analysis of Vesicle dynamics in a channel flow

The first contribution is dedidacted to the numerical study of vesicle dynamics (a model of RBC) in channel flow involving the effect of viscosity contrast. As we mentioned in section 1.2.2, the blood flow in microcirculation has a small Reynolds number and can be regarded as Stokes flow. The present chapter is based on the boundary integral method (abbreviated as BIM, and is appropriate for Stokes flow), whereas in all other chapters a Lattice-Boltzmann method is adopted and/or developed. In chapter 2, we perform systematic studies on single and multiple vesicles in channel flow with intermediate channel widths that are comparable to arteriole and large capillaries. We found the emergence of a robust and stable slipper shape by taking physiological viscosity contrast value (say, around 5). Several other branches of solutions, such as complex trilobe dynamics and snaking parachute, are discovered. We provide a phase diagram of different solutions in terms of relevant control parameters (such as the flow strength, viscosity contrast and degree of confinement). We then analyse the rheological properties. An outstanding finding is the decrease of the normalized viscosity $[\eta] = (\eta_{eff} - \eta_{out})/(\eta_{out}\phi)$ (η_{eff} is the absolute effective viscosity,

η_{out} is the suspending fluid viscosity and ϕ is the hematorcit) with hematocrit. This results from a subtle spatial organization of the suspension, which strongly moderates the increase of the absolute viscosity with hematocrit. This confirms the fact that this feature is not exclusively restricted to a pure shear flow [Thiébaud et al., 2014] but is also present in a pipe flow. Interestingly, the viscosity decrease occurs in the hematocrit range of 0% – 15%, which lies in the typical range of microcirculation hematocrit. This effect seems to bring a remarkable contribution to the efficiency of oxygen transport in microcirculation. This work has given rise to a publication under preparation, to be submitted to Phys. Rev. Fluids.

1.4.2 Development of numerical solver for fluid-membrane-solute coupled system

Although BIM enjoys a high precision which is extremely helpful in studies of accurate shape dynamics and subtle regime borders in a shape phase diagram, it suffers from a quadratic dependence of simulation time with the number of discretization points that makes it difficult for practical purposes such as complex geometry and when a very large number of cells are considered. In addition, blood flow involves coupling with various chemical transport. In order to efficiently study this problem a lattice Boltzmann method (LBM) is adopted, which is a mesoscale method which enjoys a high parallel efficiency and easy implementation of complex geometry. LBM is employed in our work to explore regimes which are computationally expensive or hard to implement via BIM. We reconstructed the well validated immersed-boundary lattice-Boltzmann (IB-LBM) code from [Shen et al., 2017a] under Compute Unified Device Architecture (CUDA), in order to fully exploit the parallel benefits from LBM. In chapter 3, we developed our advection diffusion solver in the LBM framework.

Dispersion of chemical solutes with the presence of moving boundaries is rarely mentioned in literature. This task is challenging in both numerical scheme and engineering implementation. We managed to derive a boundary scheme that works for arbitrary moving membranes and boundary conditions. The implementation is also accelerated in parallel via CUDA. Several validations are performed for translating and distorting boundaries. Our solver has shown its capabilities of tackling typical scenarios of chemical signaling processes that are related with shear stress or an external stimulus. In addition, we have demonstrated the possibility of applying this solver to more generic topics, for example, the drug delivery problematic. Figs. 1.6a and b give simple demonstrations on the type of applications for complex geometry.

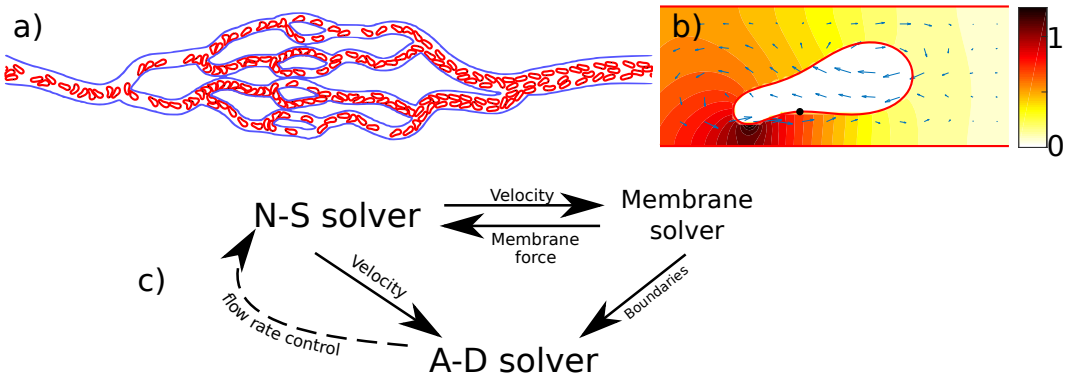

Figure 1.6: (a) An example of LBM method used to study a vessel network with realistic geometry (a network extracted from a mesentery of a cat); (b) An example of a deformed RBC under shear stress dependent ATP release in confined channel flow. The color bar represents the relative level of ATP concentration. Vectors correspond to relative induced flow; (c) A schematic for the coupling of Navier-Stokes (NS), membrane and advection-diffusion (AD). The dashed line represents a possible local regulation mechanism in microcirculation.

Fig. 1.6c is a simplified picture of the simulations. This work has given rise to a publication submitted to Physical Review E [Zhang and Misbah, 2018].

1.4.3 ATP release from RBCs under flow

Recent experimental studies *in vitro* [Forsyth et al., 2011, Wan et al., 2008], reveal that RBCs release ATP in response to flow stimulus. This feature connects the RBC dynamics to signaling processes of local regulation events in microcirculation. With the help of a solver dedicated to fluild-membrane-solute coupling, developed in chapter 3, we tackle in chapter 4 the problem of ATP release by RBCS; we have built a model inspired from hypothesized molecular mechanisms, and solved it with using the LBM. The model can reproduce results qualitatively comparable to *in vitro* shear flow experiments. Furthermore, we explored how this model behaves in channel flow and at bifurcations. The study is inspired by the geometry of arterioles and capillary networks. We found that the membrane shear stress is one of the key input to the release model. We found that the complexity of network geometry (i.e. bifurcations traversed by RBCs in microcirculation) may substantially contribute to ATP release in capillary network. This study has given rise to a publication accepted in Biophysical Journal [Zhang et al., 2018].

1.4.4 The calcium signaling in capillary Endothelial Cells

In chapter 5 we carried out preliminary studies on the signaling process associated with mechanical properties of blood flow in microcirculation. A simulation of endothelial calcium dynamics is conducted in consideration of RBCs releasing ATP, vessel wall shear stress and endothelial gap junctions. This demonstrates the possibility of studying mechano-involved regulation events in microcirculation, using our simulation tools and models.

Chapter 2

Vesicle Dynamics: The Effect of Viscosity Contrast in Channel Flow

This chapter deals with the problem of blood flow by adopting a simple model (i.e. suspension of 2D vesicles). We consider an imposed Poiseuille flow. It is shown that even a single vesicle shows plethora of solutions. For example, the vesicle exhibits a parachute centered shape, or a slipper shape (which are by now two classical modes already reported in 2D and 3D simulations). It is found here that other solutions exist, such as a fully off-centered shape, a solution which coexists with the parachute solution, and a multilobe shape which exhibits complex dynamics. Unlike recent reports in 3D which stress the necessity of shear elasticity for this kind of shape, the present 2D study rules out the relevance of elasticity ingredient. We will present a complex phase diagram in an appropriate control parameter space. We will then investigate the implication on rheology. We define the normalized viscosity as $[\eta] = (\eta_{eff} - \eta_{out})/(\eta_{out}\phi)$ (η_{eff} is the absolute effective viscosity, η_{out} is the suspending fluid viscosity and ϕ is the hematorcit). An outstanding feature reported here is that $[\eta]$ decreases with hematocrit in microcirculation. This results from a subtle spatial organization of the suspension, which strongly moderates the increase of the absolute viscosity with hematocrit. This behavior, if it is confirmed with 3D simulation, should imply that the specific spatial organization favors a more efficient oxygen supply in microcirculation.

2.1 Introduction

Blood flow imply motion of many interacting particles (Red Blood Cells –RBCs). Interactions are of different origins: (i) hydrodynamics, (ii) direct interaction (like

RBC-RBC bridging via macromolecules), or (iii) or purely entropic nature (depletion forces) (see [Brust et al., 2014, Flormann, 2017] for more details). The advent of microfluidics and the power increase of computers have caused a tremendous upsurge of interest in the study of blood flow. The computational power has rendered tackling the blood flow problem by following a bottom-up approach, i.e. by taking explicitly blood elements into account. RBCs are often modeled as a capsule, that is a membrane which is incompressible and which is endowed with in-plane shear elasticity (due to cytoskeleton) and bending. Another popular model in this spirit is the vesicle one, which is a closed membrane of a bilayer, devoid of a cytoskeleton. This is a simplified model of RBC. Simplification is essential since it allows us to decide whether or not such or a such phenomenon is a robust feature, or does it depend on some specific ingredient. Another simplification is often adopted, namely reducing the dimensionality, by considering the membrane as a contour rather than a surface. This 2D simplification allows often a very important gain at the computational level. Fortunately, many phenomena seen in 2D have also been seen in 3D as well (with 3D vesicles and capsules). Typical examples, are parachute and slipper shaped which are exhibited both in 2D and 3D (see Fig. 2.4b Centered Parachute and Near-Centered Slipper). The fact that shapes and dynamics are often shared by 2D and 3D systems is also another indication of their robustness. In this chapter we will adopt a 2D model in order to study dynamics and rheology of a single and multiple vesicles. In this study we will take only hydrodynamic interaction into account. Because of the 2D character only bending modes are present.

In a Poiseuille flow we can define three main parameters: the viscosity contrast, which is the ratio between the internal and external viscosity, denoted as λ, the strength of the flow compared with the bending mode, which will be called the capillary number and denoted as C_a , and the degree of confinement defined as the effective diameter of the vesicle over the channel width, and is denoted as C_n. A last parameter, which will be fixed here, is the deflation parameter (or reduced area), which quantifies the deflation of the shape from a circle (see precise definition of all these parameters in Section. 2.2). Vesicles as well as RBCs (represented by capsules in modeling) have shown complex dynamics even in simple confined Poiseuille flow [Noguchi and Gompper, 2005, Coupier et al., 2008, Kaoui et al., 2009, Kaoui et al., 2011, Farutin and Misbah, 2011, Coupier et al., 2012, Farutin and Misbah, 2013, Tahiri et al., 2013, Aouane et al., 2014a, Hariprasad and Secomb, 2015, Farutin and Misbah, 2014]. A typical diagram of steady shape in confined 2D channel flow (Fig. 2.1a) is

recalled (extracted from [Kaoui et al., 2011]). Typical shapes in 2D are (i) parachute, (ii) slipper, and (iii) snaking (in which the vesicles shapes oscillates as a snake).

The above studies have not yet exhausted all possible scenario. Our systematic analysis presented in this chapter shows the existence of other solutions, such as an off-centerd slipper, corresponding to a novel branch of solution as compared to the classical slipper, and multilobe complex dynamics. This type of multilobe shapes was reported recently in 3D (for capsules) [Mauer et al., 2018]. It was suggested there that the the multimode shape is due to cytoskeleton shear elasticity. However, since our study does not include shear elasticity, this means that the multilode shape is not necessarily triggered by elasticity. We will study here systematically different types of solutions by considering the three above control parameters λ, C_a , and C_n. A complex picture will emerge. After having analyzed the dynamics, we will study the rheology for various concentrations (or hematocrit). We will see that the existence of the new solutions will dictate novel and interesting rheological properties. An interesting feature is revealed. Let us define the normalized viscosity as $[\eta] = (\eta_{eff} - \eta_{out})/(\eta_{out}\phi)$ (η_{eff} is the absolute effective viscosity, η_{out} is the suspending fluid viscosity and ϕ is the hematocrit). It is found that $[\eta]$ decreases with hematocrit ϕ in the range $\phi \simeq 1 - 15\%$. This range of hematocrit is encountered in microcirculation. We shall see that this result is a consequence of a subtle spatial organization. This finding means that the absolute viscosity η_{eff} increases very slowly in this range of ϕ. Since the viscosity is a direct measure of flow efficiency, this results shows that the suspension organizes itself in a way to enhance RBCs transport, and thus oxygen carriage capacity.

2.2 Methodology: Simulation of Stokes Flow and The Modeling of Red Blood Cell as Vesicle

This study is carried out using a vesicle model under a 2D configuration, despite the complex 3D nature and spectrin network (the cytoskeleton, [Liu et al., 1987]) that may introduce quantitative (and possibly qualitative) deviation on the main results of this study. We will see that some shapes and dynamics that were suspected to be due to cytoskeleton are in fact reproduced here in 2D, ruling thus out the hypothesis of the cytoskeleton role. This is why we believe that a simplified model (e.g. pure 2D) should be analyzed in details before dealing with many other ingredients.

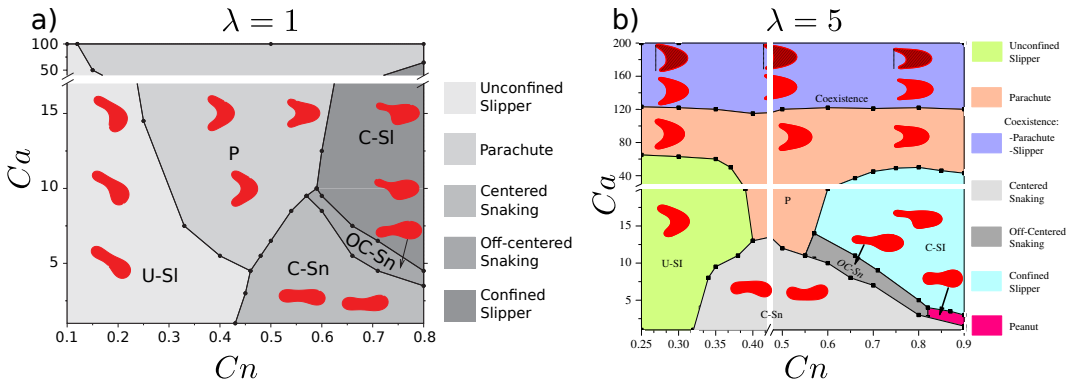

Figure 2.1: (a) A phase diagram of vesicle steady shapes in confined channel flow showing 5 distinct regions against degree of confinement C_n and capillary number Ca (for definition of parameters, see text). Other parameters are fixed as $\tau = 0.6$; $\lambda = 1$. Figure with courtesy of [Kaoui et al., 2011]; (b) The corresponding phase diagram from [Tahiri et al., 2013] with the same parameters except that here $\lambda = 5$. Figure with courtesy of [Tahiri et al., 2013]

2.2.1 The Vesicle model

Let us consider that a vesicle (as a representative of RBC) has its membrane shape depicted by a closed curve $\mathbf{X}(s,t)$ on x-y plan, where s is a curvilinear coordinate, t represents time. The Helfrich energy [Zhong-Can and Helfrich, 1989] is defined on $\mathbf{X}$, and takes into account bending modes under the constraint of local membrane inextensibility:

$$\mathbf{H}(\mathbf{X}(s)) = \frac{\kappa_b}{2} \oint c^2 ds + \oint \zeta ds \tag{2.1}$$

Here κ_b is the bending modulus of the membrane (for RBC its value is taken as $\kappa_b = 3 \times 10^{-19} J$), c is the local curvature

$$c = \frac{\partial X_x}{\partial s}\frac{\partial^2 X_y}{\partial s^2} - \frac{\partial X_y}{\partial s}\frac{\partial^2 X_x}{\partial s^2} \tag{2.2}$$

ζ is a Lagrange multiplier that enforces local membrane area [Ghigliotti et al., 2010]. Thanks to the functional derivative of $\mathbf{H}$, the force term acts from vesicle membrane on the fluid can be obtained as [Kaoui et al., 2008]

$$\mathbf{f}(s) = \kappa \left(\frac{d^2 c}{ds^2} + \frac{1}{2}c^3 - \zeta c \right) \hat{n} + \frac{d\zeta}{ds}\hat{t} \tag{2.3}$$

Here $\hat{n}$ and $\hat{t}$ are the normal and tangential unit vector respectively. The total area $A = \left| \oint \mathbf{X} \times d\mathbf{X} \right| /2$ is conserved due to the incompressibility of the flow.

We define the characteristic radius of a vesicle R_0 by the relation $A = \pi R_0^2$, which has for a RBC a typical value $R_0 = 3\mu m$. The reduced area τ is defined by the ratio

between vesicle area A and the area of a circle which has the same perimeter (denoted as P) as the vesicle

$$\tau = \frac{A}{\pi[P/(2\pi)]^2} = \frac{4\pi A}{P^2}. \tag{2.4}$$

This quantity specifies the roundness of the vesicle shape, the more round is the shape, the closer is its value to 1. We fix $\tau = 0.6$ in this study, in reference to the known value of a healthy RBC (which is about 0.65).

2.2.2 Simulation of Stokes Flow Using The Boundary Integral Method

We consider a single or multiple vesicles immersed in a periodic long straight channel, defined by a box $\Omega = [-L/2, L/2] \times [-W/2, W/2]$ (where W is the width and L the length). The dynamic viscosity of RBC cytoplasm is denoted as η_{in}, while the plasma one is denoted as η_{out}. The viscosity contrast is then defined as $\lambda = \eta_{in}/\eta_{out}$. A quadratic velocity profile is imposed as

$$u_x^0 = u_{max}^0 \left[1 - \left(\frac{y}{W/2}\right)^2\right] \tag{2.5}$$

and $u_y^0 = 0$, here u_{max}^0 is the maximum velocity at the center-line $y \equiv 0$.

Typical magnitude of blood plasma kinematic viscosity is $\eta_{out} \sim 10^{-3} mPa \cdot s$; the shear rate at the channel wall $\dot{\gamma}_w = (\partial u_x/\partial y)|_{y=-W/2} = 4u_{max}^0/W$ has its typical physiological value ranged from $100/s$ to $10^4/s$ [Vennemann et al., 2007], depending on the blood vessel size. Considering the fact that Reynolds number $Re = \dot{\gamma}_w R_0^2/\eta_{out} \sim O(10^{-4})$ is extremely small, the flow can be regarded as a Stokes flow. Using the boundary integral method (BIM) [Veerapaneni et al., 2009, Rahimian et al., 2010, Quaife and Biros, 2014, Trozzo et al., 2015, Pozrikidis, 1992] we can convert the Stokes equations into an integral equation for the evolving boundaries (vesicle(s) shape dynamics). For brevity, we recall essentially the key procedures of velocity computation: Firstly, we represent the membrane position $\mathbf{X}$ by a Fourier series defined on the complex plane.

$$X_x(s) + iX_y(s) = \sum_{k=-k_{max}}^{k_{max}} X_k \exp(2\pi iks) \tag{2.6}$$

where the complex amplitudes X_k are the shape parameters of the membrane. The membrane force term $\mathbf{f}(s)$ in Eqn. (2.3), regarded as a function of derivatives (e.g. local curvature c) and integrals (e.g. perimeter P) of $\mathbf{X}$, can then be analytically

represented as a function of x_k series. The velocity at any point $\mathbf{r}$ in the simulation domain can then be calculated by the boundary integral formulation with the viscosity contrast effect taken account:

$$\begin{aligned}\Lambda\mathbf{u}(\mathbf{r}) =&\mathbf{u}^0(\mathbf{r}) + \frac{1}{\eta_{out}}\oint \mathbf{f}(s')\cdot\mathbf{G}^{(2W)}(\mathbf{X}(s'),\mathbf{r})ds' \\ &+ (1-\lambda)\oint \mathbf{u}(\mathbf{X}(s'))\cdot\mathbf{T}^{(2W)}(\mathbf{X}(s'),\mathbf{r})\cdot\hat{n}(\mathbf{X}(s'))ds'\end{aligned} \tag{2.7}$$

The line integrals are carried out along all vesicles in the calculation domain. $\mathbf{G}^{(2W)}$ is the single layer Green's function, while the $\mathbf{T}^{(2W)}$ denotes the double-layer Green's function [Pozrikidis, 1992]. The notation $\mathbf{\Lambda}$ is defined as

$$\mathbf{\Lambda}(\mathbf{r}) = \begin{cases}\lambda, & \text{if } \mathbf{r} \text{ is inside a vesicle} \\ (1+\lambda)/2, & \text{if } \mathbf{r} \text{ is on a membrane} \\ 1, & \text{if } \mathbf{r} \text{ is out side of any vesicles}\end{cases} \tag{2.8}$$

This Green's function is rather complicated due to the restriction of satisfying periodic and no-slip condition at the same time. Instead, the numerical procedure employs another Green's function which satisfies only periodic condition denoted as $\mathbf{G}_P$ and $\mathbf{T}_P$. This Green's function can be represented in terms of the elementary functions [Pozrikidis, 1992]. The numerical procedure consists in representing the force and the residual velocity on the walls as a Fourier series. The residual wall velocity, here is the velocity on the walls calculated using Eqn. (2.7) with its Green's function being replaced by $\mathbf{G}_P$ and $\mathbf{T}_P$. The Fourier components of the residual wall velocities as well as the wall forces are calculated through explicit expressions and linear equations with explicit coefficients, respectively [Pozrikidis, 1992]. After this, the velocity contribution from wall forces to vesicles is added to the vesicle velocities using $\mathbf{G}_P$ and $\mathbf{T}_P$. This procedure is also done in Fourier space with explicit expressions [Pozrikidis, 1992].

Once having the velocity on the membrane, the evolution of vesicle shape is obtained from a simple fixed time step Euler scheme

$$\mathbf{X}(t+\Delta t) = \mathbf{X}(t) + \mathbf{u}(t)\Delta t \tag{2.9}$$

When implementing Eq.(2.9), velocity term $\mathbf{u}(\mathbf{X}(s'))$ on the right hand side in Eq. (2.7) takes its value at time t.

Two additional procedures were performed in order to ensure long-term stability of the simulations. First, we keep the inner volume of the particles fixed. Normally, fluid incompressibility and membrane impermeability should keep the inner volume

of the particles constant. However, a small drift due to numerical error can not be fully excluded. We compensate this drift by reinflating or deflating the elastic particle through homogeneous normal deformation. Second, we perform a small correction of membrane positions when two particles approach each other too closely (considered as a collision). The correction starts to act only when the distance between the particles' membranes is below a certain limit δh. The correction pushes the particles apart, thus preventing numerical instabilities from particle interpenetration.

In order to eliminate numerical artifacts, we performed several confirmatory simulations with more refined meshes in time steps, sampling points, Fourier harmonics and critical inter-particle distance δh. Based on this verification and a compromise between efficiency and accuracy, each particle was characterized by 63 Fourier harmonics. 2048 sampling points were used to resolve the short-range hydrodynamics interactions. The velocity of the particle membrane was calculated at 128 sampling points. The minimal distance δh for which the particles were unaffected by the collision-preventing procedure was 0.005 of the particle radius.

The choise of the number of harmonics for walls depends on channel length L, By using harmonics from 256 to 1024, the residual wall velocity was found to be of very small fraction of velocity in the center of the channel (with relative value less than 10^{-5}, reducing to machine precision in many cases).

We define the dimensionless capillary number

$$Ca = \eta_{out}\dot{\gamma}_w R_0^3/k_b = \dot{\gamma}_w \tau_c \tag{2.10}$$

which describes the fluid strength over vesicle bending strength, or it can be interpreted as a ratio of a characteristic time scale for vesicle deformation (τ_c) and the time scale of the imposed flow $1/\dot{\gamma}_w$.

The problem has three dimensionless numbers: i) the viscosity contrast λ, ii) the capillary number Ca, iii) the degree of confinement $C_n = 2R_0/W$; note that we have fixed the reduced area to $\tau = 0.6$ to represent RBC. The simulation box always has its length $L = 10W$, which is validated as being long enough to eliminate artifacts due to periodic boundary conditions [Thiébaud and Misbah, 2013]. We checked also that all simulations results have numerical perimeter deviations less than 0.3%, which is taken here to be as an acceptable value.

2.3 Results and Discussion

One main novelty of this study is to show the existence of several solutions, more or less complex, for the same set of parameters. The traditional solution in a Poiseuille

flow is the parachute solution. Other solutions have been classified as a slipper solution [Kaoui et al., 2009] where the center of mass of the cell is not at the center-line, and thus the overall shape in not symmetric with respect to the flow center-line. In order to identify solutions which are different from the parachute one, it is natural to define the lateral position of the vesicle as a simple measure for that deviation. This deviation, denoted as $h(t)$, is defined as

$$h(t) = \frac{[\oint_{mem} \mathbf{X}(t) \cdot \hat{y} ds]}{WP} \tag{2.11}$$

where $\hat{y}$ is the unit vector of y (lateral) direction. h has its values ranging from -0.5 to 0.5, with 0 denoting center-line. The final lateral position can then formally be defined as

$$h_f = \lim_{T \to \infty} \frac{\int_0^T h(t) dt}{T} \tag{2.12}$$

In practice, the simulation time should be large enough in comparison to the intrinsic relaxation time τ_c. We start the simulation with a well relaxed vesicle with a biconcave shape aligned along the flow direction. This choice is of course arbitrary, and any other choice could be selected as well. We shall discuss later the impact of initial conditions. $h_0 = h(0)$ denotes the initial lateral position. The simulation ran for long enough time until a steady or periodic (or permanently chaotic in rare cases) pattern is observed. Thus, h_f can be approached by $h_t = \int_{T_0}^{T_1} h(t) dt$. Here T_0 and T_1 are chosen to guarantee that the transient effects have decayed before T_0 and that the time interval $T_0 - T_1$ is long enough to ensure the convergence of h_f.

2.3.1 The Emergence of The Off-centered Final Position by Increasing Viscosity Contrast

The viscosity contrast appears to be a factor having a strong influence on the solution behavior. We exemplify the main finding of this investigation by fixing the two other remaining parameters $(C_n, Ca) = (2/7, 80)$. **Recall Figs. 2.1a and b, this set predicts a parachute final shape and $h_f = 0$ for both cases with $\lambda = 1$ and** $\lambda = 5$. By acting on the initial position h_0 from 0 to 0.4 with interval 0.05, we observed an off-centered final position for $\lambda = 5$ with a slipper-like shape (Fig. 2.2b).

This off-centered final shape emerging at higher λ is found to be a robust feature. The behavior of h_f against λ is shown in Fig. 2.3a. When λ is larger than a critical value $\lambda_c^{(OC)} \approx 4$, an off-centered stable branch emerged ($h_f^{(OC)}$). If a vesicle has its initial position and viscosity contrast pair (h_0, λ) residing in the red region in Fig. 2.3a, then the final position is off-centred $h_f^{(OC)}$ and the vesicle shape may be referred

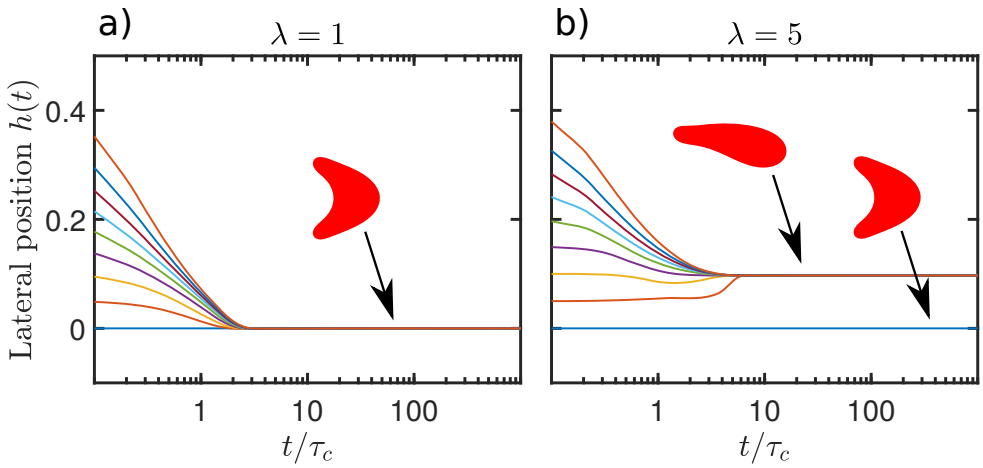

Figure 2.2: (a) Normalized lateral position versus time. Different curves $h(t)$ correspond to different initial positions, with $\lambda = 1$. All curves converge to $h_f = 0$, which corresponds to a parachute final shape; (b) $h(t)$ curves obtained with $\lambda = 5$, where vesicles start from an off-centered initial position ($h_0 \geq 0.05$), and they reach an off-centered final position $h_f = 0.097$. If instead we start from $h_0 = 0$ we obtain $h_f = 0$ (parachute shape), which has been reported in [Tahiri et al., 2013] (Fig. 2.1). The stability of $h_f = 0$ is validated by imposing small perturbations about the presumed steady state solution.

to as a slipper shape. One may notice that when $\lambda > \lambda_c^{(OC)}$, the attraction domain of $h_c^{(OC)}$ is much wider than that of $h_c^{(C)}$. This result would imply that a slipper shape may be a more common scenario than parachute (Fig. 2.3c) in vivo, given the fact that λ lies in the range around $5 \sim 10$ for healthy RBCs.

The coexistence of two stable branches in Fig. 2.3a (red and blue lines with filled circles) is a prototypical behavior of a saddle-node bifurcation. The saddle-node point is estimated from our simulations to be close to $(h_f, \lambda) = (0.072, 4)$. We have indeed seen that simulations with initial position $h_0 = 0.05$ or 0.1 (which are close to $h_f = 0.072$) both end up with their final position at the center-line. Recall that all the simulations obtained in Fig.2.3a the initial shape is a flow-aligned biconcave shape. However, when using an off-centered slipper as an initial shape (in Fig. 2.3b), while keeping the same initial positions, the final position is off-centred $h_f^{(OC)}$. We have checked and excluded the possible numerical artifacts such as deviation in perimeter or reduced area. Thus, we believe this sensitivity to initial shape is an indication of the saddle-node point.

Besides the off-centered slipper as a final shape, we also observed a parachute-snaking shape pattern at $\lambda = 10$ and $h_0 \leq 0.1$ (see Fig. 2.3d). We will see below that this snaking motion appears as an intermediate state between parachute and another

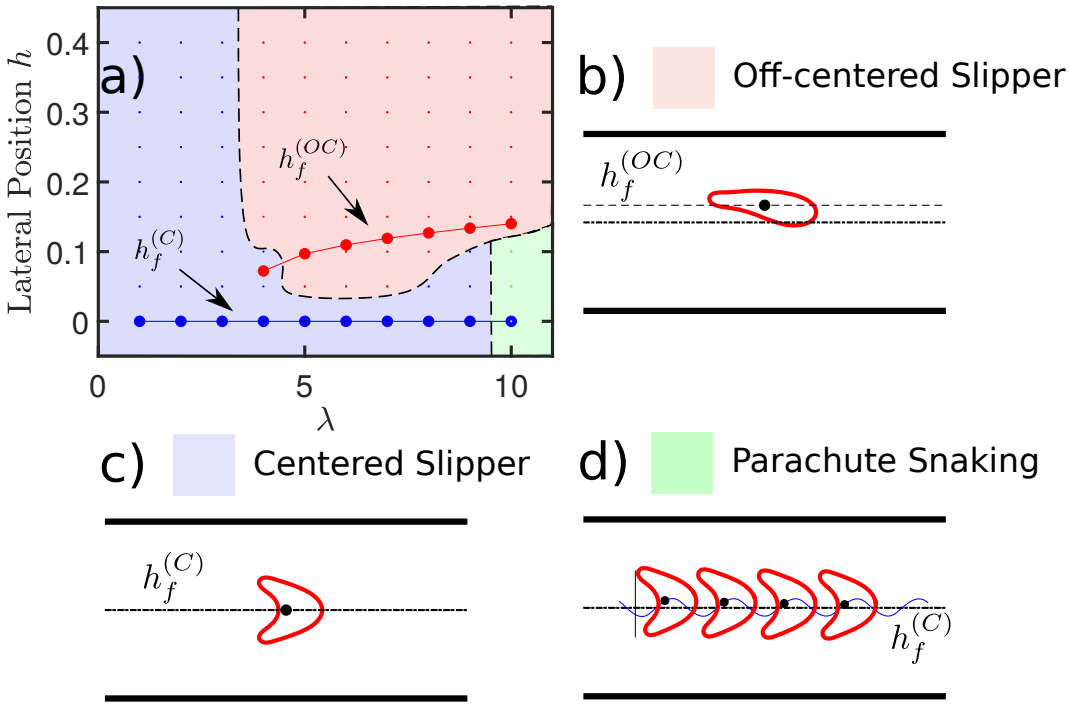

Figure 2.3: The emergence of $h_f^{(OC)}$ and the corresponding final shapes, with confinement $C_n = 2/7$: (a) The blue and red lines represent centered ($h_f^{(C)}$) and off-centered ($h_f^{(OC)}$) final position as a function of the bifurcation parameter λ. Simulations are performed with different initial positions (h_0) but with a flow-aligned biconcave shape, represented by (red or blue) dots. All initial conditions within a given domain (blue or red) yield a given final position, which is either $h_f^{(C)}$ (when initial data are in the blue region) or $h_f^{(OC)}$ (when initial data are in the red region) depending on λ and h_0. The corresponding basins of attraction are colored in red or blue. The dashed line represents borders and are here plotted just as a guide for the eye. A parachute snaking dynamics is observed when $\lambda = 10$ and $h_0 \leq 0.1$. (b), (c) and (d) are schematics for final shapes and $h_f^{(C)}$) (the blue trajectory in (c))

steady shape.

2.3.2 The General Dynamical Diagram

Here we will summarize the main results. We have found that besides the viscosity contrast, the confinement plays also a crucial role. We shows the diagram of solutions against λ for different confinements, from $W = 5R_0$ to $10R_0$ (corresponding to $C_n = 0.2 \sim 0.4$) in Fig. 2.4. In this range of confinement, the phase diagram at $\lambda = 1$ (Fig. 2.1a) indicates either unconfined slipper or parachute shape. Let us analyze the effect from λ for different $C_n \gtrsim 0.45$ (Fig. 2.1). Comparing to results in Fig. 2.3a, two new final positions associated to two final shapes emerged. The cyan color indicates a

zone, where simulations started with parameter (h_0, λ) ends up with a near-centered final position (this final position is denoted as $h_f^{(NC)}$). Starting inside yellow zone leads to a complex tumbling motion with an apparently chaotic behavior. Running simulations for more than $500\tau_c$, we have found that the final position h_f, as defined in Eq. (2.12), oscillates between $h_f^{(NC)}$ and $h_f^{(OC)}$ in an apparently erratic fashion.

We observed that the off-centered slipper region (red zones in Fig. 2.4a) appears when $W \gtrsim 5R_0$. Increasing W, the critical value $\lambda_c^{(OC)}$ for the appearance of the off-centred position decreases. In the meantime, the whole red zone is also sweeping leftward. This leftward shifting is also valid for the cyan colored region corresponding to near-centered slipper region. The parachute snaking (represented by green vesicle in Fig.2.4b) is viewed as an intermediate state between parachute and near-centered slipper. The smallest region -where a complex tumbling motion prevails- (denoted in yellow in Figs.2.4a and b), which can be viewed as the intermediate state between the near-centered slipper and off-centered slipper, shifts towards the left side as well. This general global while varying λ for different W (or C_n) may be indicative that one could find another representation of the results where both λ and W can be varied following a certain functional dependence $p(\lambda, C_n)$. In other words, instead of varying both parameters independently, a single combination would be more relevant. The diagram illustrating this is shown below.

The results of Fig. 2.5 are to be viewed as the projection of the results from the parameter plane (λ, C_n) onto the single line $p(\lambda, C_n)$. This function is considered to be monotonic with respect to both λ and C_n, obeying $\partial p/\partial\lambda > 0$ and $\partial p/\partial C_n < 0$. The degree of confinement C_n does not qualitatively change the behavior of vesicle dynamics within the considered parameter range ($1 \leq \lambda \leq 10$, $1/10 \leq C_n \leq 1/2$). The simulation results in Fig. 2.4 and their robustness highlighted in Fig. 2.5 shows that branch $h_f^{(OC)}$ is a saddle-node bifurcation, where $h_f^{(OC)}$ (red line in Fig. 2.5) and the dashed line border of the red zone are its stable and unstable branches, respectively. The branch $h_f^{(NC)}$ results from a Pitchfork bifurcation out-of the parachute solution. $h_f^{(NC)}$ (cyan line in Fig. 2.5) and its negative image $-h_f^{(NC)}$ are the two stable branches; $h \equiv 0$ is the unstable branch.

2.3.3 The Effects of the Capillary Number

The capillary number Ca is a measure of degree of membrane deformability. The increase of flow velocity or the decrease of membrane bending modulus are typical ways of increasing Ca. We investigated the same parameter set (h_0, λ) as mentioned in section 2.3.2 but with different values of Ca. We found no topological changes

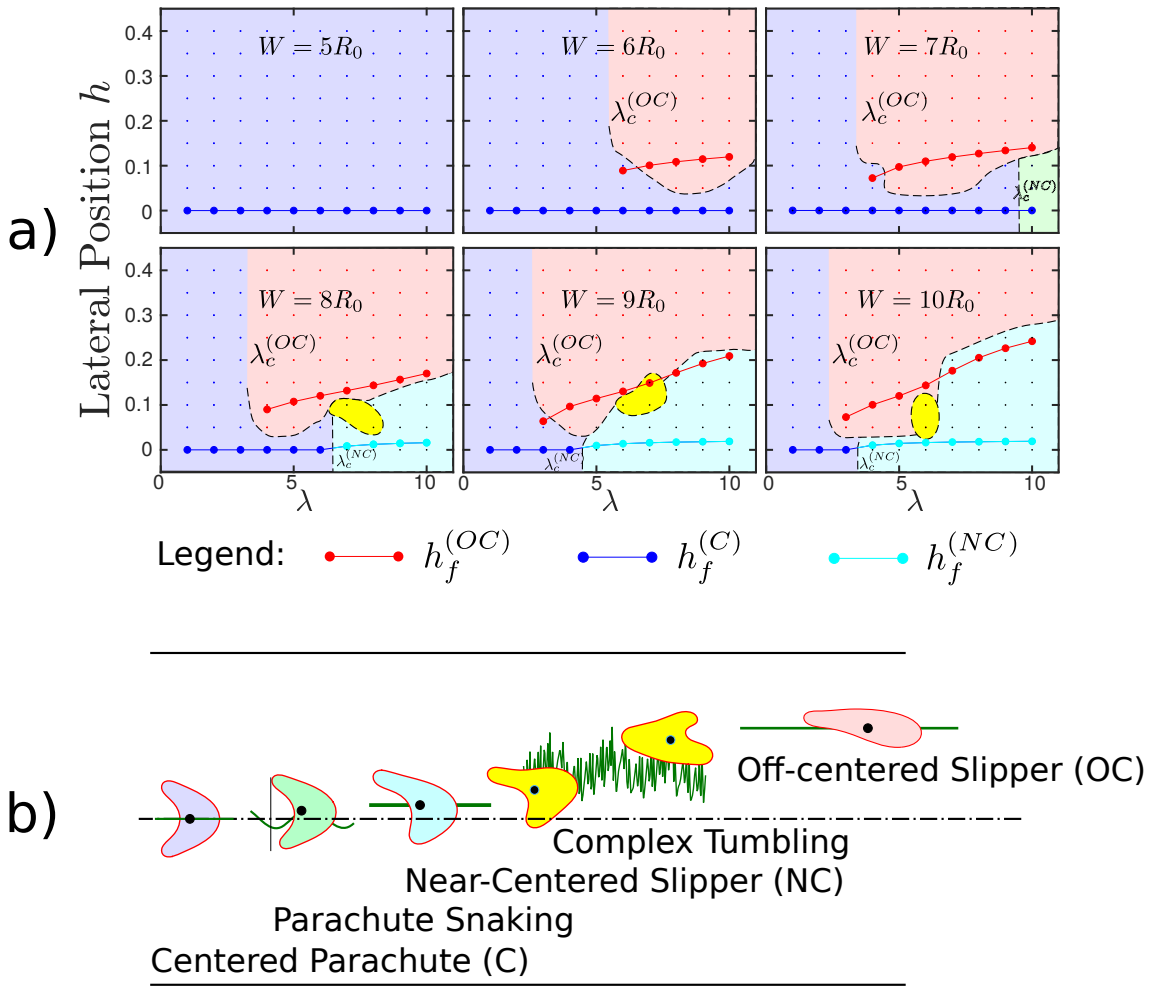

Figure 2.4: (a)Evolution of final positions and final shape diagram against channel width (Confinement). The red, blue and green zones are as defined in Fig. 2.3a. Two distinct final patterns emerged when $W \gtrsim 8$. The yellow region represents long term tumbling (longer than $500\tau_c$ in simulation time) with apparently chaotic dynamics. The cyan region represents a final slipper shape that is slightly different from parachute (its final position is slightly away from center line). The dashed lines are guide lines separating domains with different solutions. The notation $\lambda_c^{(OC)}$ indicates the position of the border between red and blue regions. $\lambda_c^{(NC)}$ is the critical value where transition from parachute to near-centered slipper happens. (b) Final shapes observed in diagrams above, the colors indicate corresponding regions in those diagrams. The dark green lines represent their final $h(t)$ schematically. One may notice the ascending order from centered parachute to off-centered slipper. This order is always preserved when having λ fixed. The parachute snaking and complex tumbling are considered as intermediate states of the other three steady states.

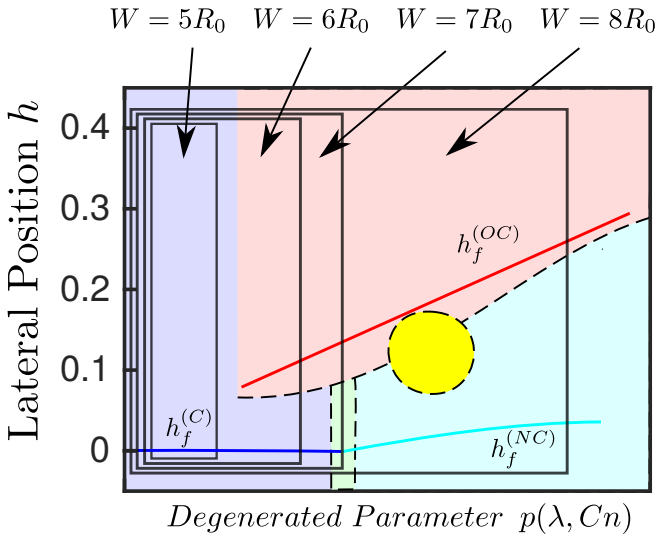

Figure 2.5: A schematic plot showing an attempt to combine both C_n and λ into a single parameter p. The black frames plotted with black solid lines (indicated by arrows) are mappings of the diagram from h vs p back to h vs λ plot. One may notice that each frame contains a similar diagram corresponding to simulation results (in Fig. 2.4a). Final positions of the three steady shapes are plotted in blue ($h_f^{(C)}$ for parachute), cyan ($h_f^{(NC)}$, near-centered slipper), and red ($h_f^{(OC)}$, off-centered slipper).

for off-centered slipper region (which has final position $h_f^{(OC)}$), when comparing to the diagram in Fig. 2.5. However, when Ca is decreased from 80 to 8 and then to 4, we observed a significant shrinkage and even collapse (when $W \gtrsim 7R_0$) of the parachute region, see Fig. 2.6. This observation was also reported in [Kaoui et al., 2009]. The fact that this occurs for a capillary number of order unity is indicative of the competition of the hydrodynamic stress and the bending resistance. Note that for $Ca \lesssim 8$, the time needed to reach final shapes becomes long. For example, when $Ca = 4$, $\lambda = 4$ and $h_0 = 0.4$, it took about $10^3\tau_c$ to reach the final position and final shape. The dashed line with cyan color in Fig. 2.6 represents the terminal position (near-centered slipper) for $Ca = 4$.

It is interesting to compare dynamics of two situations obtained for two extreme capillary numbers. Consider the points A1 and A2 having as coordinates $(Ca, \lambda, h_0) = (4, 6, 0.1)$ and $(4, 6, 0.05)$ respectively. The second set of points are B1 and B2 having as coordinates $(80, 6, 0.1)$ and $(80, 6, 0.05)$ respectively (see Fig. 2.6). When $Ca = 80$ the dynamics of both B1 and B2 exhibit complex tumbling motion, whereas when $Ca = 4$ (points A1 and A2) show a stable near-centered slipper shape. The lateral position curves ($h(t)$) and their corresponding shapes are plotted for the first $1000\tau_c$ in Fig. 2.7. When $Ca = 4$, both simulations with $h_0 = 0.05$ and 0.1 lead to tumbling

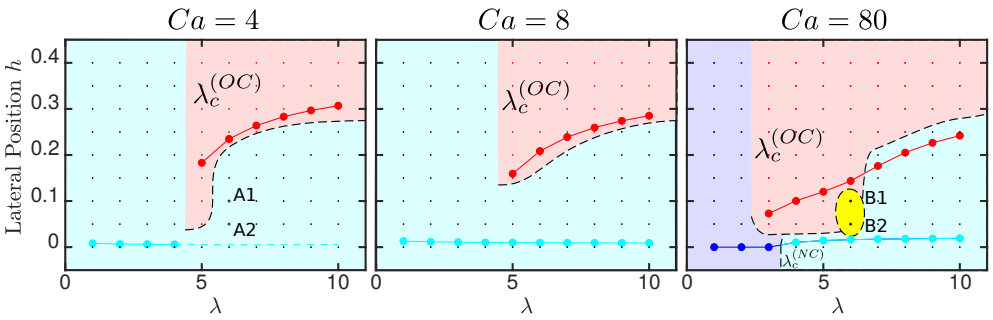

Figure 2.6: The evolution of final position h_f with viscosity contrast for $Ca = 4$, 8 and 80. The colors and final positions share the same definition as in Figs. 2.4 and 2.5. In all these simulations, C_n is fixed at 0.2. It is confirmed that the off-centered slipper is robust and exists for all explored capillary numbers. The parachute shape is not preferred when Ca is small. When $\lambda = 1$, our simulation results are consistent with the results from [Aouane et al., 2014b] (see Fig. 2.1a).

with small deformation, while their lateral position are gradually descends to reach the final state. Supplementary simulations with initial position from $h_0 = 0.04$ to 0.01 suggest that $h(t)$ will keep descending until it reaches $h_f^{(NC)}$ – the final position for near-centered slipper, although the whole tumbling process lasts for long time, $t \sim O(10^4 \tau_c)$. For $Ca = 80$, the complex tumbling motion (for cases B1 and B2) prevails. It is worth of mention that the shape exhibited in Fig. 2.7 for $Ca = 80$, which may be called "trilobe shape" [Lanotte et al., 2016, Mauer et al., 2018] take place here for a purely fluid system (i.e. in the absence of cytoskeleton elasticity); This points to the fact that this shape is robust since it does not depend on the details of the underlying structure. The domain of existence of this type of motion is shown by yellow zones in Fig. 2.4.

2.3.4 Impacts on Rheology

Our goal in this section is to analyze the rheological properties of the suspension, from very dilute to relatively dense suspensions. One objective in the dilute regime is to make a link between the branches of solutions discussed above and the rheology.

Let us recall the basic results of the last sections. For values of confinement C_n between 0.2 to 0.4 and viscosity contrasts $1 \lesssim \lambda \lesssim 10$, we have seen from sections 2.3.1, 2.3.2 and 2.3.3, that the main effect of high viscosity contrast is the introduction of an off-centered slipper shape (with corresponding final lateral position denoted as $h_f^{(OC)}$). Moreover, we have seen that by exploring a wide large range of the capillary number Ca (from 4 to 80), that for viscosity contrast in the range $4 \lesssim \lambda \lesssim 7$, the

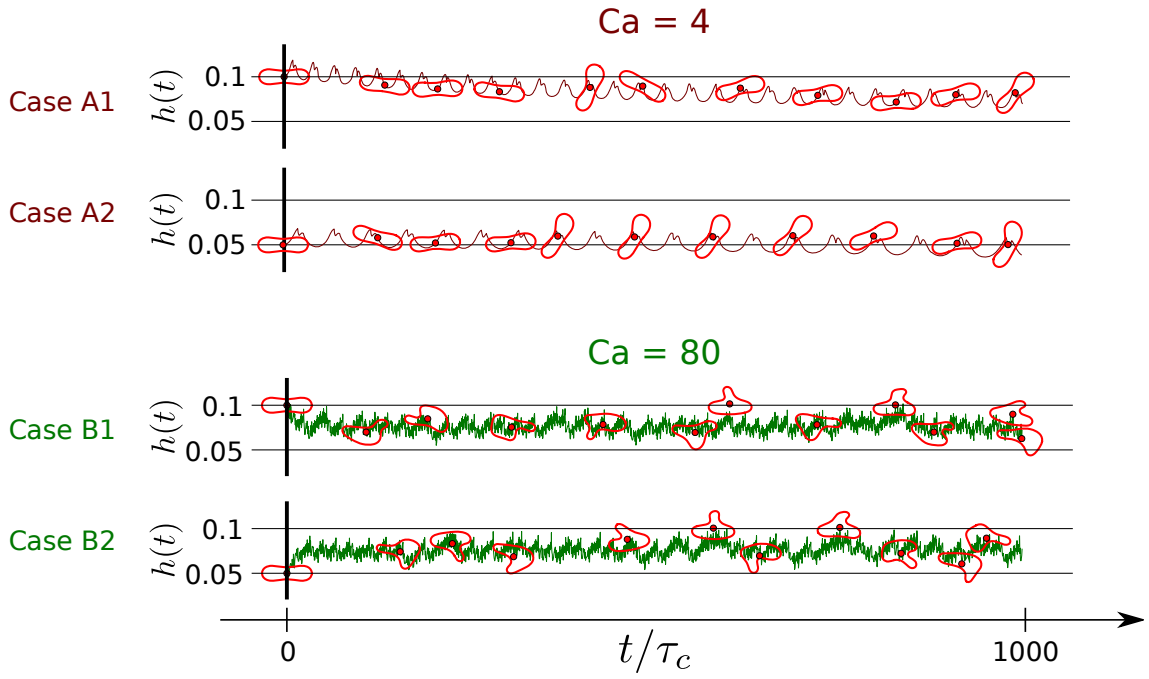

Figure 2.7: Emergence of a complex attractor upon an increase of Ca: In all 4 cases, λ is fixed at 6. When $Ca = 4$, both A1 and A2 yield $h(t)$ curves with a downward drift, which could imply a priori that this tumbling motion could be unstable. However, long time simulation confirms convergence of this solution. For $Ca = 80$, $h(t)$ corresponding to B1 and B2 always oscillate in a complex fashion between 0.05 and 0.1, illustrating the existence of a complex attractor, with a chaotic-like signature.

off-centered slipper region has the largest attraction zone. Interestingly, this range lies in the viscosity contrast value range for healthy RBCs.

We discuss below the viscosity of vesicle suspension. The (areal) concentration of a vesicle suspension is defined as $\phi = n \cdot \pi R_0^2/(LW)$, here n is the number of vesicles in the suspension. The effective viscosity of vesicle suspension is defined by

$$\eta_{eff} \cdot Q^{(ssp)} = \eta_{out} \cdot Q \tag{2.13}$$

where η_{eff} denotes the effective viscosity, Q^{ssp} is the average flux of vesicle suspension, Q is the flux of the pure fluid (with viscosity η_{out}) which is subjected to the same pressure gradient as Q^{ssp} is. We recall that η_{out} is the viscosity of external fluid. The intrinsic (or normalized) viscosity, $[\eta]$ –which evaluate the contribution of a solute (vesicles in this study) to the viscosity of a solution– can be defined as

$$[\eta] = \lim_{\phi \to 0} \frac{\eta_{eff} - \eta_{out}}{\eta_{out}\phi} \tag{2.14}$$

The total velocity is composed of the imposed flow $\mathbf{u}^0$ (the first term of the right-hand-side of Eq. (2.7) and the induced flow $\mathbf{u}^{(ind)}$(the terms represented by integrals in Eq. (2.7)). One can express the normalized viscosity as a function of the induced flow and the areal concentration. We straightforwardly find

$$[\eta] \approx \frac{\eta_{eff} - \eta_{out}}{\eta_{out}\phi} = -\frac{[u_x^{(ind)}]}{1 + [u_x^{(ind)}]\phi} \approx -[u_x^{(ind)}], \tag{2.15}$$

where the last equality is valid in the dilute regime. $[u_x^{(ind)}]$ is the flow-aligned component of a normalized mean induced velocity defined as

$$[u_x^{(ind)}] = \frac{< \int u_x^{(ind)} dxdy >}{\bar{u}_x^0 \cdot n\pi R_0^2} \tag{2.16}$$

Here $\bar{u}_x^0$ is the mean velocity of the imposed flow, $< \cdot >$ is the time averaging operation (for steady shape, it can be omitted), $n\pi R_0^2$ is the total area of all vesicles immersed in the flow. Through boundary integral formula (Eq. (2.7)) it can be seen that $[u_x^{(ind)}]$ contains directly information on the vesicle shape, which depends on the dimensionless parameters such as λ, C_n, Ca etc.. Analytical computation of $[u_x^{(ind)}]$ based on Eq. (2.7) is not an easy task. Here, we evaluate it numerically with a equidistant spatial mesh size $\Delta x = 0.1R_0$. Based on the concept of normalized mean induced velocity $[u_x^{(ind)}]$ defined in Eq. (2.16), the local normalized induced velocity can be written as

$$U_x^{(ind)}(\mathbf{r}) = \frac{u_x^{(ind)}(\mathbf{r})}{\bar{u}_x^0 \cdot \phi} \tag{2.17}$$

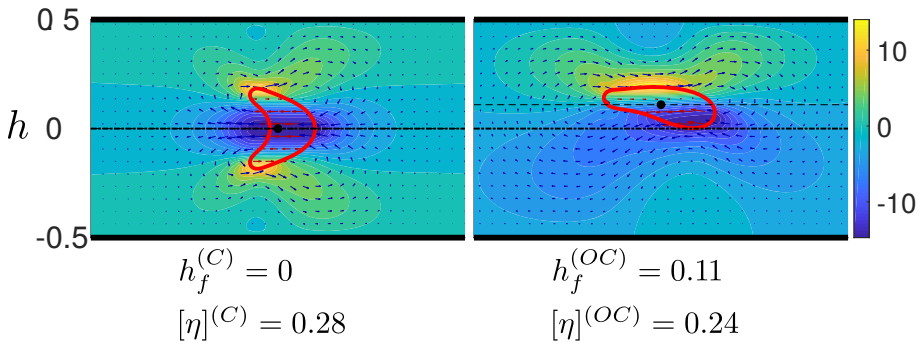

Figure 2.8: Vesicles possessing different final shapes with the same parameter set $((Ca, \lambda, C_n) = (80, 6, 2/7))$. The color map shows the flow-aligned component of the normalized local induced velocity field $U_x^{(ind)}$ (see Eq. (2.17), which has its mean value approximately equal to $-[\eta]$. The off-centered slipper has its normalized viscosity $[\eta]^{(OC)} \approx 0.24$, and is about 15% smaller than its counterpart for the centered parachute ($[\eta]^{(C)} \approx 0.28$)

Its mean value $[u_x^{(ind)}]$ (Eq. (2.15)), is approximately equal to $-[\eta]$ when the suspension is dilute.

We plot the $U_x^{(ind)}$ fields for two distinct steady states: a centered parachute (as show in Fig. 2.3c) and a slipper at an off-centered position (as shown in Fig. 2.3b) respectively, fixing parameters at $Ca = 80$, $\lambda = 6$ and $W = 7R_0$. A quick glance to that plot shows that the figure which exhibits more darker blue color (Fig. 2.8a) would provide the higher viscosity, since this is related to the negative average value of the induced field.

Figure 2.9 shows h_f and $[\eta]$ as functions of λ including both center and off-centered branches at $Ca = 80$. For $Ca = 8$ and 4, apart from an increase in the absolute magnitude of$[\eta]$, we observed no qualitative change in their corresponding diagrams. We can summarize the observed trends into three classes:

i) for center parachute, the normalized viscosity is not sensitive to λ, but its absolute value is approximately proportional to its corresponding C_n. ii) for off-centered slipper (red curves in Fig. 2.9), its final position $[\eta]^{(OC)}$ positively correlates with $[\eta]$; iii) for near-centered slipper (blue curves in Fig. 2.9 where it has non-zeros h_f value), the increase of λ results in a slight decrease in $[\eta]$.

The trend i) is obvious since both the shape and lateral position are almost preserved among different λs. This indicates only the presence of walls (and their width) dictate the viscosity $[\eta]^{(C)}$ For trend ii), we consider the off-centered final position as a result of the balance between the lifting force from the wall (see [Seifert, 1999, Coupier et al., 2008, Olla, 1997, Cantat and Misbah, 1999, Vlahovska and Gracia, 2007, Vla-

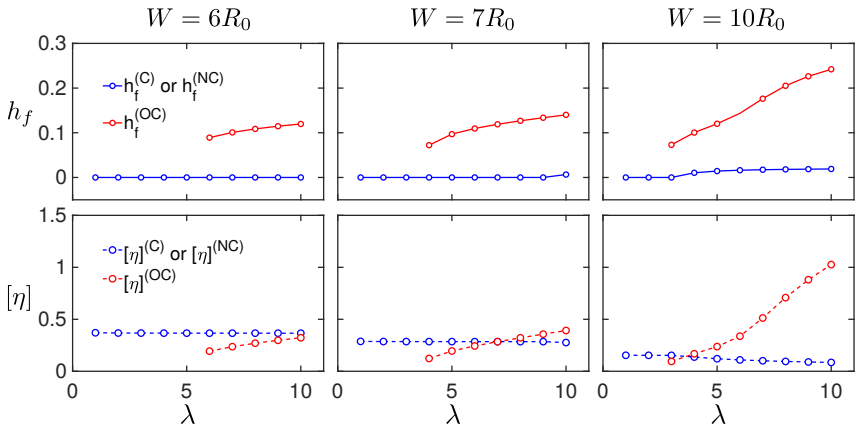

Figure 2.9: Final position and normalized viscosity as a function of viscosity contrast. The capillary number is fixed at $Ca = 80$.

hovska et al., 2009, Farutin and Misbah, 2013]) and the lateral migration towards off-center direction when viscosity contrast is high (see [Farutin and Misbah, 2013]). In the same time, the increase of $h_f^{(OC)}$ is accompanied by an increase of effective viscosity (well-known as the Fahraeus-Landqvist effect [Fahraeus and Lindqvist, 1931]). This effect is the main reason of the interdependency between $h_f^{(OC)}$ and $[\eta]^{(OC)}$. For trend iii), where the vesicle is almost at the center line, the Fahraeus-Landqvist effect becomes negligible. Instead, the near-centered slipper (see its schematic shape in Fig. 2.4b), when compared to the parachute shape, has a smaller lateral extent in the vertical direction and and in addition exhibits a tank–treading motion (meaning it acts as a smoother obstacle to the flow in comparison to the parachute shape). Both these two features trigger a slight decrease of the effective viscosity; this tendency is is enhanced with λ. However, when W increase the slipper become more and more off-centered and therefore its lag with respect to the imposed flow increases, resulting into further dissipation. We observe then a cross-over where the off-centered solution has higher viscosity than the parachute one.

2.3.5 Investigation of Rheology for Higher Concentrations

Here we would like to analyze the rheological properties for higher concentrations. It was reported that under linear shear flow [Thiébaud et al., 2014] the suspension organizes in files that lead to non monotonous behavior of the normalized viscosity $[\eta]$. This behavior was a direct consequence of the confinement and of the fact that the vesicles are subject to wall migration effect. *In vivo* the flow is of Poiseuille type, and it is therefore important to see how the rheological properties are affected by confinement.

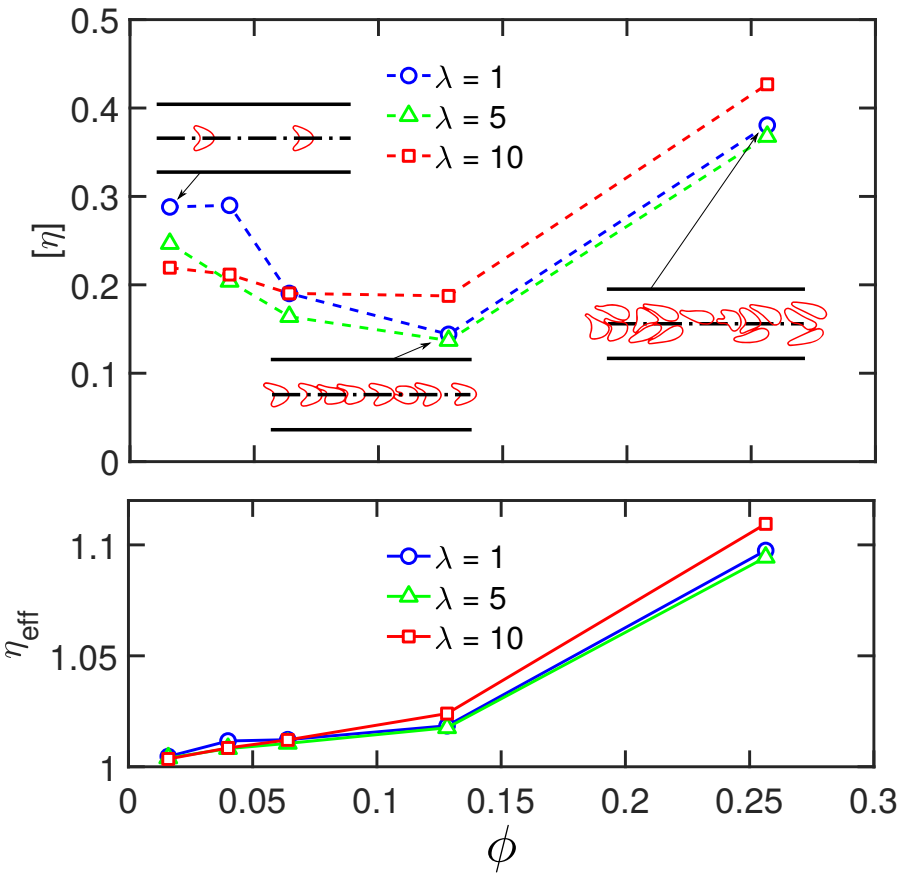

Figure 2.10: $[\eta]$ and η_{eff} as a function of ϕ.

The normalized ($[\eta]$) and the effective (η_{eff}) viscosities are plotted as a function of concentration (ϕ) for different viscosity contrasts, $\lambda = 1$, 5 and 10 (see Fig. 2.10). The other parameters are fixed as to $Ca = 80$, $W = 7$ and $L = 8W$. The number of vesicle are n_{ves} = 2,5,8,16 and 32, corresponding to $\phi = 0.016$, 0.04, 0.064, 0.128 and 0.256. Simulations are initiated with well relaxed vesicle shapes with random positions within the channel. Figure 2.10 (top panel) shows the normalized viscosity (which is a direct information on the effect of vesicle presence, related to the induced flow) as a function of ϕ. An interesting feature emerges: $[\eta]$ always decrease with ϕ up to a concentration of about $\phi \lesssim 0.13$. Below we shall provide some intuitive explanation. It is interesting to note that the decrease occurs in a range of concentrations corresponding to microcirculations values (which fall in the range $5 - 20\%$ [Sutera et al., 1970, Popel and Johnson, 2005]). In other words the system tries to reduce dissipation in order to enhance the benefit of oxygen transport.

In order to explain the present behavior, we first refer to our previous results for the case a single vesicle, which should remain valid in the small ϕ regime. For

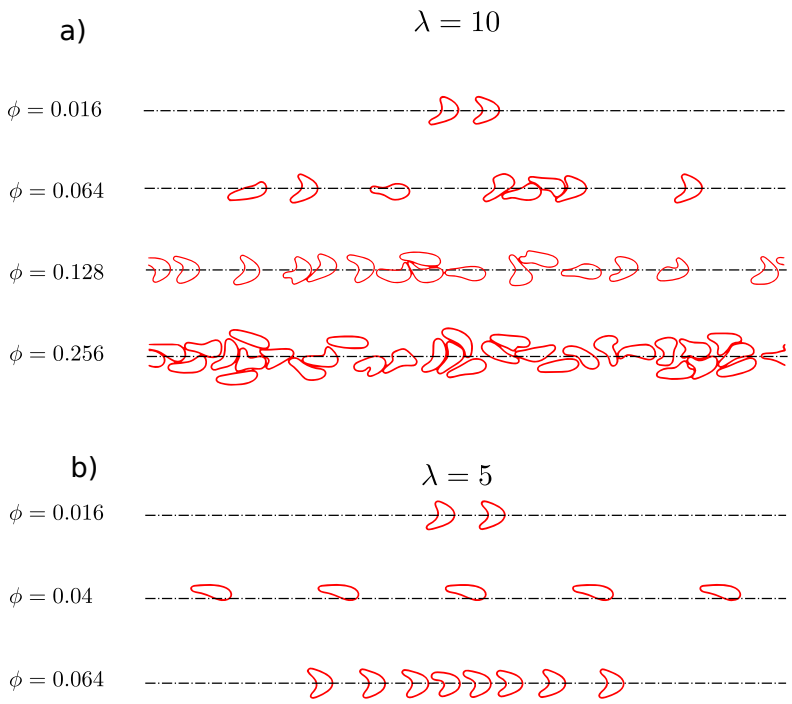

Figure 2.11: (a) Vesicles tend to form a single layer at $\phi \lesssim 0.13$, exemplified by simulation with $\lambda = 10$ (b) Vesicles are attracted by center parachute or near-centered slipper solutions at $\phi = 0.016$ an 0.064, but when $\phi = 0.04$, the off-centered slipper becomes becomes more stable.

$\lambda = 5$, we have observed in the single vesicle study, that the off-centered slipper shape with lateral position $h_f^{(OC)}$ has a larger attraction zone. For $\phi = 0.04$, after all transient effects have decayed, all vesicles form steady a single profile at $h_f^{(OC)}$ position (Fig.2.11b). In other words, the vesicles behave as if they were alone (hydrodynamic interaction among vesicles is weak). We have seen that the slipper (for $W = 7R_0$ and $\lambda = 5$, see Fig2.9), $[\eta]$ is smaller than that of the parachute solution. When adding more vesicles, say two vesicles, their combined induced field is less dissipative than the addition of two isolated vesicles.

2.4 Conclusion

In this work, the dynamical behavior of vesicles in a channel flow (under a Poiseuille flow) is numerically studied. We have found several branches of solutions, such as the centered parachute and slipper, snaking parachute, off-centered slipper, and complex trilobe dynamics. This study highlights the complexity of dynamics, even for the most simple 2D model with an incompressible membrane having only resistance against bending modes. In particular, we have shown that the trilobe shape is not a property

to be linked to membrane cytoskeleton, unlike the claim in [Mauer et al., 2018]. Of course, enriching the model by treating a full 3D model by incorporating the shear elasticity may add an extra layer of complexity, but the existence of the above modes are robust features which do not require further ingredients. We have analyzed the rheology for different concentrations. We have linked the rheology to spatial organization. We have shown that the decrease of the normalized viscosity $[\eta]$ (Fig. 2.10) in the relatively small concentration regime does not occur only in linear shear flow [Thiébaud et al., 2014] but also in the pipe flow, which is more relevant to blood circulation. The origin of the decrease is not attributed to the organization into parallel files of vesicles, but into a more subtle organization. For a dilute suspension the cells tend to select their single-cell solution (slipper) in they gather together in a way that reduce dissipation. The induced flow field in the gap between the two cells benefits for a kind of screening. It is interesting to note that the viscosity decrease occurs in a range of about $0 - 15\%$ which is more or less the range of hematocrit in microcirculation. In some sense, the cells organize themselves in a way to reduce as much as possible the increase of viscosity due to an increase of hematocrit. By this way the cells try to enhance efficiency of oxygen transport. The effective viscosity in this range of concentration increases very slowly (or even shows a tendency of plateau; see Fig.2.10), which is translated into a decrease of the normalized viscosity.

Chapter 3

Development and Validation of The Numerical Solver for Fluid-Membrane-Solute Coupled System

In this chapter we develop the advection-diffusion solver that deals with moving curve boundaries. Diffusion of solutes is commonly present in many biological processes. In the blood micro circulation system, solutes, such as oxygen and calcium molecules, as well as Adenosine Triphosphate (ATP) and biochemical messengers, are released by cells (like red blood and endothelial cells) and then diffuse and are advected by blood flow. In addition, several targeted drug delivery strategies rely on an encapsulation of chemicals and on their release in the blood stream at specific location. These chemicals couple to blood flow, in which red blood cells (RBCs) constitute the major component. Thus, the development of numerical codes which take into account both dynamics of RBCs and their coupling with chemicals is of great importance for many biomedical applications. We develop here a lattice-Boltzmann based solver that deals with generic moving boundary conditions in an advection-diffusion field representing the chemicals. The boundary condition of the solutes at the cell membrane is based on a modified bounce-back scheme. We prove analytically that it enjoys second order precision. In section 3.3 We validated the solver with several examples and then coupled it with a solver for a suspension of RBCs, we developed previously. As a first application we exemplify our method on the problem of liposome drug delivery in arterioles. The results show that for a rigid drug carrier at a scale of about 1 μm, the presence of RBCs facilitates the drug absorption along the vessel wall. We also demonstrate the possibility of applying this solver to the release of chemicals induced

by membrane shear stress, a feature which is omnipresent in mechano-involved signaling processes. As a way of example, we briefly study the problem of ATP release by RBCs. We point out several possible generalizations.

3.1 Introduction

In many biological processes the presence of the cytoplasmic membrane plays an important role regarding molecular and ion (active and passive) transport from the cytoplasm towards the extra cellular environment and vice versa. Examples are abundant in blood circulation. For instance, red blood cells (RBCs) can release oxygen as well as ATP in the microcirculation zone depending, in particular, on the partial oxygen pressure as well as on the cell membrane shear stress [Forsyth et al., 2011, Zhang et al., 2018]. Other examples are encountered in cell signaling processes in blood circulation, such as blood vessel endothelium signaling pathway that modulates vasodilation [Davies, 1995, Yamamoto et al., 2000, Ando and Yamamoto, 2013], or the lymphatic calcium dynamics [Zawieja, 2005, Jafarnejad et al., 2015]. The problem of chemical transport in a flow constitutes also an active field of research in biotechnologies, such as targeted drug delivery which relies on an encapsulation of chemicals within liposomes which are then released at specific sites; the release is triggered either by intrinsic properties (e.g. local shear stress) or by means of an external stimulus (e.g. ultrasound) [Needham et al., 2000, Allen and Cullis, 2013, Akbarzadeh et al., 2013, Sercombe et al., 2015, Kaoui, 2018]. All these examples involve an intimate coupling between blood flow and chemical transport. In other words, the chemical species, besides reactions and diffusion, are advected by the flow. In addition, the chemical species are bound within moving and deformable domains (e.g. RBCs, drug carriers, such as liposomes, etc.) and when released they encounter RBCs as major obstacles in the blood. This problem requires handling the coupling between the moving boundaries, the flow field and chemical transport with specific boundary conditions on the membranes of the suspended entities (e.g. liposomes, RBCs) which describe the criterion dictating the chemical release. For example, some protein channels may open or not regarding ATP release from RBC, depending on the local shear stress, and so on [Forsyth et al., 2011, Zhang et al., 2018]. This task is, in its full generality, quite complex and presents several numerical and conceptual challenges to be described below.

The main purpose of this chapter is to propose an advection-diffusion method in a domain which contains a suspensions of deformable particles (like RBCs or li-

posomes). The method (and its numerical implementation) should handle both the evolution equations of the fluid flow (Navier-Stokes equations) and of the chemicals (advection/diffusion equations) inside and outside the suspended particles, which constantly move and deform in response to hydrodynamics forces (and possibly due to an external stimulus). This problem will be formulated and solved by a lattice Boltzmann method (LBM). The solution of the pure fluid flow by LBM has now become quite classical [Zou and He, 1997, He and Luo, 1997, Chen and Doolen, 1998, Succi, 2001, Mohamad, 2011, Krüger et al., 2017]. The diffusion/advection problem is now becoming an emerging field of research from both physical and numerical aspects [Mohamad, 2011, Krüger et al., 2017, Huang et al., 2009, Lee et al., 2010, Markl and Körner, 2015, Chen et al., 2013a]. To the best of our knowledge, a LBM with general moving boundary with Dirichlet (the boundary concentration is specified) / Neumann (the normal derivative is specified) / Robin (a linear combination of boundary concentration and its normal derivative is specified) condition has not been addressed yet.

We will develop here a LBM for the diffusion-advection problem and couple it with the fluid solver. The formulation of the coupling of the fluid flow to the chemicals adds an extra layer of complexity. A formidable task is to properly handle the chemical boundary conditions on a curved and moving interface (the cell membrane). We will see that both the curvature as well as the moving boundary character pose a challenge. The difficulty arises from the fact that the chemical concentration can be discontinuous at the boundary, unlike the velocity field which is continuous and where the so-called immersed boundary method (IBM) has been successfully applied. Except for some specific situations (the diffusion profile is smooth; the profile has a finite thickness across the membrane) [Peskin, 2002, Feng and Michaelides, 2004, Yang et al., 2009, Huang et al., 2009, Lee et al., 2010, Lee et al., 2010, Chen and Lai, 2014], the use of IBM for general problems remains to be shown.

A generic type of boundary conditions at the membrane that we will deal with is the so-called Robin boundary condition. Attempts to resolve general Robin boundary condition by LBM on static curved boundary have been made [Gebäck and Heintz, 2014, Zhang et al., 2012, Chen et al., 2013b, Li et al., 2013, Huang et al., 2016]. In these cases the handling of boundary conditions requires both a complex interpolation strategy and local curvature information, which obstructs its parallel implementation for arbitrary moving curved boundaries. In [Huang and Yong, 2015], Huang et al proposed a scheme for general Robin condition on piecewisely linear segments (which are parallel to the mesh segment) with second order precision. The formulation of

the boundary condition is derived via asymptotic analysis [Junk et al., 2005, Yoshida and Nagaoka, 2010], and requires only local information. Later on in [Huang et al., 2016] an extension of this scheme for curved boundaries with second order precision has been proposed. However, this scheme turned out to present a complicated interpolation strategy which is shape-dependent and requires information on the local curvature. This strategy is difficult to adopt for a moving boundary problem due to the tremendous number of information needed at each time step. This makes the scheme practically quite inefficient, or even unfeasible for some particular shapes (e.g. triangles where the curvature is undefined at the vertex).

In order to circumvent the problem of inefficiency for parallel implementation and challenges raised by some specific shapes for moving boundaries, we have developed, by still adopting the general Robin boundary condition scheme from [Huang and Yong, 2015], an interpolation scheme which is simpler than in [Huang et al., 2016]. Indeed, our scheme takes into account only a single neighboring lattice point to the membrane, instead of several lattice points [Huang et al., 2016]. It will be shown here that the simplified version enjoys the same precision as the method of [Huang et al., 2016], but at the same time it offers the possibility of efficient (parallel efficiency) and robust handling of arbitrary and moving boundaries.

In addition to the above complexity due to boundary shape, the motion of the boundary in itself raises another problem. Indeed, in the course of time lattice points belonging to a domain lying on one side of the membrane may shift to the other side, and vice versa. Thus, we must identify at each time step the points which have been swept by the moving boundary. This requires an interpolation and / or extrapolation scheme in order to properly reset the values of the concentration field (in the classical fluid-structure interaction problem , this is the so-called refilling procedure [Lallemand and Luo, 2003]). Our method is similar in spirit to this, but with some improvement.

Due to the general complexity of the problem we will focus here on a 2D geometry. The implementation of the chemical problem in LBM is based on the so-called D2Q5-BGK model (2 dimensional, 5 velocity and Bhatnagar-Gross-Krook single relaxation time). To efficiently exploit the parallelization benefit of LBM, the implementation is fully based on a graphic processing unit (GPU) parallel architecture, namely Compute Unified Device Architecture (CUDA). Several tests are performed in order to demonstrate the precision and validity under static and moving boundary conditions.

After having performed several validation tests, we integrate this solver into a well-validated immersed-boundary coupled Navier-Stokes LBM solver [Shen et al., 2017a]. We then present two main applications: (i) we study the liposome drug

delivery (caused by an external stimulus) problem and analyze the main outcome. Recent studies on this problem have focused on the mixing effect [Kabacaoğlu et al., 2017, Kaoui, 2018] for a given velocity field (i.e. without coupling the membrane dynamics to the solute). Another study has analyzed advection-diffusion under steady flow for a given shape (a cylinder) [Gekle, 2017]. Here we extend these studies to the case where the suspended entities (e.g. model of RBCs) are both deformable (free moving boundaries) and coupled to the advection-diffusion of the solute. We find that the coupling to the RBCs significantly affects the results regarding the drug adsorption at the vascular wall. (ii) We shall adapt the method to the case where the membrane boundary condition depends on the local shear stress, with the aim to analyze mechano-involved signaling process in micro-circulation. Of particular interest is the problem of ATP release from RBCs that will be briefly analyzed.

3.2 Methods

Since the problem of solving the Navier-Stokes equations by LBM has by now become quite classical [Zou and He, 1997, He and Luo, 1997, Chen and Doolen, 1998, Succi, 2001, Mohamad, 2011, Krüger et al., 2017], we will focus on the convection-diffusion problem, and only briefly recall the LBM for the fluid when needed. The proposed method can handle several solutes which are coupled to each other. However, for ease of presentation we will consider a single solute only. In addition, we will restrict ourselves to a two dimensional domain (denoted as 2D), and thus our model of RBC will be a 2D contour made of an inextensible membrane. It will be recognized that a generalization to many solutes, as well as to 3D, is straightforward. Let c denote the concentration of a given solute that depends on space and time. In its full generality c obeys the following equation

$$\frac{\partial c}{\partial t} + \mathbf{u} \cdot \nabla c = \nabla \cdot [D(t, \mathbf{x}) \nabla c] + R(c, t, \mathbf{x}) \tag{3.1}$$

$\mathbf{u}$ is the velocity field (supposed to be known for the moment), $t \in \mathbb{R}^+$ and $\mathbf{x} \in \mathbb{R}^2$ are time and spatial coordinates, respectively. For simplicity, we assume here that the diffusion coefficient D is constant. The reaction term R can be handled (see below) within the LBM method, albeit we will not investigate here any application involving reaction. A non-overlapping moving boundary (say a RBC model in 2D) curve is explicitly defined as $\mathbf{B}(t, s) = [X(t, s), Y(t, s)]$, here X and Y are Cartesian components of a given membrane point, s is a scalar parameter, which can typically

be chosen as the local arc length. By adopting the non-slip condition assumption at the membrane, the boundary is advanced by the adjacent fluid velocity

$$\frac{\partial \mathbf{B}}{\partial t} = \mathbf{u}(t, \mathbf{B}) \tag{3.2}$$

If s is chosen as the local arc-length, the normal vector of the boundary is defined as $\mathbf{n}(t,s) = [-\partial Y/\partial s, \partial X/\partial s]$, while tangential vector is defined as $\mathbf{t}(t,s) = [-\partial X/\partial s, -\partial Y/\partial s]$

The solute concentration c and the corresponding flux $\mathbf{J} = \mathbf{u}c - D\nabla c$ are, in general, discontinuous at the boundary. By defining $c^{\pm}(\mathbf{B}) = \lim_{\epsilon \to 0^{\pm}} c(\mathbf{B} + \epsilon \mathbf{n})$, ($c^{\pm}$ in short), the general Robin boundary condition (an equation which combines both Neumann and Dirichlet conditions) along the two sides of the moving boundary $\mathbf{B}$ can be written as

$$\begin{cases} \alpha_1^+ c^+ + \alpha_2^+ \mathbf{n} \cdot \nabla c^+ = \alpha_3^+ \\ \alpha_1^- c^- + \alpha_2^- \mathbf{n} \cdot \nabla c^- = \alpha_3^- \end{cases} \tag{3.3}$$

A schematic of the moving boundary and some definitions are shown in Fig. 3.1a.

3.2.1 Advection-Diffusion Lattice Boltzmann Method

We adopt the so-called D2Q5 BGK model (2 dimensional 5 velocities and a single relaxation time) to formulate a convection-diffusion lattice Boltzmann scheme. Compared to the classical D2Q9 models (used for the fluid solver [Zou and He, 1997, He and Luo, 1997, Chen and Doolen, 1998, Succi, 2001]), D2Q5 requires a smaller memory usage and lends itself to an easier treatment for the geometry of the moving boundary, both of which are important for acceleration in a GPU parallel context. In addition, there are numerical evidences that D2Q5 may enjoy a better stability against D2Q9 for the diffusion problem in some particular situations such as at low or intermediate Peclet numbers [Li et al., 2017, Suga, 2006].

Let Δx and Δt denote the spatial and temporal mesh sizes, the discrete micro velocities are defined as

$$\begin{bmatrix} \mathbf{c}_0 & \mathbf{c}_1 & \mathbf{c}_2 & \mathbf{c}_3 & \mathbf{c}_4 \end{bmatrix} = \begin{bmatrix} 0 & 1 & -1 & 0 & 0 \\ 0 & 0 & 0 & 1 & -1 \end{bmatrix} \frac{\Delta x}{\Delta t} \tag{3.4}$$

This notation means that the velocity $\mathbf{c}_i$ has its components in the $x-y$ plane given by the ith column of the matrix. We will define a particular speed as $c_s = (\Delta x/\Delta t)/\sqrt{3}$ (which would be called the sound speed in the traditional fluid problem, but here

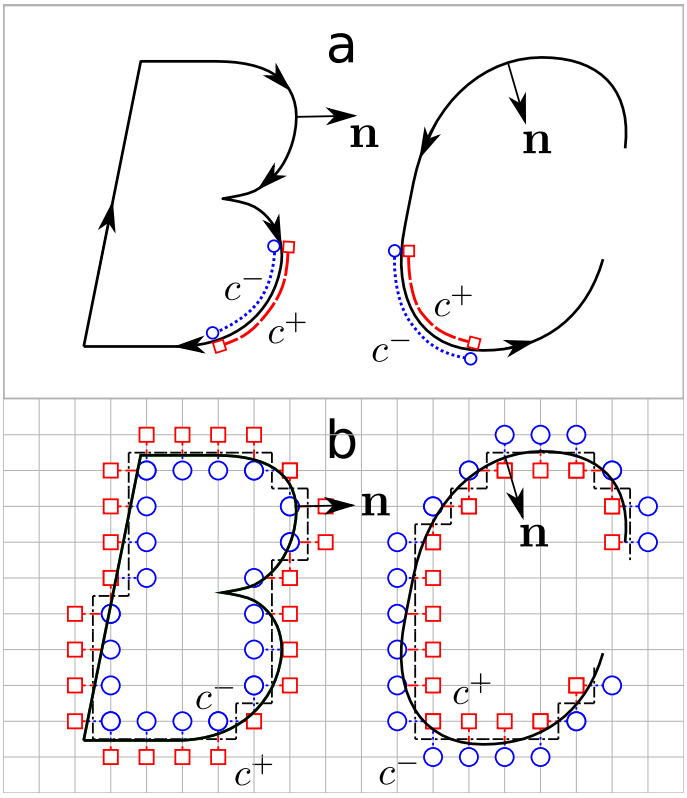

Figure 3.1: A schematic of the convection-diffusion problem in the presence of a moving boundary: a) physical boundary $\mathbf{B}(t, s)$ is piecewisely continuous with countable discontinuities in its derivative. Boundary conditions expressed by Eq. (3.3) are imposed along each side of the curve. Arrows along the curve show the monotonously increasing direction of s. b) Geometrical information of the physical boundary which is discretized into a series of boundary pairs (a square and a circle which are located on the nearest lattice points from the boundary). Boundary conditions are reinterpreted on the zigzag (dash-dot) line

it only has a formal analogy). The direction of $\mathbf{c}_i$ is defined by the unit vector $\hat{c}_i = \mathbf{c}_i/|\mathbf{c}_i|$.

Denoting the micro distribution function as $g_i(t, \mathbf{x})$, its temporal evolution follows the two main steps:

(i) the collision step

$$g_i^*(t, \mathbf{x}) = g_i(t, \mathbf{x}) + \frac{1}{\tau}\left(g_i^{eq} - g_i(t, \mathbf{x})\right) + w_i \Delta t R \tag{3.5}$$

(ii) and the streaming step

$$g_i(t + \Delta t, \mathbf{x}) = g_i^*(t, \mathbf{x} - \mathbf{c}_i \Delta t) \tag{3.6}$$

Here g_i^* is known as the post-collision distribution function, w_i is the weight factor valued as $w_0 = 1/3$ and $w_{1,2,3,4} = 1/6$, and $\tau = 3D{\cdot}(\Delta t/\Delta x^2){+}1/2$ is the dimensionless relaxation time. The equilibrium distribution function is

$$g_i^{eq} = w_i c \left[1 + \frac{\mathbf{u} \cdot \mathbf{c}_i}{c_s^2}\right] \tag{3.7}$$

which depends on the macro concentration c and velocity $\mathbf{u}$. The relation between the micro distribution function and the macro concentration is simply given by

$$c = \sum_{i=0}^{4} g_i \tag{3.8}$$

It is proven via an asymptotic analysis (see [Yoshida and Nagaoka, 2010, Huang and Yong, 2015] and Appendix A.1) that Eqs. (3.5)-(3.7) converge to the convection-diffusion Eq. (3.1) with a second-order precision when $\Delta t/\Delta x^2 \sim O(1)$. A brief derivation is provided in Appendix A.1. We define the dimensionless diffusivity and velocity (in the lattice Boltzmann units) as

$$\begin{aligned} D^{'} &= D \cdot \Delta t/\Delta x^2 \\ \mathbf{u}^{'} &= \mathbf{u} \cdot \Delta t/\Delta x \end{aligned} \tag{3.9}$$

The relaxation time τ and $D^{'}$ are related by (see Appendix A.1)

$$\tau = 3D^{'} + 1/2 \tag{3.10}$$

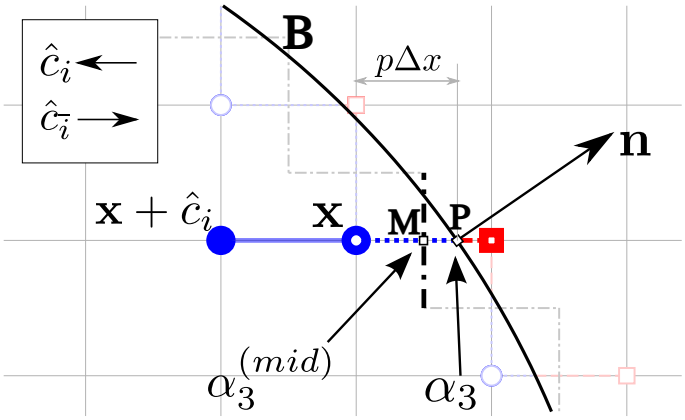

Figure 3.2: A typical boundary lattice is highlighted as the hollow circle. $g_i(t, \mathbf{x})$ is to be calculated from boundary condition (see text). The curved boundary needs to be interpolated onto the zigzag boundary (dashed-doted line). This process is done via finding a value $\alpha_3^{(mid)}$ imposed on zigzag boundary which is consistent with $c = \alpha_3^{(mid)}$ (Dirichlet) or $\partial c/\partial \hat{c}_{\bar{i}} = \alpha_3^{(mid)}$ (Neumann) on the curved boundary value problem. $\hat{c}_i$ is the unit vector parallel to $\mathbf{c}_i$, $\hat{c}_{\bar{i}} = -\hat{c}_i$.

3.2.2 General Moving Boundary Condition Treatment

Since the boundary treatments on both sides of the membrane (Fig. 3.1) are identical from the technical point of view, we only discuss the handling of c^-. Thus below, we omit "±" sign in (3.3). We will split the general Robin boundary conditions given by Eq. (3.3) into two pieces (and then combine them in the general case). The first one is the Dirichlet condition written as

$$c = \alpha_3 \quad (\alpha_1 = 1, \alpha_2 = 0) \tag{3.11}$$

and the second one is the Neumann condition written as

$$\frac{\partial c}{\partial \mathbf{n}} = \alpha_3 \quad (\alpha_1 = 0, \alpha_2 = 1) \tag{3.12}$$

3.2.2.1 Treatment for Static Curved Boundary

The moving boundary treatment is composed of two steps. The first one is to deal with the shape itself at a given moment (a static boundary), while the second one consists in reconstructing the boundary lattice points when they flip from one side of the membrane to the other due to the motion of the free boundary.

The static boundary treatment follows closely (with some important modifications; see below) that given in Refs. [Huang and Yong, 2015, Huang et al., 2016]. The authors there first extended the halfway bounce-back scheme (known for fluid

solvers) to the convection-diffusion LBM. This modified scheme is suitable for the type of the boundary shown by the dashed-dotted lines in Figs. 3.1 b and 3.2). For that boundary (which will be called hereafter *zig-zag* boundary) all its intersecting points with the lattice mesh segments are defined at the middle of the mesh segments (dashed-dotted lines in Figs. 3.1 b and 3.2; **M** is one representative point). Since this scheme requires only local information, it lends naturally itself to an efficient parallel implementation.

Recall that in Fig. 3.1 a physical boundary is discretized into a series of boundary pairs. Assuming there is a boundary lattice point that resides at position $\mathbf{x}$ (see Fig. 3.2, the hollow circle and hollow square provide an example of a typical boundary pair), due to the existence of boundary B, the distribution function $g_i(t+\Delta t, \mathbf{x})$ cannot be determined from streaming Eq. (3.6). Indeed, if $\mathbf{x}$ is the hollow blue circle, then the streaming operation given by Eq. (3.6) (where the argument of the right hand side is $\mathbf{x} - \mathbf{c}_i\Delta t$) would propagate the information from the hollow red square to the hollow blue circle (see Fig. 3.2). The streaming procedure will fail due to the presence of the boundary, and thus the determination of the evolution of g_i at a boundary point, designated by $\mathbf{x}$, requires a special treatment.

The concentration field (or its normal derivative) is specified at the real boundary (a representative point is **P** in Fig. 3.2) to be equal to α_3 (for Dirichlet boundary condition). The discretized boundary has a representative point denoted as **M**, at which the concentration (still unknown) is denoted as $\alpha_3^{(mid)}$. Below we show how is this value determined from α_3 and the concentration field at point $\mathbf{x}$. Once this task is performed, we have at our disposal the concentration field inside the domain of interest, satisfying the boundary condition. The idea is then to use the Boltzmann equation in order to determine the sought-after micro-distribution appearing on the left hand side of Eq.(3.6) as a function of the post-collision distribution at point $(t, \mathbf{x})$ and the macro concentration field at the discretized boundary (Eq. (3.13)). The proof is given in the Appendix A.2 and the result is given by (for Dirchlet and Neumann conditions)

$$\begin{cases} g_i(t+\Delta t, \mathbf{x}) = & -g_i^*(t,\mathbf{x}) + & \frac{1}{3}\alpha_3^{(mid)} & \text{for} & c = & \alpha_3^{(mid)} \\ g_i(t+\Delta t, \mathbf{x}) = & \frac{1+3\mathbf{u}\cdot\hat{c}_i}{1-3\mathbf{u}\cdot\hat{c}_i} g_i^*(t,\mathbf{x}) + & \frac{D'\Delta x}{(1-3\mathbf{u}\cdot\hat{c}_i)}\alpha_3^{(mid)} & \text{for} & \hat{c}_i\cdot\nabla c = & \alpha_3^{(mid)} \end{cases} \tag{3.13}$$

The streaming equation given by Eq.(3.6) is substituted by the above equation for any lattice point $\mathbf{x}$ lying next to the boundary. Our analysis presented in Appendix

A.2 shows that the scheme has a second-order precision. This is consistent with the direct numerical estimates [Huang and Yong, 2015].

Let us now show how to determine $\alpha_3^{(mid)}$. An interpolation procedure was developed in [Huang et al., 2016] for such a purpose, but it requires information from several lattice points. In addition, the selection of interpolating points is geometry-dependent. A simpler procedure is required for a practical implementation of moving boundaries and parallel computation. Here, we only use a single neighboring lattice point ($\mathbf{x} + \mathbf{c}_i\Delta t$ in Fig. 3.2).

Interpolate $\alpha_3^{(mid)}$ for Dirichlet condition

We perform a simple linear interpolation. Let us define the normalized distance p (Fig. 3.2) between points $\mathbf{x}$ and $\mathbf{P}$. The idea is to use the concentration gradient at $\mathbf{x}$ at previous time step to linearly interpolate $\alpha_3^{(mid)}$ out of the concentration field (or its derivative) at the real boundary (where $c = \alpha_3$ for a Dirichlet condition) and at $\mathbf{x}$. The concentration at point $\mathbf{M}$ and at time $t + \Delta t$ is given by

$$\alpha_3^{(mid)} = \begin{cases} \alpha_3 + (p - \dfrac{1}{2})\Delta x \hat{c}_i \cdot \nabla c(t, \mathbf{x}) & \text{if} \quad p \leq \dfrac{1}{2} \\ \dfrac{\alpha_3}{2p} + (1 - \dfrac{1}{2p})c(t, \mathbf{x}) & \text{if} \quad p > \dfrac{1}{2} \end{cases} \tag{3.14}$$

This interpolation has a second-order precision. The separation into two cases ($p > 0.5$ and $p < 0.5$) is dictated by numerical stability.

Asymptotic analysis shows that the concentration gradient can be reconstructed locally in terms of the micro-distribution with one-order precision procedure [Yoshida and Nagaoka, 2010, Huang et al., 2016]

$$\nabla c = \frac{1}{\Delta t c_s^2} \left[\mathbf{u}c - \sum_{i=0}^{4} \mathbf{c}_i g_i \right] + O(\Delta x) \tag{3.15}$$

Interpolate $\alpha_3^{(mid)}$ for Neumann condition

Since the zigzag boundary has its normal vector $\hat{c}_{\bar{i}}$ which is different from $\mathbf{n}$, the reconstruction of $\alpha_3^{(mid)}$ involves tangential derivative as well. It is easily seen that

$$\begin{aligned} \alpha_3^{(mid)} &= \frac{\partial c}{\partial \hat{c}_{\bar{i}}} \\ &= \hat{c}_{\bar{i}} \cdot \mathbf{n} \left.\frac{\partial c}{\partial \mathbf{n}}\right|_{\mathbf{M}} + \hat{c}_{\bar{i}} \cdot \mathbf{t} \left.\frac{\partial c}{\partial \mathbf{t}}\right|_{\mathbf{M}} \end{aligned} \tag{3.16}$$

The normal derivative at **M** can be obtained from **P** and first order extrapolation from **x**,

$$\left.\frac{\partial c}{\partial \mathbf{n}}\right|_{\mathbf{M}} = \begin{cases} \alpha_3 + (p-\frac{1}{2})\left(\left.\frac{\partial c}{\partial \mathbf{n}}\right|_{\mathbf{x}} - \left.\frac{\partial c}{\partial \mathbf{n}}\right|_{\mathbf{x}+\hat{c}_i}\right) & \text{if } p \leq \frac{1}{2} \\ \frac{\alpha_3}{2p} + (1-\frac{1}{2p}) \cdot \left.\frac{\partial c}{\partial \mathbf{n}}\right|_{\mathbf{x}} & \text{if } p > \frac{1}{2} \end{cases} \tag{3.17}$$

The tangential derivative of c at point **M** is unknown, so we will express it in terms of the value at **x** and at the neighboring point $\mathbf{x} + \hat{c}_i$. A linear extrapolation yields

$$\left.\frac{\partial c}{\partial \mathbf{t}}\right|_{\mathbf{M}} = \left.\frac{\partial c}{\partial \mathbf{t}}\right|_{\mathbf{x}} + \frac{1}{2}\left(\left.\frac{\partial c}{\partial \mathbf{t}}\right|_{\mathbf{x}} - \left.\frac{\partial c}{\partial \mathbf{t}}\right|_{\mathbf{x}+\hat{c}_i}\right) \tag{3.18}$$

Finally, we consider the general Robin boundary condition, which is a linear combination of Dirichlet (Eq. (3.11)) and Neumann (Eq. (3.12)) boundary conditions. It reads

$$\alpha_1 c + \alpha_2 \frac{\partial c}{\partial \mathbf{n}} = \alpha_3 \tag{3.19}$$

Similar to [Huang et al., 2016], we reduce the Robin condition back to a Neumann problem by approximating the boundary concentration c in the term $\alpha_1 c$ in Eq. (3.19) with its value at previous time step. Since the boundary position is off-lattice (see point **P** in Fig. 3.2), the value of c on the boundary is evaluated with concentration value on the nearest boundary lattice and corresponding gradient information (see Eq. (3.15)). Recalling the diffusive scaling assumption mentioned at the end of section 3.2.1, namely $D' = \frac{\Delta t}{\Delta x^2} D \sim O(1)$, it is obvious that the introduced error by this approximation merely introduces a second order error term.

3.2.3 Treatment of the Moving Boundary

When dealing with an interface two questions arise: (i) how is the interface being advanced in the course of time, and (ii) how is the interface being discretized and the boundary conditions implemented. The first point is quite classical: once the velocity field is known then the interface is simply advected by the local velocity (using Euler scheme). In this case the velocity is defined on the fluid lattice, whereas the interface is off-lattice. In order to transfer the fluid velocity information from the lattice to the interface the immersed boundary method is used [Peskin, 2002, Feng and Michaelides, 2004, Yang et al., 2009, Shen et al., 2017a]. This is what we adopt here. For the diffusion problem, we have to specify how is the boundary condition imposed on the interface. The first step is to determine the discretized interface as

described in Fig. 3.1. This procedure is different from the IBM, since our interface is defined as a geometrical one (a sharp interface description) and not as a thin strip as is the case with the IBM . The reason for this treatment is that, unlike the velocity field, the concentration field (and its derivatives) is generically discontinuous at the interface, so that the IBM is inappropriate for handling this situation with enough precision. Some exceptions are observed for a special type of boundary conditions as described in [Huang et al., 2009, Lee et al., 2010, Lee et al., 2010, Chen and Lai, 2014]. Once the interface is discretized the boundary terms are evaluated and then transfered to the concentration lattice points in order to deal with the LBM at the interfacial region (see Eq. 3.13).

After each interface motion (obtained thanks to the fluid velocity) we have to resolve the problem of points flipping from one side of the interface to the other side. A possible type of treatment is the so-called refilling procedure [Lallemand and Luo, 2003]. In this method, a point which passes from one side to the other has to be connected to new neighbors located on the same new side. The new distribution function value of the point having passed the interface is evaluated as an extrapolation from its new neighbors. Here we will use a similar strategy but in a more refined manner, as described below. Our procedure is dealt with in three steps: (a) at a given time we have configuration shown in Fig. 3.3a with 4 boundary lattices (shown with empty red squares). At this moment the boundary treatment is done as if the boundary were fixed at that configuration. (b) At later time the boundary moves to configuration shown in Fig. 3.3b where, for example, a new boundary point (in addition to the previous four), shown with empty magenta square, enters the domain. In [Lallemand and Luo, 2003] the distribution function of the new boundary point is obtained by extrapolation from its neighbors shown in red in Fig. 3.3b. Our treatment is slightly different. The idea is to ignore first that new point (since we do not yet dispose of the value of its distribution function), and take into account the boundary motion thanks to the new 4 distances that the 4 red square points make with the new boundary position. We then calculate the distances p for each of the boundary neighboring points (p was described previously in Fig. 3.2, and was represented in Fig. 3.3 with a red dashed line) and evaluate the boundary conditions according to Eqs. (3.13 to 3.17). (c) In the third step, we evaluate the distribution function at the new point (shown with a hollow magenta square in Fig. 3.3c) by using information from its neighbors, as explained below.

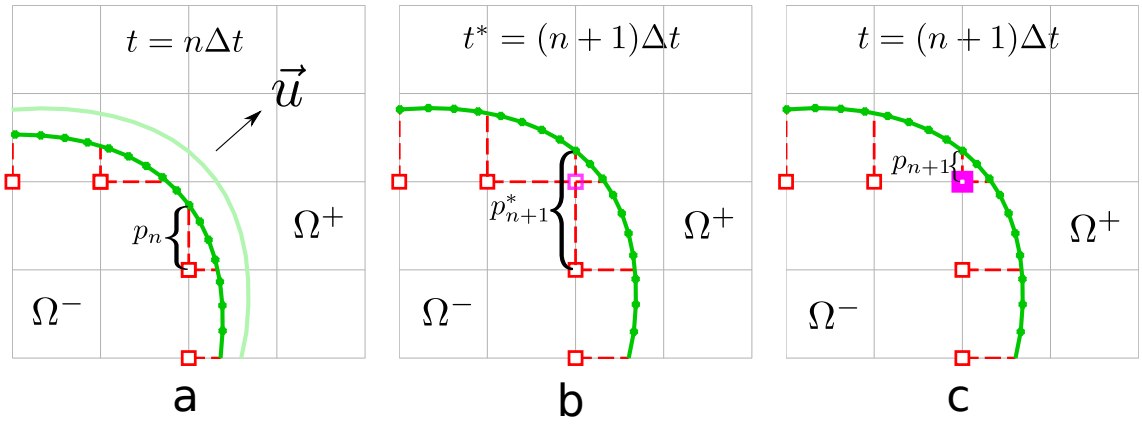

Figure 3.3: The procedures dealing with the moving boundary problem: (a) at that time step, we treat the boundary condition as a static boundary. (b) at intermediate time step, keep the boundary grids fixed, calculate the intersection length p due to boundary movement (defined in Fig. 3.2), and deal with the new boundary condition with the p value (even if it is larger than 1). (c) Search for neighboring lattice points in the set $S^{(ref)}$, and then calculate the new distribution function value via Eq. (3.20)

The natural neighbor interpolation based on Voronoi tessellation [Novak and Slepchenko, 2014] or linear/quadratic interpolation [Lallemand and Luo, 2003] could be implemented. In order not to introduce too many branching operations into moving boundary treatment, we used a simple linear interpolation instead (which lends itself to efficient parallel implementation and is robust even when the membrane undergo high distortions). Our analysis has led us to postulate the following relation for the distribution function at the new points swept by the boundary

$$g_k = \frac{\sum_{k' \in S^{(ref)}} w_{k'} (2g_k(t, \mathbf{x} + \mathbf{c}_{k'}) - g_k(t, \mathbf{x} + 2\mathbf{c}_{k'}))}{\sum_{k' \in S^{(ref)}} w_{k'}} \tag{3.20}$$

Here $S^{(ref)}$ is a collection of subscripts defined on a lattice point , which flipped from Ω^+ to Ω^- in the new time step (see Fig. 3.3). An index k belongs to $S^{(ref)}$ only if both $\mathbf{x}+\hat{c}_k$ and $\mathbf{x}+2\hat{c}_k$ belongs to $\Omega^-(t)$ and $\Omega^-(t+\Delta t)$ in both previous and present time step. We have postulated equation (3.20) from linear extrapolations and a set of intuitive weight factors as defined in section 3.2.1. We have successfully tested these weight factors by a number of numerical experiments (examples of validation will follow). Similar extrapolations (for rigid moving boundaries) were adopted for fluid and solute problems in [Yin et al., 2012, Chen et al., 2013a].

3.3 Validations

3.3.1 Validations with time-dependent problems and static boundaries

3.3.1.1 A pure diffusion problem in an irregular domain

We first validate this boundary condition scheme by treating a time-dependent diffusion problem in the presence of a static boundary. This problem has an analytical solution [Hu et al., 2018]. A periodic square domain is defined as $\Omega = [-1, 1] \times [-1, 1]$, with the presence of an internal boundary

$$\mathbf{B} = [r(\theta)\cos(\theta), r(\theta)\sin(\theta)],\ \theta \in [0, 2\pi)$$

here $r(\theta) = 0.4 + 0.1\cos(3\theta)$. As the internal boundary is closed, it divides Ω into Ω^- and Ω^+, which are the external and internal domains respectively. We focus on the solution in Ω^-. The analytical solution is given by [Hu et al., 2018]

$$c^{(ana)}(t, x, y) = 1 + 0.5\exp\left(-2\pi^2 t D_a\right)\cos(\pi x)\cos(\pi y) \text{ for } (x, y) \in \Omega^-$$

Here D_a is a dimensionless diffusion coefficient in some arbitrary units. Its value is set here to 0.1. The above solution is valid for both Dirichlet and Neumann conditions The above concentration field satisfies the pure diffusion equation with initial condition

$$c|_{t=0} = c^{(ana)}(0, x, y)$$

and a corresponding Dirichlet type boundary condition

$$c|_{\mathbf{B}} = c^{(ana)}$$

or a Neumann type boundary condition

$$\left.\frac{\partial c}{\partial \mathbf{n}}\right|_{\mathbf{B}} = \partial_{\mathbf{n}} c^{(ana)}$$

here $\mathbf{n}$ is the normal vector pointing from Ω^- to Ω^+. We tested numerically both boundary conditions.

The choice of relaxation time τ in simulation is quite flexible. As we have seen in Eq. (3.9) and Eq. (3.10), once the lattice mesh size Δx and relaxation time τ are fixed, the total number of the simulation steps can be given by

$$N^{(step)} = \frac{T}{\Delta t} = \frac{T D_a}{\Delta x^2 D'} = \frac{3 D_a}{\Delta x(\tau - 0.5)} \cdot T$$

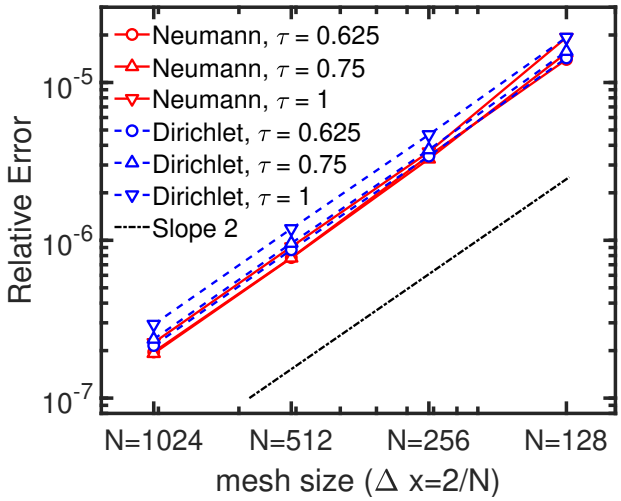

Figure 3.4: The relative error against the mesh size in the static three-leaves problem from [Hu et al., 2018].

For definiteness, we fixed $T = 1$ (in an arbitrary unit). Simulations with different values of relaxation time were tested, namely $\tau = 0.625, 0.75$ and 1. The numerical results are then compared to the analytical solution $c^{(ana)}$ at this particular time $T = 1$. We define the numerical relative error of concentration $c^{(num)}$ as

$$E(\Delta x) = \frac{||c^{(num)} - c^{(ana)}||}{||c^{(ana)}||} \tag{3.21}$$

where $||\cdot||$ is the euclidean norm. A second-order convergence is observed (see Fig. 3.4).

3.3.1.2 An advection diffusion problem in an irregular domain

Secondly, we test this boundary condition scheme against a dimensionless advection diffusion problem in an irregular domain, which has an analytical solution [Huang et al., 2016]. The computational domain is defined as $\Omega = \{(x, y) \in \mathbb{R}^2 | \phi(x, y) < 0\}$, here $\phi(x, y)$ is a scalar field which reads

$$\phi(x, y) = x^4 - 5x^2 - 3x + 2y^4 - 6y^3 - y - 1$$

The time dependent advection diffusion problem is governed by

$$\frac{\partial}{\partial t} c(t, x, y) + \nabla \cdot (\mathbf{u}c) = \nabla \cdot (D \nabla c) + S, \ (x, y) \in \Omega, , \ t \in [0, T]$$

The velocity field is set to be a constant, $\mathbf{u} = (1, 0)$ and D is a constant scalar. The time dependent source term S is

$$S = (x^3 + y^3)\omega \cos(\omega t) + [3x^2 - D(6x + 2)] \sin(\omega t)$$

The initial condition is given as

$$c|_{t=0} = 0,\ (x, y) \in \Omega$$

The boundary condition, which is defined on the zeros of $\phi(x, y)$, can be defined as either Neumann type or Robin type. For Neumann condition, it reads as

$$\left.\frac{\partial c}{\partial \mathbf{n}}\right|_{\phi=0} = (3n_x x^2 + 2n_y y)\sin(\omega t)$$

For Robin condition, it is given by

$$\left.\left(c + \frac{\partial c}{\partial \mathbf{n}}\right)\right|_{\phi=0} = (x^3 + y^2 + 3n_x x^2 + 2n_y y)\sin(\omega t)$$

Here n_x and n_y are components of the normal vector pointing outward. This problem has an analytical solution

$$c = (x^3 + y^2)\sin(\omega t)$$

By following [Huang et al., 2016], we set $D = 1$ and $\omega = 1$. A computational domain $[-3, 3] \times [-2, 4]$ is uniformly meshed into $N \times N$ lattices. For the Robin condition, the value of c on the boundary is obtained by the values at the boundary lattices and the gradient information (see Eq. (3.15)) at previous time step. By choosing different τ and mesh size $\Delta x = 6/N$, the numerical results at $T = 1$ are compared with the analytical solution. A second order convergence is observed (see Fig. 3.5). Despite the fact that there is only a single neighboring point to a given boundary lattice point and no curvature information (recall Fig. 3.2) used in this boundary treatment, the relative error is of the same magnitude compared to the results from [Huang et al., 2016] (recall that in that work several neighboring points and boundary curvature information are employed). The relative error against the different choices of relaxation time τ is gathered in Fig. 3.6. This results suggests a choice for the relaxation time in the range $\tau \leq 1$ (see Fig. 3.6) for all time-dependent problems. Our numerical experiments revealed that this choice favors stability. Indeed, we found that for both Neumann and Robin type boundary condition, simulations with a large relaxation time could be unstable (e.g. $\tau = 3$ and $N = 16$ lead to divergence). We identified that the instability i-results from extrapolation of tangential gradient in Eq. (3.18). Note that omitting the extrapolated term can make the simulation more stable with large relaxation time but the precision of the boundary treatment will degrade down to first-order.

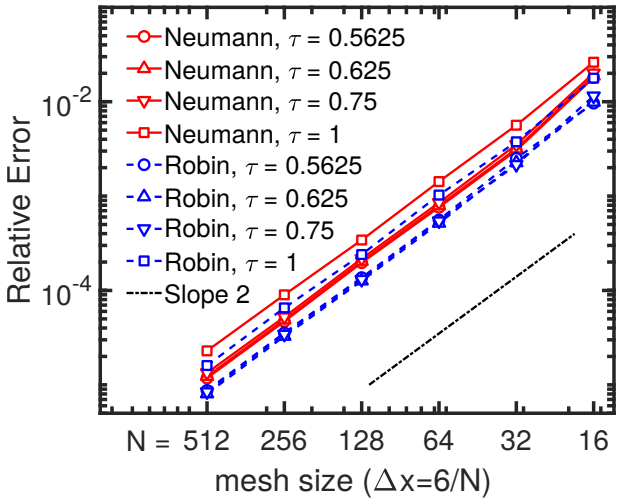

Figure 3.5: The relative error against the mesh size in the advection diffusion problem in an irregular domain from [Huang et al., 2016].

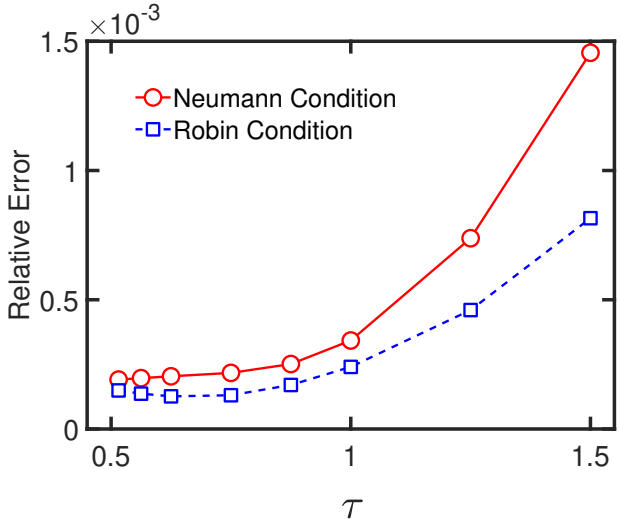

Figure 3.6: The relative error against relaxation time τ in the advection diffusion problem in an irregular domain from [Huang et al., 2016]. The lattice mesh size is fixed as $N = 128$.

3.3.2 Moving Boundary Validation

Now we perform some validation tests on a problem with moving boundaries. The first example is a cylinder (which is a circle in 2D, and contains some solute) advected by a constant velocity. The second case consists of a deformable opaque surface that enclose a solute and which is distorted by a rotational velocity field.

3.3.2.1 An Advected Leaking Reservoir

Consider the dimensionless model in which a cylindrical reservoir is advected by a constant velocity $\mathbf{u}_0$ in a periodic box $\Omega = [-a/2, a/2] \times [-b/2, b/2]$. The boundary of the advected reservoir is described as

$$\mathbf{B}(t, \theta) = [r_0 \cos(\theta) + u_{0x}t, -r_0 \sin(\theta) + u_{0y}t], \ \theta \in [0, 2\pi)$$

where r_0 is the radius of the cylinder. A solute concentration field c is defined on Ω and obeys

$$\frac{\partial}{\partial t}c(t, x, y) + \nabla \cdot (\mathbf{u}_0 c) = \nabla \cdot (D\nabla c), \ (x, y) \in \Omega, t \in [0, T]$$

The initial condition is set as

$$c_{ini} = \begin{cases} 1 & \text{inside reservoir} \\ 0 & \text{outside reservoir} \end{cases}$$

The concentration along the internal and external sides of $\mathbf{B}$ are denoted as $c^-(t, \theta)$ and $c^+(t, \theta)$ respectively. The normal vector points into the outward direction. The solute is leaking from the reservoir into the external zone, and this leakage is described by the following boundary condition at the cylinder surface

$$D\frac{\partial c^-}{\partial \mathbf{n}} = -D\frac{\partial c^+}{\partial \mathbf{n}} = k(c^- - c^+)$$

Parameters are fixed as $r_0 = 0.8$, $a = 4$, $b = 2$, $D = 1$, and $k = 1$. The concentration fields acquired with two different constant velocities $\mathbf{u}_0 = [a/T, 0]$ or $[0, 0]$ are compared at $T = 1$. The contour plots of the numerical solution with $\Delta x = b/512$ is shown in Fig.3.7

The boundary concentration values, c^- and c^+, are evaluated thanks to the concentration values and their gradients at the lattice points (see Eq. (3.15)). Since $\mathbf{u}_0$ is constant, one can infer from Galilean invariance that the actual concentration field in case of $\mathbf{u} = [a/T, 0]$ should be identical to the case with zero advection velocity. However, the numerical errors may affect the Galilean invariance. Therefore, it is

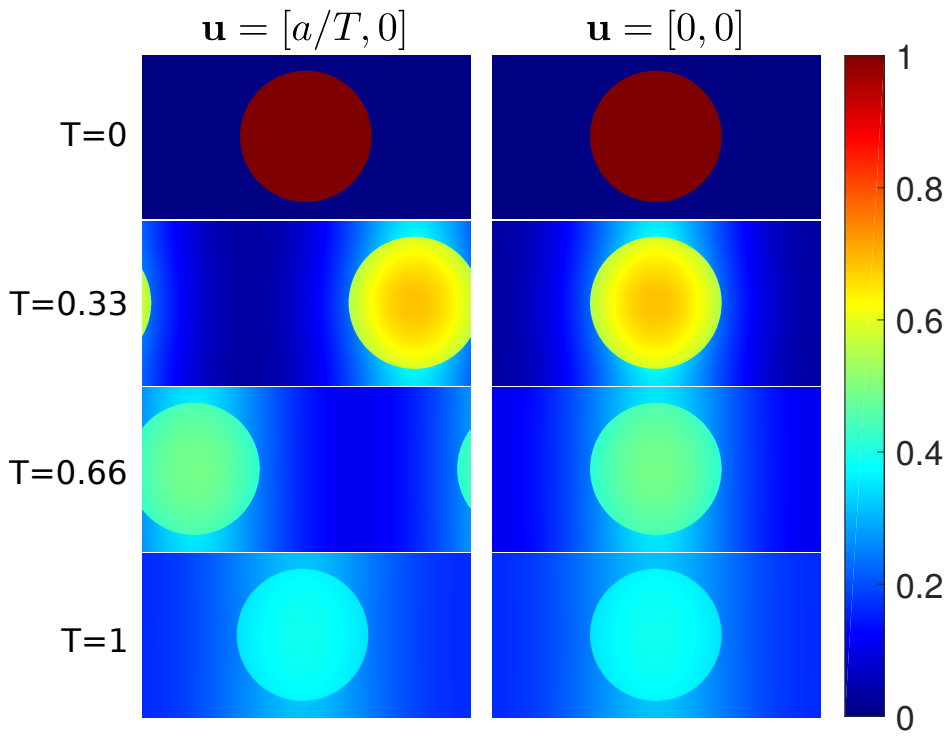

Figure 3.7: Snapshots for the concentration field for $\mathbf{u} = [a/T, 0]$ (left side) and $\mathbf{u} = [0, 0]$ (right side) respectively. In both simulations, we have set $\Delta x = b/512$ and $\tau = 1$. Since the only difference between the left side simulation and the right side one is that the concentration field is advected by a constant velocity, it should be identical to the concentration field on the right side up to a translation (Galilean invariance). This property is accurately reproduced in this simulation, although the LBM is based on an Euclidian mesh. The preservation of Galilean invariance is crucial to scenarios with long term advection such as cell membrane flowing in channels of realistic length.

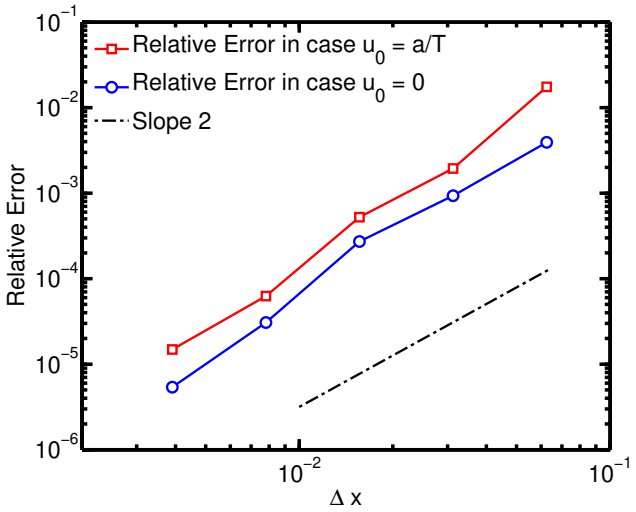

Figure 3.8: Relative error against Δx in the case of a cylindrical reservoir being advected by a constant velocity

important to check if this property is preserved after long simulation time (see the comparison at $T = 1$ in Fig. 3.7). τ is fixed 1 in these simulations. The numerical solution for $\Delta x = b/1024$ and $\mathbf{u}_0 \equiv \mathbf{0}$ is used as a reference solution from which the error is calculated when non zero velocities are considered. A second-order convergence is obtained (Fig. 3.8).

3.3.2.2 A Reservoir that undergoes rotation and distortion

In this case we consider a divergence-free rotational velocity field $\mathbf{u} = [u_x, u_y]$ (see the vector fields in Fig. 3.9 colored in gray) in a simulation box $\Omega = [-1, 1] \times [-1, 1]$.

$$\begin{cases} u_x = & -0.5[1 + \cos(\pi x)] \sin(\pi y) \\ u_y = & \ \ 0.5[1 + \cos(\pi y)] \sin(\pi x) \end{cases}$$

A localized circular reservoir is initially defined with its centroid at $\mathbf{x}_0 = [0.5, 0]$ with radius $r_0 = 0.3$. Its boundary is denoted as $\mathbf{B}$. The reservoir is then subjected to a rotating velocity field, thus, the motion of the reservoir boundary is $\partial\mathbf{B}/\partial t = \mathbf{u}$. A concentration field c is defined on this simulation box, governed by the advection-diffusion equation A zero-flux Neumann condition is imposed on both sides of the reservoir boundary $\mathbf{B}$. A representative Dirac delta function is used as an initial condition $c_0 = \delta(\mathbf{x} - \mathbf{x}_0)$. We set the Peclet number to $Pe = \max(|\mathbf{u}|)/D = 50$. The imposed velocity field is expected to extremely elongate and distort the reservoir. This extreme distortion will constitute an interesting test of the code robustness.

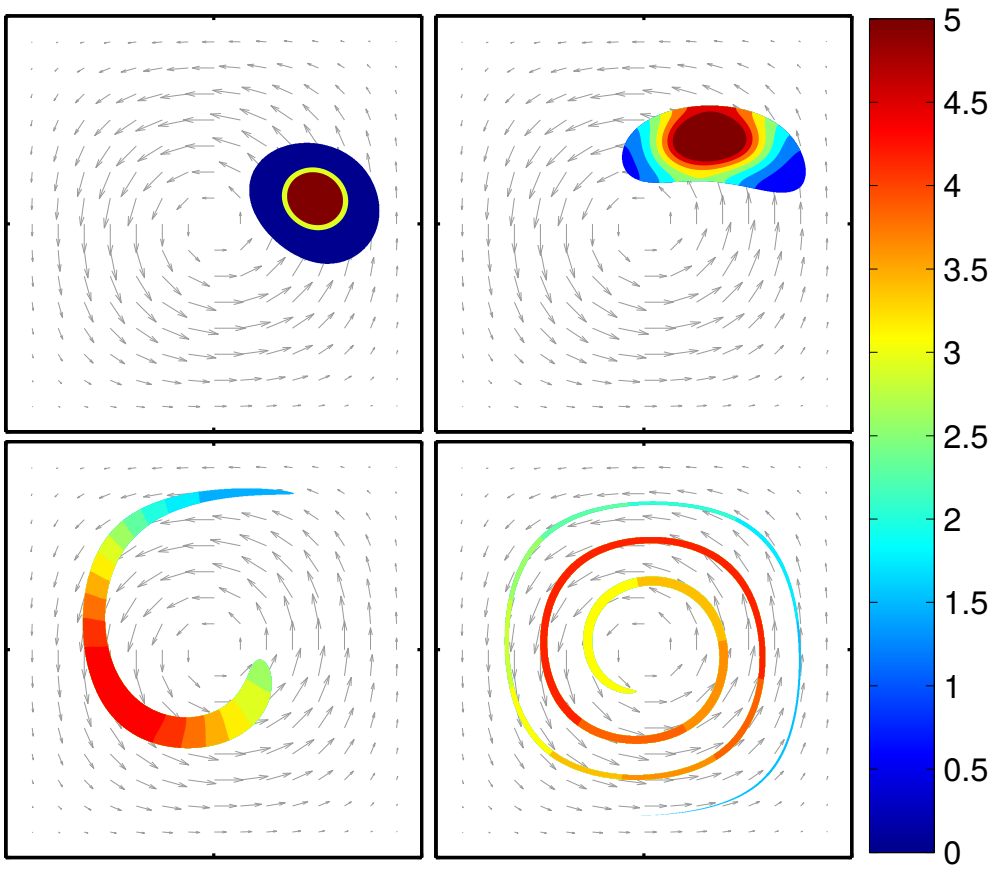

Figure 3.9: From left to right, up to bottom we show the numerical solution of the concentration field at $T = 0.125$, 0.5, 2 and 8, in which $\Delta x = 1/512$. The vector fields in gray represent the rotational velocity field.

The advancing of the distorted reservoir boundary is conducted by means of a $4th$ order Runge Kutta method, under which, the numerical error of reservoir area is adequately suppressed. A numerical solution (obtained with via $\Delta x = 1/512$ and $\tau = 0.75$) is presented in Fig. 3.9. We measure the error at $T = 1$, when the shape is still easily resolvable for lower mesh $\Delta x = 1/16$. The finest mesh $\Delta x = 1/2048$ is used to estimate the relative error calculation (3.21). A convergence rate between first and second order (around 1.45, see Fig. 3.10) is observed. We attribute this to the loss of resolving geometry information when the mesh size is not small enough. For example, in the case where $\Delta x = 1/32$, in Fig. 3.10, the maximum width of the shape is represented by only 7 lattice points, which may cause a significant inaccuracy during the reconstruction process of the zigzag numerical boundary. Despite the relative degradation of the quality of precision (from the expected order 2 down to order 1.5) the code robustly handles extreme distortions, such as the situation shown at $T = 8$ in Fig. 3.9.

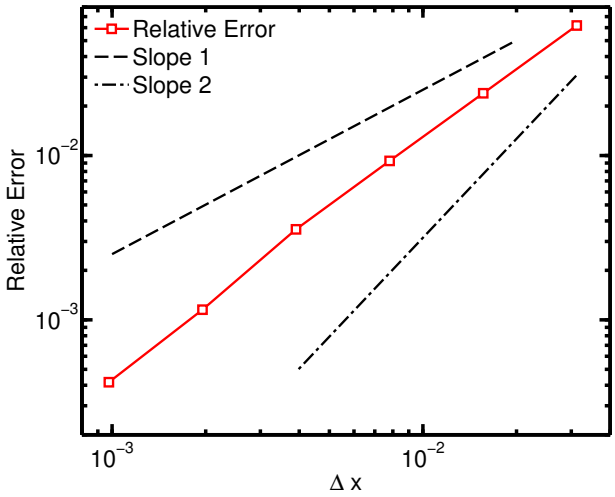

Figure 3.10: Relative error against Δx in the case of a cylindrical reservoir being advected and distorted by a rotational velocity field $\mathbf{u}$

3.4 The Arteriole Thrombosis Drug Delivery Simulation

The validations (section 3.3) have proven that the numerical method's capability of dealing with advection, rotation and distortion of a moving boundary, with even quite ample deformation patterns (or even extreme) under flow. We now implement this solver for the study of a first practical example, the arteriole thrombosis drug delivery. This example is inspired by previous numerical studies on simplified models for liposome drug release in channel flow [Gekle, 2017, Kaoui, 2018]. We consider a liposome that encapsulate some drug to be released in a blood vessel. We take here into account both the plasma fluid and the RBCs.

Liposomes are closed membranes, and are considered as promising targeted drug carriers. They have typical diameters ranging from 100 nm to 1μm [Sercombe et al., 2015]. They are suitable means for carrying hydrophilic drugs to a particular location in the organism where they may release their content thanks to an external stimulus (for example ultrasound excitation) or when the surrounding fluid shear stress reaches a critical value (shear stress is the highest in arterioles). Although there exist various types of liposomes depending on the precise purpose, we consider it here to be composed of a single lipid bilayer. Actually in 2D and for an incompressible membrane there is only a single mode of deformation (bending), and there is no real distinction between different models (vesicle, capsule, red blood cell, etc...).

We consider a straight long channel for the arteriole model, with a Gaussian hill shaped obstacle on one side of the vessel wall to represent the thrombosis (Fig. 3.11). We adopt a 2D vesicle as a crude model for RBCs (we will nevertheless use the abbreviation RBC in what follows). An immersed boundary coupled lattice Boltzmann method is employed to resolve the fluid-membrane coupled system, which means, the motion of the RBCs as deformable boundaries is performed by the immersed boundary method [Peskin, 2002, Feng and Michaelides, 2004, Yang et al., 2009]; for details of the solver we adopted, see [Shen et al., 2017a]. A liposome is initially located at the upstream of a thrombosis site, surrounded by RBCs suspended in the solution. The liposome encapsulates a water-soluble drug with concentration $c_0 = 1$. Its membrane is initially impermeable to the drug. Then the liposome is advected by blood flow until it reaches a particular distance from the thrombosis, where an external stimulus is assumed to make the liposome membrane becoming permeable to solute. After this external excitation, we assume the liposome to become fully transparent to the drug solute. A schematic representation is given in Fig. 3.11 to show the simulation layout.

We would like to evaluate how the flow pattern and the RBCs presence affect the drug delivery process. For that purpose we consider 3 different situations, one without RBCs at all, the second one with passive RBCc (i.e. RBCs are completely transparent to the drug), and finally a realistic case in which the RBCs are opaque to the drug. In all the three cases we consider a complete absorption condition along the vessel walls (zero-value Dirichlet condition). When RBCs are considered as opaque to solute, the boundary conditions at the RBC membrane and at the wall reads

$$\begin{cases} \dfrac{\partial c}{\partial \mathbf{n}} = 0 & \text{on RBCs membrane} \\ c = 0 & \text{on vessel walls} \end{cases} \tag{3.22}$$

When we consider a transparent RBC model, we relax the first above boundary condition.

3.4.1 Preliminaries on the fluid–membrane–solute system

Hereby we simply recall the modeling of 2D membrane problem. A 2D unstretchable closed membrane is used for the RBC model, and has a bending elastic modulus $\kappa_b = 3 \times 10^{-19} J$ [Betz et al., 2009, Kaoui et al., 2011]. The membrane force is obtained from the Helfrich energy

$$H(\mathbf{X}(t,s)) = \frac{\kappa_b}{2} \oint \kappa^2 ds + \oint \zeta ds$$

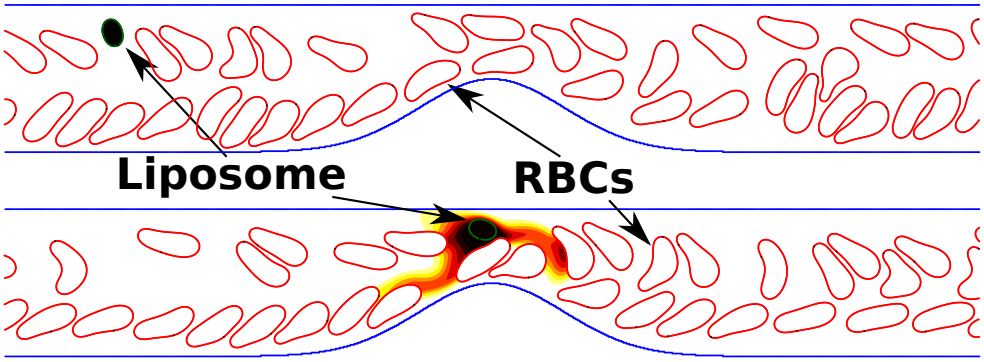

Figure 3.11: A schematic representation of liposome drug delivery process near an arteriole thrombosis. The top panel represents some time before drug release, and the bottom one represents the situation after drug release. The colormap represents the concentration of drug solute. The liposome becomes transparent after it reaches a particular distance from the thrombosis

Here $\mathbf{X}(t,s)$ is the position of RBC membrane, κ is the local curvature, ζ is a Lagrange multiplier that enforces local membrane inextensibility, and s is the curvilinear coordinate. The membrane force (which is obtained as a functional derivative of H with respect to $\mathbf{X}(t,s)$) is applied as a bulk force (albeit localized close to the membrane, in an immersed boundary spirit) to the fluid

$$\rho\left(\frac{\partial \mathbf{u}}{\partial t}+\mathbf{u}\cdot\nabla\mathbf{u}\right)=-\nabla p+\nabla\cdot(\eta\nabla\mathbf{u})+\oint\frac{\delta H}{\delta\mathbf{X}}\cdot\delta(\mathbf{x}-\mathbf{X})ds$$

Then, the velocity field $\mathbf{u}$ is used to advance the membrane shape

$$\frac{\partial \mathbf{X}}{\partial t}=\int\delta(\mathbf{x}-\mathbf{X})\mathbf{u}(\mathbf{x})dxdy$$

We define the Capillary number as $Ca=\mu_{ex}\dot{\gamma}_w R_0^3/\kappa=10$, where η is the fluid viscosity (which is position dependent, so that it can be taken to be different inside and outside of the RBC, if need be; see later). $\dot{\gamma}_w$ is the flow shear rate at channel wall in the absence of thrombosis, liposome and RBC, R_0 is a characteristic radius of the RBC, $R_0=\sqrt{A/\pi}$. A reduced RBC area is defined as $RA=4\pi A/P^2$, A and P are constant area and perimeter, respectively. RA is an index that quantifies the roundness of the RBC, and taken here as $RA=0.7$. For the RBC model we take $R_0=3\mu m$, whereas for the drug carrier (liposome, for which we adopt the same membrane model as the RBC) we take $RA^{(lip)}\approx 0.997$ (a quasi-circular shape) and a radius $R_0^{(lip)}=1.8\mu m$. In the whole simulation we keep the Reynolds number $Re=max(|\mathbf{u}|)R_0^{(ves)}/\eta\approx 0.2$. The channel width and length are $W=7.5R_0^{(ves)}$ and $L=75R_0$, thus the simulation box is $\Omega^{(vessel)}=[-37.5R_0,37.5R_0]\times[-3.75R_0,3.75R_0]$.

The Hematocrit value 31.3% is taken for RBCs, which cor responds to 56 representing cells in the channel. The thrombosis is shaped as

$$y = h_t \cdot exp\left[-\frac{1}{2}\left(\frac{x - L/2}{w_t}\right)^2\right]$$

Here $h_t = 0.5 \cdot W$ and $w_t = W$ are the height and the width of the shape.

Studies [Zhao et al., 2012, Kumar and Graham, 2012, Gekle, 2016, Müller et al., 2016, Krüger, 2016, Guckenberger and Gekle, 2018] have shown that due to the liposomes size, their rigidity and flow conditions, margination effect will drive them to the so called cell-free layer (CFL) near the vessel wall. Our long term simulation also confirmed this tendency. However, in the absence of RBCs, the liposome remains at its initial lateral position while being advected by the flow along the channel. In order to be able to compare the results with those obtained in the case where RBCs are present (and thus margination prevails) we selected the initial liposome position in the CFL, $1.25R_0$ distant from the upper vessel wall. We use the following criterion for drug release: the liposome is impermeable to solute until its centroid reaches a given distance from the thrombosis, below which it becomes transparent. In these simulations we have set that distance to $x^{(permeation)} = -17.5R_0$. We have in mind the situation where the liposome develops small pores that allows solute release, whereas the liposome maintain its overall membrane integrity.

We set $\Delta x = 0.15\ \mu m$ and $Pe = max(|\mathbf{u}|)R_0^{(ves)}/D = 10$ and 100, which corresponds to typical drug solute diffusivities D (10^{-10} and $10^{-11}\ m^2/s$). Prior to the study of interest (0 value Dirichlet condition in Eq.(3.22), we have tested our code with zero-flux boundary condition on vessel walls in order to check numerically the mass conservation. We have found that loss of mass is always smaller than 1.5%.

3.4.2 Results

We show the solute absorption curve by vessel walls for 6 different cases in Fig. 3.12 (a). The normalized absorption level is defined as

$$R(t) = 1 - \frac{\iint c(t)dxdy}{\iint c(0)dxdy} \tag{3.23}$$

The integration is simply treated as summation among all pixels, which will introduce an error term of order 1% magnitude only.

It is found that for both $Pe = 10$ and 100, whether we have transparent RBCs or no RBcs at all (solid lines and dashed lines in Fig.3.12 (a)) the absorption rate

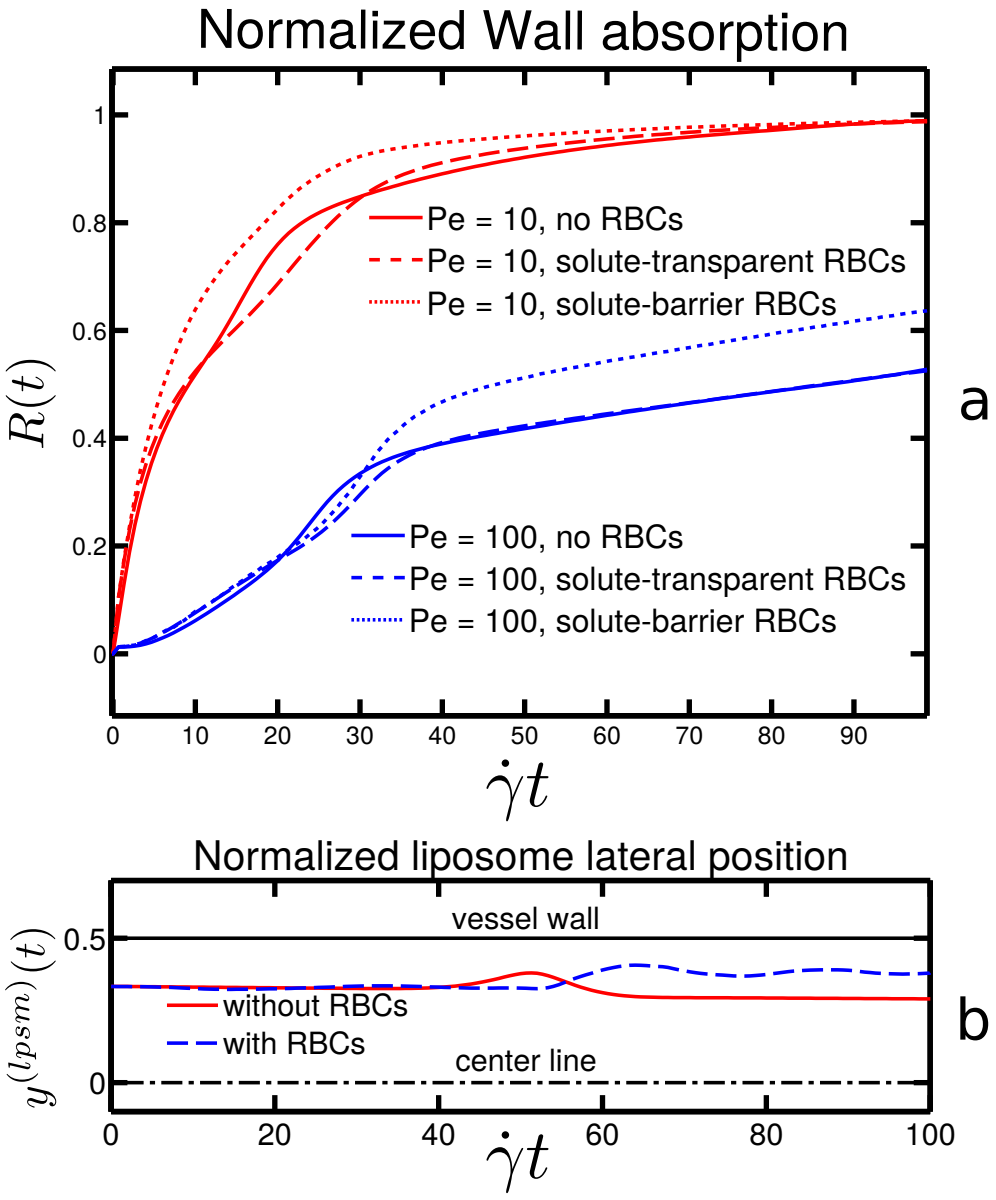

Figure 3.12: (a) The solute absorption rate as a function of time for $Pe = 10$ and 100. (b) The normalized lateral position of the liposome as a function of time with or without RBCs' presence. In both cases the liposome is close to the wall. The vessel wall is at position 0.5 and the center-line at position 0.

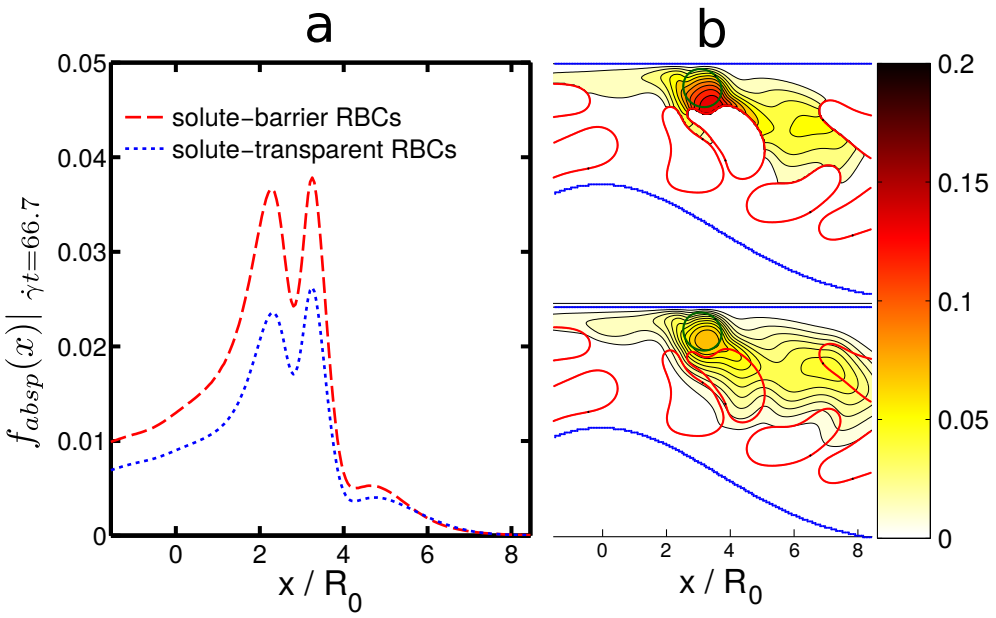

Figure 3.13: (a) The normalized absorption rate along the upper wall, calculated from Eq. (3.24). (b) Corresponding solute concentration distribution at $\dot{\gamma}t = 66.7$, both in the presence and absence of RBC; $Pe = 100$.

is practically the same. We believe this is due to the liposome's lateral position near the vessel wall (Fig. 3.12 (b)), where the normalized distance between liposome centroid and the wall $y^{(lpsm)}(t)$ is always small enough, so that the absorption curve is diffusion-dominated, rather than advection-dominated. However, when RBCs are opaque, we find an increased absorption, shown by dotted lines in Fig. 3.12 (a)). A close inspection suggests that RBCs, as solute barrier, obstruct the diffusion of solute from liposome to the channel center. Consequently the gradient is increased towards vessel wall; is proportional to normalized absorption rate along the upper wall:

$$f_{absp}(t,x) = -\frac{D}{\dot{\gamma}R_0}\frac{\partial c}{\partial y}\bigg|_{y=3.75R_0} \tag{3.24}$$

Figure 3.13 shows the absorption rate together with RBCs configuration and the solute pattern at the thrombus location. Here again, we notice the higher absorption rate due to the presence of RBCs playing the role of solute barriers.

In conclusion, when having high enough Hematocrit (31.3% in this study) and high enough rigidity of liposome which lead to margination, the presence of RBCs facilitates the vessel wall absorption process. This is mainly due to the impermeability of RBC membrane to the solute. One can speculate that increasing of Hematocrit will strengthen the absorption, although further investigations are needed before reaching a definite answer.

3.5 ATP release from Red Blood Cells under Flow Stimulus

The study of mechanosensing of solute release (or the lack thereof) ca be handled by coupling the boundary conditions with other information such as the membrane shear stress. We demonstrate here a possible application of our solver in a fluid-membrane-solute coupled scenario, which is the problem of release of ATP (Adenosine Triphosphate) from RBCs under shear flow. Experimental studies have shown that when RBCs undergo flow originated shear stress, they can release ATP, a universal energy carrier and messenger molecule that plays important role in vessel dilatation [Wan et al., 2008,Forsyth et al., 2011]. It has been shown in [Forsyth et al., 2011] that the amount of ATP release depends on whether RBC undergo tank-treading (TT) or tumbling (TB). In our 2D model a transition from TT to TB can be achieved by varying the viscosity contrast between the internal and the external fluids. A shear flow is generated in a simulation box $[W, L] = [12.5R_0, 25R_0]$ by moving the upper and lower walls with the same speed but opposite direction. The solute (ATP) boundary condition on the upper and the lower correspond to zero-flux condition, with periodic boundary conditions along the flow direction. The RBC is initially located at the center of the shear flow. We define the viscosity contrast as $\lambda = \eta_{in}/\eta_{out}$, here η_{in} and η_{out} are the viscosity of internal and external domain of the RBC. Experiments have shown that viscosity (as well as the shear rate) contrast is a key parameter to the motion of RBCs under shear flow [Fischer et al., 1978a, Tsubota and Wada, 2010, Fischer and Korzeniewski, 2013]. For low enough λ (to be specified below), a vesicle (or 2D RBC) tends to exhibit TT motion, whereas for higher λ TB prevails. We adopt a simplified model of the ATP release, which is a Heaviside step function for shear stress condition (namely, the release takes place only if the local membrane shear stress exceeds a certain value). Thus, the Neumann boundary condition along the membrane for the solute release from RBC towards the external fluid reads

$$D\frac{\partial c}{\partial \mathbf{n}} = \begin{cases} \dot{\gamma}_w/P & \text{if } \sigma > \sigma_0 \\ 0 & \text{if } \sigma \leq \sigma_0 \end{cases}$$

Recall that P is the perimeter of the RBC, $\dot{\gamma}_w$ the wall shear rate, defined in section 3.4. σ is the shear stress along the membrane, defined as

$$\sigma = \eta_{out}\frac{\partial \mathbf{u_t}}{\partial \mathbf{n}}$$

where $\mathbf{u_t}$ is the fluid velocity along the membrane tangent.

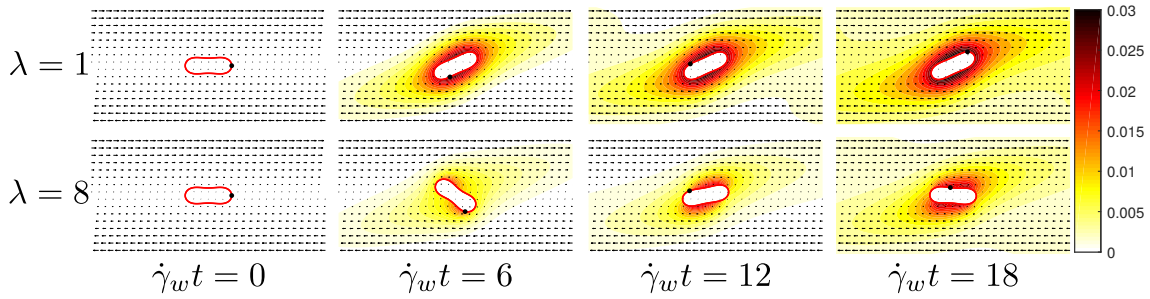

Figure 3.14: ATP fields under different viscosity contrast values. For $\lambda = 1$, the vesicles undergo tank-treading motion, while for $\lambda = 8$, the tumbling motion prevails. In the tumbling regime the release pattern along the membrane is more inhomogeneous, but the overall released concentration is lesser than in the tank-treading regime ($\lambda = 1$).

The critical value of the shear stress is set to $\sigma_0 = 0.07Pa$, and is inspired by *in vitro* experiments [Forsyth et al., 2011]. We use the ATP diffusivity $D_{ATP} = 2.36 \times 10^{-10} m^2/s$, which leads to the Peclet number $Pe = \dot{\gamma}_w R_0^2/D = 1.91$. The ATP concentration field snapshots is shown in Fig. 3.14 with $\lambda = 1$ (TT) and $\lambda = 8$ (TB). Our results show that qualitatively an increase of viscosity contrast reduces the ATP release. In other words, the TB regime triggers less release than the TT one. This finding is consistent with experimental observations [Forsyth et al., 2011]. Actually the problem is more subtle, since not only the local shear stress matters, but also the cell deformation amplitude. By taking into account both effects, we have been able to reproduce both qualitatively and quantitatively the experimental results. An extensive study is devoted to this question in a different publication [Zhang et al., 2018].

3.6 Conclusion

In this chapter, we developed a 2D lattice-Boltzmann based advection-diffusion solver for curved moving boundaries for both Dirichlet, Neumann and linear Robbin boundary conditions. In most cases, a second order convergence is achieved. For highly distorted boundaries, a convergence between first and second order is observed. The boundary scheme requires only one neighboring lattice point with simple strategy, allowing for efficient GPU parallelization.

Since the advection-diffusion solver is designed for generic usage, its implementation for other problems, such as two-sided coupling cases is straightforward. Moreover, the scheme is based on a simple pixelization of curved boundary, with the help

of parallel voxelizer, implying that the extension to 3D is also feasible.

We coupled this solver to a well-validated immersed boundary lattice-Boltzmann fluid-vesicle solver and implemented the resulting code for the study of liposome based hydrophilic drug delivery problem. We confirmed that with an assumption of instant absorption on vessel wall, when the liposome margination effect is strong, the presence of red blood cells facilitates the absorption. We have also demonstrated the potential of using this solver for shear stress induced cell-signaling process, and have exemplified it for the problem of ATP release by RBCs under flow.

Chapter 4

ATP Release by Red Blood Cells Under Flow: Model and Simulations

In this chapter, we discuss the Adenosine Triphosphate (ATP) release from red blood cells (RBCs) under flow. ATP is a major player as a signaling molecule in blood microcirculation. It is released by RBCs when they are subjected to shear stresses large enough to induce a sufficient shape deformation. This prominent feature of chemical response to shear stress and RBC deformation constitutes an important link between vessel geometry, flow conditions, and the mechanical properties of RBCs, all contributing factors affecting the chemical signals in the process of vasomotor modulation of the pre-capillary vessel networks. Several *in vitro* experiments have reported on ATP release by RBCs due to mechanical stress. These studies have considered both intact RBCs as well as cells within which suspected pathways of ATP release have been inhibited. This has provided profound insights to help elucidate the basic governing key elements. Yet how the ATP release process takes place in the (intermediate) microcirculation zone is not well understood. We propose in section 4.3.2 an analytical model of ATP release. The ATP concentration is coupled in a consistent way to RBC dynamics. The release of ATP, or the lack thereof, is assumed to depend on both the local shear stress and the shape change of the membrane. The full chemo-mechanical coupling problem is written in a lattice Boltzmann formulation and solved numerically in different geometries (straight channels and bifurcations mimicking vessel networks) and under two kinds of imposed flows (shear and Poiseuille flows). We show in section 4.3.3 that our model remarkably reproduces existing experimental results. In section 4.4 we pinpoints the major contribution of ATP release when cells traverse network bifurcations. General conclusion is made in section 4.6. This study may aid in further identifying the interplay between mechanical properties and chemical signaling processes involved in blood microcirculation.

4.1 Introduction

ATP is known not only as an energy carrier but also as a prominent signaling molecule in many physiological processes [Khakh and Burnstock, 2009]. A notable example is the case of blood flow where RBCs have the ability to release ATP under several types of stimulus. Experimental evidence [Khakh and Burnstock, 2009] supports the idea that ATP is capable of modulating vasomotor tone in the microcirculation via diffusion towards endothelial cells (ECs) which then in turn elicit a vasodilation reaction cascade of the smooth muscle of the arteriolar trees, without nerve ending intervention. *In vivo* studies [Sprague et al., 1996] confirmed that ATP release by RBCs due to shape deformation played a vital role in pulmonary vascular resistance modulation. In recent years, systematic *in vitro* experimental studies revealed that ATP release by RBCs is quite sensitive to low oxygen level, to shear stress and to sufficiently high shape deformation [Sprague et al., 1998a, Dietrich et al., 2000, Wan et al., 2008, Forsyth et al., 2011]. This mechanical-dependent release is believed to play an important role in the microcirculation, since in these zones (e.g. in arterioles and capillaries) the shear stress is the highest and shape deformations may become quite large. The actual ATP concentration level as well as its heterogeneities (e.g. its gradient) has most likely a potential role in a global and precise understanding of "RBC to EC to smooth muscle" signaling pathway and related pathologies. This is at present a quite ambitious task that is beyond the objective of this study. Rather, here we shall concentrate on the first basic question, on how the geometry of networks, the flow properties and RBC dynamics affect the ATP concentration in microcirculation.

Although direct access to high resolution spatio-temporal ATP concentration patterns in micro-vessel networks is a formidable task, statistical analysis in *in vitro* studies provided some essential key elements. Along this line Forsyth et al. [Forsyth et al., 2011] performed an *in vitro* study in which RBCs were subjected, for a long enough time period, to various levels of shear stress. ATP release was measured subsequently and compared with the amount of ATP obtained under static conditions. By varying the amplitude of the shear stress, two distinct ATP release pathways were hypothesized from previous experimental studies [Sprague et al., 1998b, Chasan et al., 2002, Locovei et al., 2006, Ellsworth et al., 2009, Forsyth et al., 2011]. One pathway is triggered by the amplitude of the shear stress, whereas the second one requires sufficiently large RBCs shape deformation. Both pathways were shown to be shear stress dependent. More precisely, when the shear stress was non-zero but below a

critical value ($3Pa$ in their experiment), most of RBCs perform tumbling (flipping in a shape-preserving manner) with a very limited deformation. In this case, the release level of ATP was quite independent of the amplitude of the shear stress once the threshold value was crossed. Beyond a second critical value of shear stress, a large proportion of RBCs underwent tank-treading motion with large shape deformation. In this case, the total ATP amount showed a monotonic increase with shear stress. Other experimental studies of RBCs passing through a narrow channels [Wan et al., 2008] have also pointed to the fact that when the characteristic shear stress on the RBC increased from around $0.02Pa$ to $0.1Pa$, a release of ATP was observed with a time delay in the range of $20 - 70ms$.

The experimental evidence reporting on the link between membrane shear stress, shape deformation and the level of ATP release, has motivated theoretical studies in an attempt to explain the ATP release mechanism on a molecular level. In [Gov and Safran, 2005], the authors proposed a possible pathway, in which, the deformation creates cytoskeletal defects, from which actin molecules are freed. Subsequently, actin molecules aggregate on cystic fibrosis transmembrane conductance regulator (CFTR) which causes its activation in favor of ATP release. Yet the CFTR is believed to modulate ATP release in an indirect manner, that is to up-regulate the so-called Pannexin 1 hemichannel (Px1). Actually, Px1 is believed to be the main avenue for ATP release from the RBC membrane. It is directly sensitive to mechanical stress, as well as to cytoplasmic oxygen and calcium levels. Experiments have also reported on a presumable mechanism from Piezo1, a cation channel which responds to membrane shear stress by allowing calcium influx [Saotome et al., 2017]. An elevation of calcium level is known to facilitate Px1 activation for intracellular ATP release.

In vivo, RBCs are constantly exposed to flow where they experience various levels of shear stress and deformation. Several numerical studies on RBC dynamics in the circulation reveal nontrivial steady or time-dependent shapes. In [Kaoui et al., 2009], a vesicle model (where the membrane is made of a pure lipid bilayer) was employed to represent the RBC. A complex diagram of single vesicle dynamics was reported later in [Kaoui et al., 2011] and [Aouane et al., 2014b].

Despite the oversimplification of the vesicle 2D model, several similar shapes were also found subsequently in more elaborate 3D models, which included the membrane cytoskeleton [Fedosov et al., 2014, Quint et al., 2017]. This points to the fact that the simplified 2D vesicle problem captures several important RBC shapes and dynamics.

The two main ingredients of this ATP release model are (i) the local shear stress, (ii) the deformation amplitude. Both effects are present in 2D and 3D. We do not expect a qualitative difference between 2D and 3D, since the two modes of motion (Tumbling and Tank-treading) are exhibited in both 2D and 3D. However, we have to keep in mind that the 3D properties of RBC may become essential. For example, RBC is endowed with network of spectrins (cytoskeleton) and that it may undergo large deformation as comaperd to a 2D model. These factors are expected to quantitatively shift the results. To cope with the complex problem of ATP release, we shall adopt here a 2D vesicle model and focus on the most important RBC dynamics related to ATP release, namely the local shear stress and local membrane deformation, leaving more advanced 3D simulations to the future.

Here, our major goal is to propose a model of ATP release and its coupling with membrane shear stress and shape deformation. The basic elements of the model of ATP release are guided by *in vitro* experimental data [Forsyth et al., 2011, Wan et al., 2008] and inspired by the molecular mechanism involving RBC shape deformation [Gov and Safran, 2005]. To the best of our knowledge this is the first model of ATP release from RBC under flow. As we will see, the model is inspired by existing *in vitro* shear experiments and will be validated by reproducing the experimentally observed features.

Once the model is established, we shall use a lattice Boltzmann method to investigate it numerically under microcirculation conditions. A complex issue is the handling of the advection-diffusion problem on a moving and deformable boundary. The implementation of coupling the ATP release to the fluid flow were discussed in chapter 3. We propose an empirical ATP release model which remarkably reproduces the essential ATP patterns reported experimentally under shear flow. This model will be analyzed in a systematic way for different scenarios in the microcirculation. More precisely, we consider a pipe flow with various steady or unsteady shapes of RBC, then the scenario of a RBC hitting a bifurcation, and finally the post-hitting lateral migration and its relation to ATP release. The ATP release is found to show a strong dependence on RBC dynamics. Finally, we present some general conclusions and future directions.

4.2 Methodology

4.2.1 The Model of RBC Dynamics and The Coupling to The Chemical Problem

Under shear flow, both vesicles (in 2D and 3D) and RBCs exhibit two main modes: tank-treading (the cell or vesicle acquires a given orientation while the membrane rotates around the center of mass) and tumbling (a quasi solid-like flipping). The two modes will be denoted as TT and TB, respectively. For vesicles, TB occurs at high enough internal fluid viscosity with respect to the external one, while TT prevails at low enough internal viscosity [Vlahovska et al., 2009]. For RBCs [Fischer et al., 1978b, Tsubota and Wada, 2010, Fischer and Korzeniewski, 2013, Abkarian and Viallat, 2008], the transition from TB to TT can be achieved by increasing shear stress. For low shear stress, RBCs exhibit TB, while for large shear stress, we have TT. Experiments reported [Forsyth et al., 2011] that the ATP release critically depends on the dynamical mode (TT or TB). Thus, it is sufficient to consider a 2D vesicle which is known to exhibit both TT and TB.

$\mathbf{X}(s)$ refers to the coordinate of the vesicle shape defined on a 2 dimensional space $\mathbf{x} = (x, y)$, with $s \in [0, P)$ the curvilinear coordinate (local arc length), where P is the perimeter of the vesicle. Ω_{in} refers to the vesicle internal domain with a constant area A, whereas Ω_{ex} designates the 'plasmic' domain. The reduced area is defined as $\tau = 4\pi A/P^2$ to quantify the deflation of the vesicle. $\tau = 1$ corresponds to a circle, while any other shape corresponds to $\tau < 1$. $R_0 = 3\mu m$ is a characteristic radius of the vesicle, which is defined by $\pi R_0^2 = A$. In the vesicle model, the Helfrich bending energy [Helfrich, 1973] is adopted in order to extract the membrane force:

$$\mathbf{H}(\mathbf{X}(s)) = \frac{\kappa}{2} \oint c^2 ds + \oint \zeta ds \tag{4.1}$$

κ is the bending rigidity modulus, c is the local curvature, s is the curvilinear coordinate, and ζ is a Lagrange multiplier which enforces local membrane inextensibility. The force per unit length along the membrane can be obtained thanks to a functional differentiation $\mathbf{f}(s) = \delta H \Big/ \delta \mathbf{X}(s)$.

The vesicle is immersed into an incompressible flow field $\mathbf{u}$, thus its shape evolution obeys

$$\frac{\partial \mathbf{X}}{\partial t} = \int \delta(\mathbf{x} - \mathbf{X})\mathbf{u}(\mathbf{x}) dx dy \tag{4.2}$$

The fluid velocity $\mathbf{u}$ is defined on domain $\mathbf{x} \in [0, L] \times [-W/2, W/2]$, (L is the domain length, W is the width). It satisfies the incompressible continuity condition

$\nabla \cdot \mathbf{u} = 0$, as well as the momentum conservation condition

$$\rho\left(\frac{\partial \mathbf{u}}{\partial t} + \mathbf{u}\cdot\nabla\mathbf{u}\right) = -\nabla p + \nabla\cdot(\mu\nabla\mathbf{u}) + \mathbf{F}(\mathbf{x}) \tag{4.3}$$

Here ρ is the fluid density, $\mathbf{F} = \oint \mathbf{f}(s)\cdot\delta(\mathbf{x}-\mathbf{X}(s))ds$ is the force that the vesicle applies on the fluid. μ is the dynamic viscosity, and takes two generally distinct values inside and outside the vesicle:

$$\mu(\mathbf{x}) = \begin{cases} \mu_{in} & if \quad \mathbf{x}\in\Omega_{in} \\ \mu_{ex} & if \quad \mathbf{x}\in\Omega_{ex} \end{cases} \tag{4.4}$$

The viscosity contrast is defined as the ratio between internal and external viscosity $\lambda = \mu_{in}/\mu_{ex}$.

The capillary number is defined as $Ca = \mu_{ex}\dot{\gamma}_w R_0^3/\kappa$, and represents the ratio between the applied shear force and the bending force. $\dot{\gamma}_w = \partial u_x/\partial y|_{y=-W/2}$ is the shear rate at $y=-W/2$. For a linear shear flow the shear rate is constant. However, this is not the case for a pipe flow and this is why we have to specify the definition of what is meant by the typical shear rate.

The chemical problem can be described without reference to any specific molecule, albeit later we will focus specifically on ATP. The concentration, defined on domain Ω_{ex} is denoted as $a(t,\mathbf{x})$, and it obeys, in general, the diffusion-advection-reaction equation. In its full generality, the concentration evolution equation takes the form

$$\frac{\partial a}{\partial t} + \mathbf{u}\cdot\nabla a = \nabla\cdot(D\nabla a) + R \tag{4.5}$$

where $D \simeq 2.36\times10^{-10}m^2/s$ is the ATP diffusion coefficient in plasma, with its value taken from [John and Barakat, 2001]. R is a reaction term. In what follows, we will set it to zero, since we will be exclusively interested in ATP release not involving reactions. The Peclet number is defined as $Pe = \dot{\gamma}_w R_0^2/D$, which ranges approximately from 1.0 to 200 in our simulations.

On the vesicle membrane, if $\mathbf{n}$ denotes the normal vector towards Ω_{ex}, the boundary condition of ATP release is set as

$$D\frac{\partial a}{\partial \mathbf{n}} = \psi(\mathbf{S}(s)) \tag{4.6}$$

This equation yields the total ATP flux across the membrane, which is a priori an unknown function of the precise membrane state at a given point of the membrane. $\psi(\mathbf{S}(s))$ is the ATP flux across the membrane, and it constitutes the main focus of the

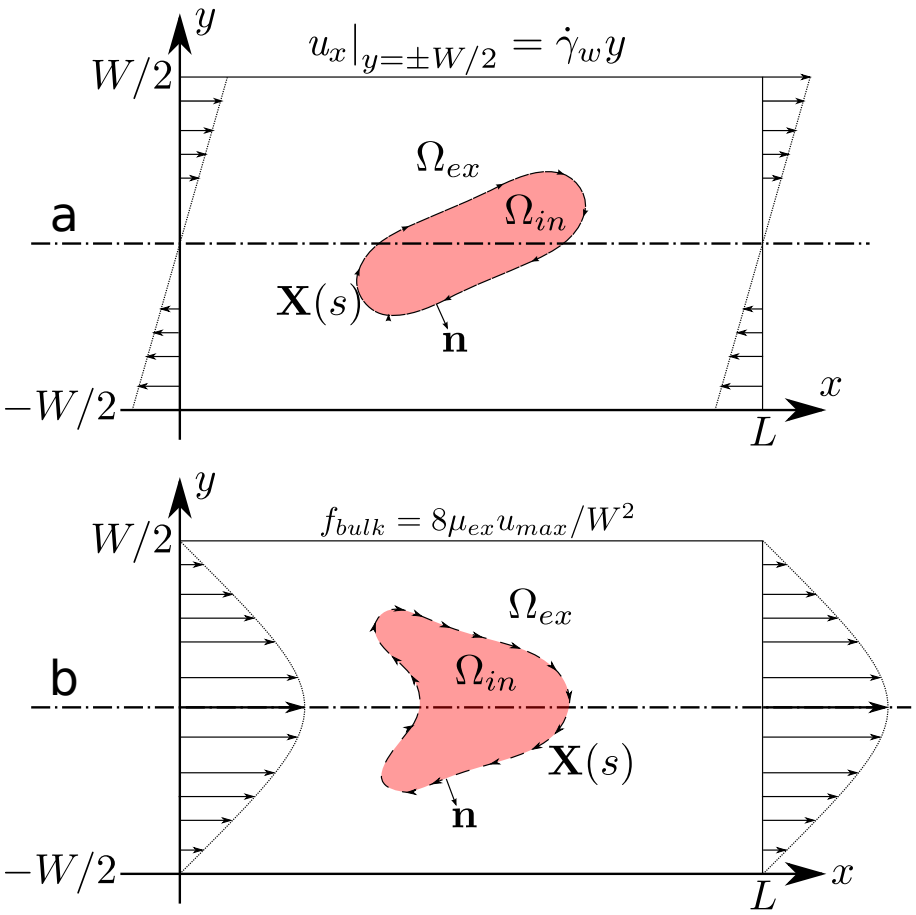

Figure 4.1: A schematic view of the studied configuration: (a) shows the case of a linear shear flow obtained by imposing the velocity of the upper and lower walls; (b) shows a similar configuration but for a Poiseuille flow, the imposed flow is generated by a bulk force term f_{bulk} which ensures a parabolic profile with maximum velocity u_{max}. In both configurations the ATP concentration a is defined on Ω_{ex}, and a Neumann boundary condition is imposed on the moving boundary $\mathbf{X}(s)$.

modeling. The vector $\mathbf{S}$ can be viewed as a collection of local states of the membrane. We will see later how $\psi(\mathbf{S}(s))$ can be inferred after a close inspection of experimental facts. Finally, and for simplicity, we impose that the concentration obeys periodic boundary conditions along x and has zero-flux across the bounding walls. Schematics of model configuration can be found in Fig. 4.1.

4.2.2 Lattice-Boltzmann Model for Fluid - Membrane - Solute Coupling

An Immersed-Boundary Lattice Boltzmann Method (IB-LBM) is implemented based on an identical numerical algorithm from [Shen et al., 2017b]. By choosing a pseudo Reynolds number of around 0.1, the method is well validated against the well established boundary integral method (BIM) in the Stokes limit (for BIM see [Thiébaud et al., 2014]). A similar lattice Boltzmann scheme is developed in chapter 3 to solve the advection-diffusion equation (equation (4.5) and (4.6)). This advection-diffusion solver has been validated against known analytical benchmarks as well as against the Galilean invariance tests for static and moving boundaries. The code was developed under Compute Unified Device Architecture (CUDA) in order to benefit from GPU acceleration, allowing for the fluid - membrane - solute coupling simulation within an acceptable computational time. The numerical methodology is introduced in chapter 3. The general numerical procedure for the boundary condition and the immersed boundary method can be found in [Krüger et al., 2017, Ladd and Verberg, 2001, Tsubota and Wada, 2010, Huang and Yong, 2015]. In this work, the calculation of membrane curvature and membrane shear stress is conducted via simple finite difference method, with first order precision. A more accurate shear stress calculation method based on LBM distribution functions proposed in [Krüger et al., 2009] could be employed in the future.

A similar study but with a static boundary has been proposed regarding the drug delivery problem [Gekle, 2017, Kaoui et al., 2018]. Problems related to diffusion-advection of a concentration field in a velocity field created by vesicles or capsules under flow have been treated recently [Kabacaoğlu et al., 2017, Kaoui et al., 2018]. In those studies, the vesicle/capsule membrane is fully transparent to the solute. That is, solute is advected passively by the flow. In the present study we will consider the problem of kinetics of ATP across the vesicle membrane. This requires implementation of an appropriate boundary condition on a curved and moving interface (i.e. a Neumann boundary condition for the ATP release).

4.3 ATP Release Modeling

The model of ATP release proposed has been inspired by *in vitro* experimental observations [Forsyth et al., 2011]. Since this is essential information to our problem, we have felt it worthwhile to briefly recall the main experimental results.

4.3.1 Shear Experiment

In the experimental study performed in [Forsyth et al., 2011], a RBC suspension was prepared at 1% hematocrit, implying negligible interaction among RBCs. Solutions were then mixed with dextran to create different viscosity contrasts λ by changing μ_{ex}, while $\mu_{in} = 0.012Pa \cdot s$. The explored viscosity contrasts were $\lambda = 1.6$, 3.8 and 11.1. The RBC solutions were sheared in a cone-and-plate viscometer (shear rate ranges from $50s^{-1}$ to $5000s^{-1}$) corresponding to different shear stresses mimicking physiological values in different blood vessels *in vivo*. After 30s exposure to the shear flow, the blood sample was mixed gently with bioluminescent luciferase/luciferin, so that a photomultiplier can count the photon emission, which is proportional to the averaged value of the extracellular ATP concentration. Each data point of the experiment is averaged over 5 independent measurements. The apparent shear stress (defined as the product of the imposed shear rate and the effective viscosity of the suspension provided by the rheometer) and cell motion (TT or TB) were also recorded statistically thanks to several performed experiments.

It was found that ATP release initiated at a critical shear stress $\sigma_c \leq 0.1Pa$ (the lower limit of apparent shear stress in Fig. 4.2), and then the release level remained constant (a plateau regime). When the shear stress exceeded a value of about $3Pa$, the ATP release started to increase monotonically. In the first interval of shear stress ($\sigma_c \leq 0.1 - 3Pa$) most of RBCs performed TB motion. In this configuration, the cell underwent a solid-like motion with minimal shape deformation. This means that in this shear stress interval, once a critical shear stress is attained the cell starts ATP release. Increasing the shear stress further does not increase the amount of ATP release. Beyond a shear stress of about $3Pa$, most of the cells performed TT motion in which cell shape deformation becomes significant. A further increase of shear stress implies higher shape deformation and higher ATP release. In this regime (TT) the ATP release is attributed to shape deformation, whereas in the former regime (TB) a critical shear stress is needed for ATP release. This means that two main pathways can be identified, one related to a critical shear stress, and the other is related to shape deformation.

Other investigations focused on the molecular origin of ATP release and support the idea that Px1 is the main avenue for shear-induced ATP release. This channel may also become activated due to a drop in oxygen content or in the presence of a high enough intracellular calcium concentration [Locovei et al., 2006]. It is assumed that this channel requires a critical shear stress for its activation. The increase of ATP release found in the TT regime is attributed to the CFTR. It is recognized that

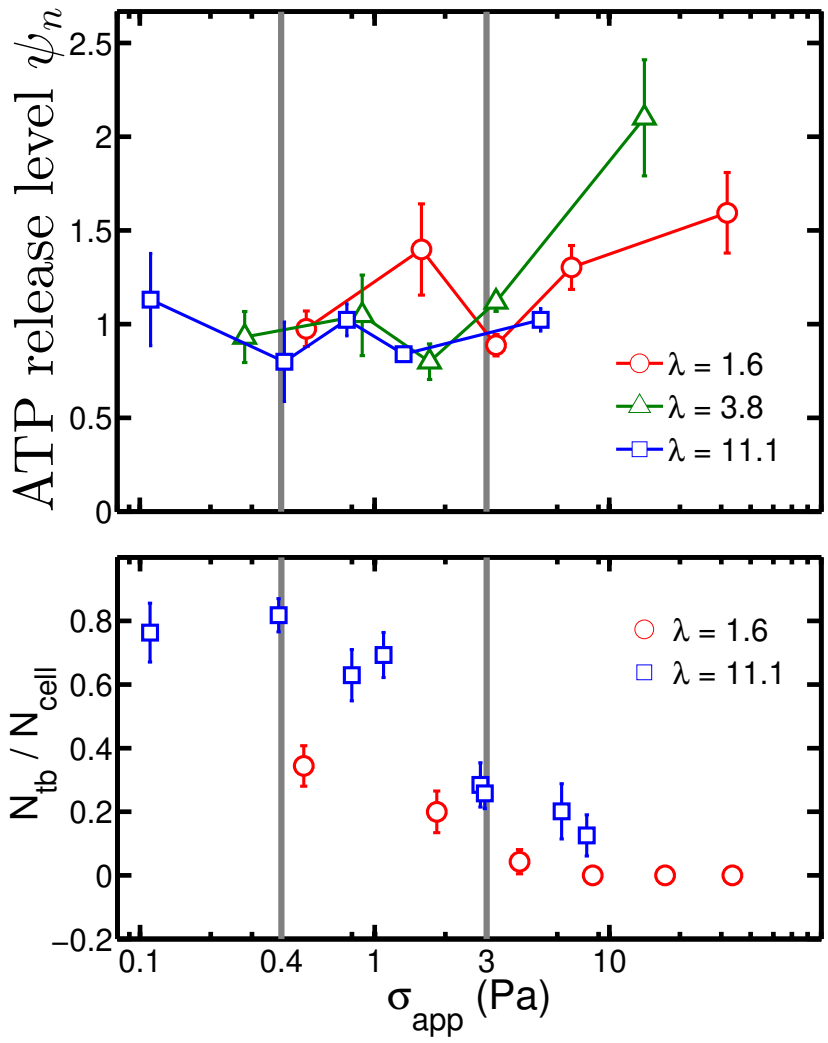

Figure 4.2: An adapted figure of ATP release level (upper) and tumbling / tank-treading motion data (lower) extracted from experimental study in [Forsyth et al., 2011]. The data are categorized into 3 different zones, below $0.4Pa$ is the range of shear thickening, in the middle range below $3Pa$ is the range of shear thinning, the last zone beyond $3Pa$ the shear thinning stops and a large portion of RBCs undergo tank-treading motion. A detailed definition of ψ_n is given in Equation 4.10.

CFTR itself may not directly release ATP, but rather it up-regulates Px1 so that a further increase of shear stress causes further deformation and thus amplifies the release. As described in the introduction, CFTR activation requires the presence of actin, the latter is more likely to be freed when cell deformation is high enough (that is in the TT regime).
Further support for the roles played by Px1 and CFTR are provided by data using specific inhibitors [Forsyth et al., 2011]. Carbenoxolone and glibenclamide are used to inhibit the Px1 channels and CFTR respectively. The study revealed that glibenclamide-treated RBCs no longer show increased ATP release with shear stress (TT regime). However, carbenoxolone-treated RBCs show a collapse of ATP release both in TT and TB regimes. In the TT regime, cell deformation is higher than in the TB one, but the collapse is similar in both regimes. This points to the fact that Px1 is a channel that is quite insensitive to cell deformation.

To summarize, the ATP release level is mainly affected by membrane shear stress $\sigma_{mem}(t, s)$ and by deformation: once the membrane shear stress reaches a critical value, the Px1 becomes activated, and no further release takes place upon further increasing the shear stress. Once in the TT regime, CFTR enters into play in order to up-regulate Px1, and since higher shear stress enhances cell deformation, an increasing up-regulation of Px1 is expected with shear stress.

4.3.2 ATP Release Model

We have seen above that two mechanisms are possible, one associated with the level of shear stress and the other with the level of membrane deformation. A schematic representation of this model can be found in Fig. 4.3. Let us focus on the latter first. For this scenario, once the shear stress exceeds a value (inducing RBC TT regime) the ATP release level is amplified monotonically to induce CFTR activation. Since RBCs have no organelle or nucleus, we consider that cell reaction takes place at the RBC membrane. We quantify the deformation level by the local curvature. Once in the TT regime, the cytoskeletal material point will explore with time different cell membrane local curvatures. Let $\dot{c}(s) = |Dc(s)/Dt|$ denote the time derivative of local curvature quantifying the level of an instantaneous variation of deformation at a given point, where D/Dt is the time derivative on a fixed point on Lagrangian curvilinear coordinate s.

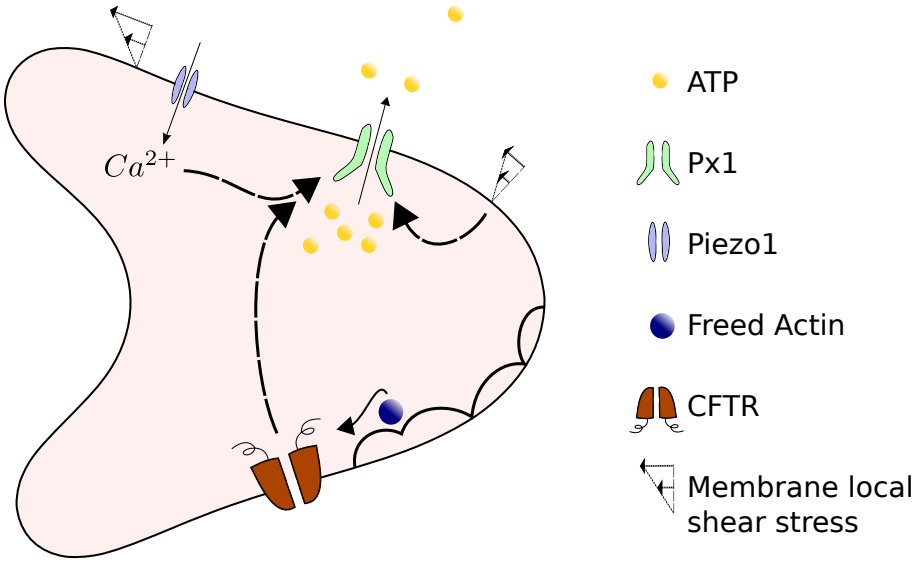

Figure 4.3: Schematics of the ATP release pathway in RBC: Px1 is the main avenue for ATP release that can be activated by the local shear stress and Ca^{2+} ions; the Piezo1 cation channel can be activated by the local shear stress and trigger Ca^{2+} influx; actin is freed from deformation induced cytoskeletial defects; CFTR is activated by freed actin and consequently up-regulates Px1.

The membrane local shear stress is given by $\sigma_{mem}(s) = \mu_{ex} \, |\partial u_{\mathbf{t}}(\mathbf{X}(s))/\partial \mathbf{n}|$, where $\mathbf{t}$ is the tangential vector. We can also define the apparent shear stress (for the sake of comparison with experiments) as $\sigma_{app} = \mu_{ex} \, |< \partial u_x/\partial y >|$, where the average is performed along the bounding wall in a shear experiment. The effective viscosity μ_{eff} of the suspension is given by $\sigma_{app}/\dot{\gamma}_w$, so that $\mu_{eff}\dot{\gamma}_w$ (used in experiments) coincides with the apparent stress.

ATP release rate due to Px1 channels is modeled as (Fig. 4.4 upper)

$$p_\sigma = k_\sigma \cdot H(\sigma_{mem} - \sigma_c) \tag{4.7}$$

where $H(x)$ is the Heaviside step function and k_σ is a phenomenological coefficient which will be extracted from confrontation with experimental data on ATP release. The above equation expresses the fact that the channel is activated above a critical shear stress σ_c on the membrane. This effect does not depend on deformation. The deformation affects CFTR, which in turns up-regulates Px1. The function expressing the fact that a curvature change will affect CFTR is written as (Fig. 4.4 lower panel)

$$p_{\dot{c}} = min(1 + k_{\dot{c}} \cdot (\dot{c} - \dot{c}_c) \cdot H(\dot{c} - \dot{c}_c), p_{\dot{c}max}) \tag{4.8}$$

Since CFTR affects the ATP release indirectly by up-regulating Px1, $p_{\dot{c}}$ is understood as an amplification factor. The value of $p_{\dot{c}}$ is limited between 1 (no release due to

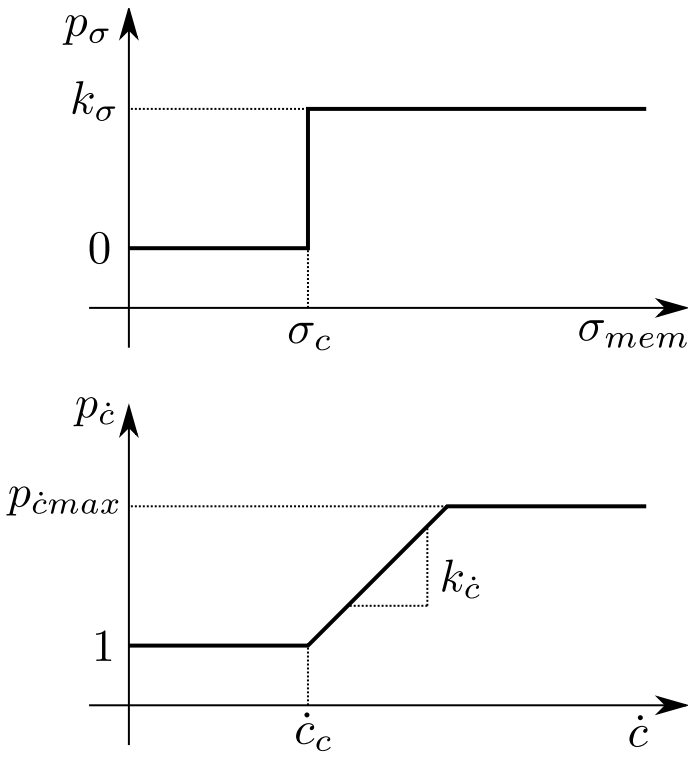

Figure 4.4: schematics of contribution from shear stress (upper) and curvature change (lower) to ATP release

deformation) and $p_{\dot{c}max} > 1$. The existence of an upper limit, expressed by $p_{\dot{c}max}$, is based on the notion that there should exist a maximum amount of free actin and a limited level of activatable CFTR. The phenomenological parameter $p_{\dot{c}max}$ will be determined by comparison with experiments.

All together, we write the ATP release flux equation (4.9) as a product between the two functions, namely

$$\psi = p_\sigma \cdot p_{\dot{c}} \tag{4.9}$$

The product means (i) if the shear stress is below a critical value there is no activation of Px1, and thus the flux vanishes, (ii) once the shear stress has exceeded a critical value, the Px1 pathway is activated, and even if no CFTR is present, ATP release takes place. If the curvature change is sufficiently large (beyond a critical value) CFTR is produced and amplifies the ATP release. We will see that these ingredients capture the essential experimental features.

We find it convenient to define a reference level of release, which we take to be the unity level, and is defined as the total release when all points on the membrane have reached a shear stress $\sigma_1 \geq \sigma_c$ and a curvature change $\dot{c}_1 \leq \dot{c}_c$. We set $\psi_1 =$

$\int_0^P \psi(\sigma_1, \dot{c}_1)ds = k_\sigma P$. Thus, a normalized ATP release level can be quantified by the ratio

$$\psi_n = \int_0^P \psi(\sigma, \dot{c})ds \Big/ \psi_1, \tag{4.10}$$

which is an important indicator for the origin of release. Indeed a value $\psi_n > 1$, means that the deformation of the cell contributes to ATP release.

For completeness, we would like to comment on some simplifying assumptions adopted here. In the upstream of the pathway (Fig. 4.3) the Piezo1 channel is activated by shear stress allowing calcium influx, which in turn indirectly activates Px1. This can be thought of as being absorbed into the value of k_σ as long as we are not interested in the details of calcium kinetics. In addition, the cytoskeletal defects leading to actin generation and CFTR activation are taken as simple and bounded linear functions of $\dot{c}$. The existence of a time delay for release mentioned in [Wan et al., 2008] is ignored. That is, we consider that all the reactions on the membrane take place on a much faster time scale than RBC deformation or shear stress change, despite the fact that they might have a comparable time scale when the blood flow is fast enough. Although the details of ATP renewal mechanism in RBCs are not well understood, bulk ATP generation occurs via a glycolysis process in the RBC cytoplasm, and under healthy conditions, blood sugar concentration has a quite stable value in plasma, around 5.0 mM. Thus, it is reasonable to assume that in the time interval of interest for ATP release, RBCs are saturated enough in ATP so that the release rate is not affected by the actual content of ATP.

4.3.3 Results: ATP Release Under Linear Shear Flow

4.3.3.1 Membrane Shear Stress and Deformation Behavior Under Flow

In order to test the model and to specify the range of parameters involved, we investigated the membrane shear stress and curvature change via numerical simulations. We refer to the experimental data in Fig. 4.2 (lower panel). It is found experimentally that the proportion of TB RBCs decreases as the apparent shear stress σ_{app} increases and the viscosity contrast λ decreases. The transition from TB to TT on increasing shear stress is attributed to the shear elasticity of the cytoskeleton, while the viscosity contrast dependent transition is due to hydrodynamic dissipation [Fischer et al., 1978b, Tsubota and Wada, 2010, Fischer and Korzeniewski, 2013]. Although the 2D vesicle model does not consider cytoskeleton, it can capture the viscosity contrast

induced transition, which is the main reason for TT motion at high σ_{app} regime. It will be seen below that if the ATP release is presented as a function of apparent shear stress itself, the behavior found in experiments and in simulations are very similar.

In the experiments, a dilute RBC suspension was considered (volume fraction of about 1%), so that the interaction among RBCs is negligible. It is thus sufficient to consider a single cell subject to a linear shear flow. We consider a channel width of $W = 12.5R_0$, and length $L = 25R_0$, resulting in a hematocrit 1.05% and a sufficiently weak confinement effect. We have explored the viscosity contrasts $\lambda = [1, 2, 4, 6, 8, 10]$. The reduced area is set to $\tau = 0.6$ or 0.7, but no significant difference between these two values was detected in the results. We explored a wide range of capillary numbers $Ca = [0.125, 1.0, 8.0]$. Since the typical time scale for RBC deformation is in the range of 0.01s [Prado et al., 2015] we have chosen our simulation time to be large enough as compared to that time. More precisely, the explored range goes from 0.5s to 10s under different shear rates (recall that in the experiments of Forsyth et al. [Forsyth et al., 2011] the shear stress was applied during 30s). During the full time interval of the simulation we observed enough loops of repeatable periodic release pattern. The ATP release rate is then averaged over the simulation time, after transients have decayed. The normalized mean curvature change (defined as $< \dot{c}R_0/\dot{\gamma}_w >$) is shown in Fig. 4.5. A decrease in normalized curvature change is observed upon increasing λ , which implies a higher activation level of CFTR in TT situations than in TB cases. The inflection of the curve between $\lambda = 4$ and $\lambda = 6$ for $Ca = 8$ is attributed to the fact that when the capillary number is high, even if the cell shows TB, the distortion of the shape starts to play a role at that capillary number. Note that the capillary number *in vivo* and in the experiments of Forsyth et al. [Forsyth et al., 2011] remains smaller or comparable to unity. We have deliberately explored even higher values here in order to highlight the robustness of the results. Note that the values of the mean membrane shear stress $< \sigma_{mem} >$ are very close to the apparent shear stress σ_{app} regardless of the values of the viscosity contrast λ and the capillary number Ca (see Fig. B.1 in the appendix). Therefore, no real distinction will be made between these two quantities when representing the results (actually the experiments in [Forsyth et al., 2011] referred to σ_{app}).

4.3.3.2 Analysis of The ATP Release from The Model and Confrontation with Experiments

A systematic investigation has been conducted on different parameter values in equation (4.7) and (4.8). By presenting the normalized ATP release ψ_n as a function of

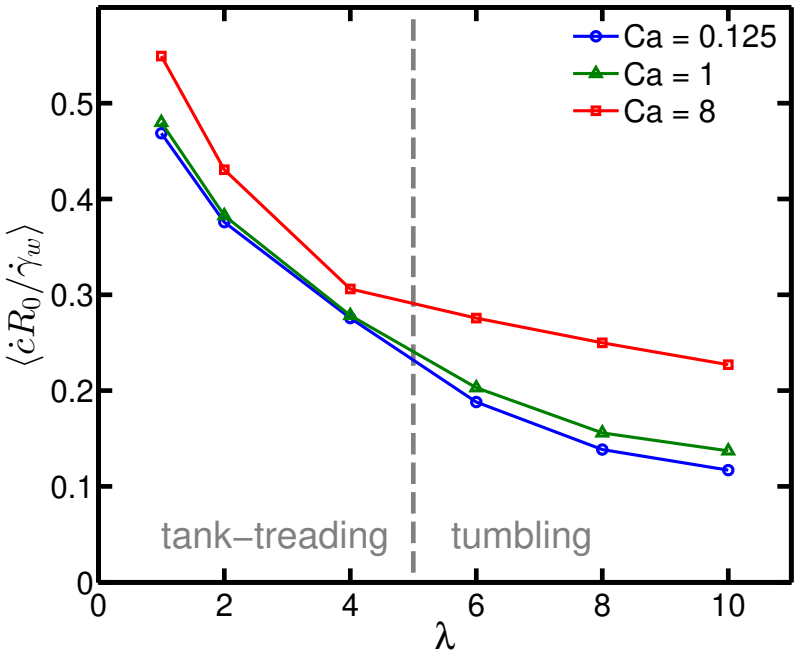

Figure 4.5: curvature change vs viscosity contrast

Table 4.1: Parameters for ATP release model

Notation	value	Origin
$\dot{c}_c$	$2 \times 10^2 \mu m^{-1} s^{-1}$	estimated
$k_{\dot{c}}$	$6 \times 10^{-3} \mu m s$	estimated
$p_{\dot{c}max}$	2.5	estimated
σ_c	$0.05 Pa$	estimated
k_σ	$\sim 7 \times 10^3 (nmol/L) \cdot \mu m/s$	estimated

σ_{app}, we could compare the model behavior with the experimental data in Fig.4.2 (upper panel). This investigation revealed that the proposed ATP release model provides qualitatively similar results to the experiments: (i) the value of σ_c is critical to the shape of plateau; (ii) $\dot{c}_c$ is sensitive to the position of inflection point (at $3Pa$ in the experiments); $k_{\dot{c}}$ and $p_{\dot{c}max}$ corresponds to the slope and maximum value of ψ_n.

Although the ATP release criterion is linear, hidden nonlinearities are present due to the nonlinear shape dynamics of RBC. Thus, the fitting procedure is not an easy task. We have adopted a trial and error procedure in order to determine the parameter set in Table 4.1, which provides the most quantitatively comparable results to those reported by experiments (compare Fig. 4.6 and Fig. 4.2 (upper panel)). Note that since in Fig. 4.6 we only consider the normalized ATP release level, the value of k_σ is not needed at this level.

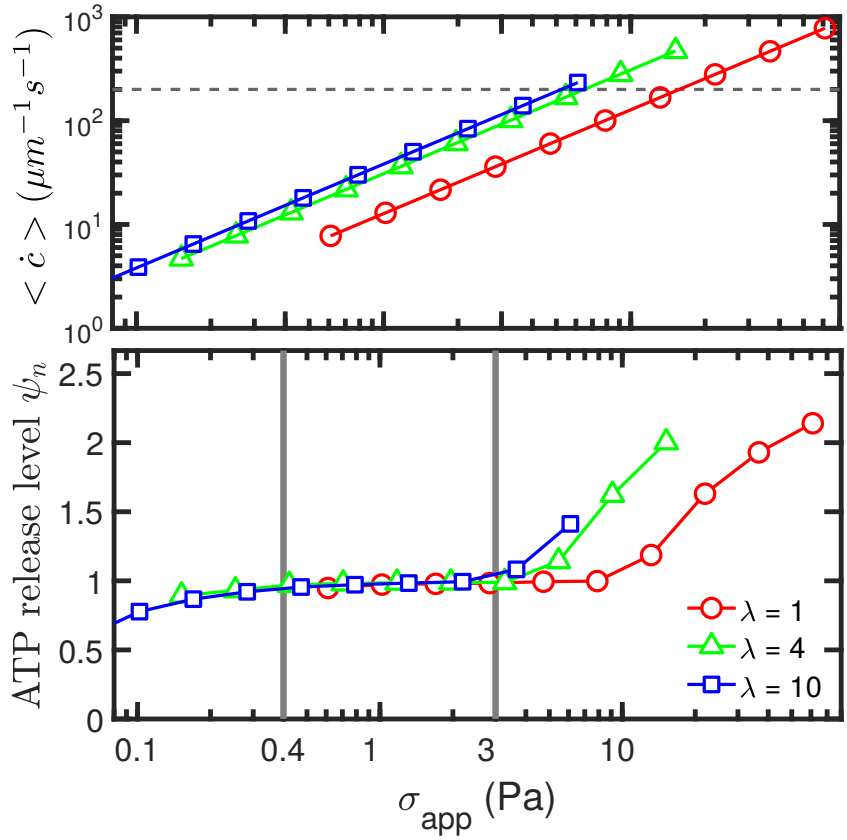

Figure 4.6: Mean curvature change (upper panel) and ATP release level (lower panel) vs apparent shear stress, with reduced area $\tau = 0.7$ and capillary number $Ca = 1$. The dash-line in upper panel corresponds to the critical curvature change $\dot{c}_c$ beyond which ATP release due to deformation takes place.

Smaller capillary numbers such as $Ca = 0.125$ and reduced area 0.6 or 0.7 provide almost identical results, as in Fig. 4.6. At larger values of Ca ($Ca = 8$) a deviation is observed (as testified by the behavior of the deformation amplitude in Fig. 4.5), especially at large enough λ. This is due to the fact that the membrane starts to develop buckling, even though the vesicle is tumbling. This enhances the effect of shape deformation and thus CFTR activation. For RBCs buckling is quite rare, this is why we do not pay a particular attention to this problem here.

Our results (Fig. 4.6) capture the plateau below $3Pa$ seen in the experiments (Fig. 4.2 upper), which is associated mainly with the TB regime, as well as the increase of ATP release with shear stress associated mainly with the TT regime. This has allowed us to fix the model parameters. In addition, our results reproduce well the amplitude of variation of ATP release, from the small shear stress to the highest one.

Actually, at small enough apparent shear stress in Fig. 4.6 (below $\sim 0.3Pa$) the ATP release shows a small drop, while our model (Equation 4.7) would have suggested that the ATP release, once it takes place, would follow the plateau level. In fact, our criterion is local (it senses the local stress) while Fig. 4.6 refers to an average stress. The local threshold can thus be significantly lower than the average one. In other words, for small apparent shear stress, it is possible that only few localized points on the membrane can release ATP (see Fig. 4.7).

Hitherto we have only described the normalized value of ATP release and not the absolute level of this release. In order to estimate the absolute value, we need to evaluate k_σ. Confrontation of our model with experiments [Forsyth et al., 2011] suggest the value given in Table 4.1. This is estimated by considering the RBC volume, surface area and average ATP concentration in plasma ($a_0 \approx 1000nmol/L$, see [Gorman et al., 2007]). The precise way for determining k_σ is explained in the appendix B.

Note that the actual value of the critical shear stress σ_c still suffers from some uncertainties. Combining the outcomes from experiments in a linear shear flow [Forsyth et al., 2011] and in a Poiseuille flow experiment from [Wan et al., 2008] suggests that this value lies in the range $0.02 - 0.1Pa$. Further systematic experiments will be needed in order to acquire more statistics with the hope of better refining our estimates.

Finally, our model shows that in some shear rate range ($\dot{\gamma}_w > 2000Hz$ in this study), an increase in internal viscosity, μ_{in}, triggers a decline in ATP release level. This is attributed to the fact that a hardened cell (due to an increase of internal viscosity) implies a smaller level of membrane deformation and thus a decline in ATP

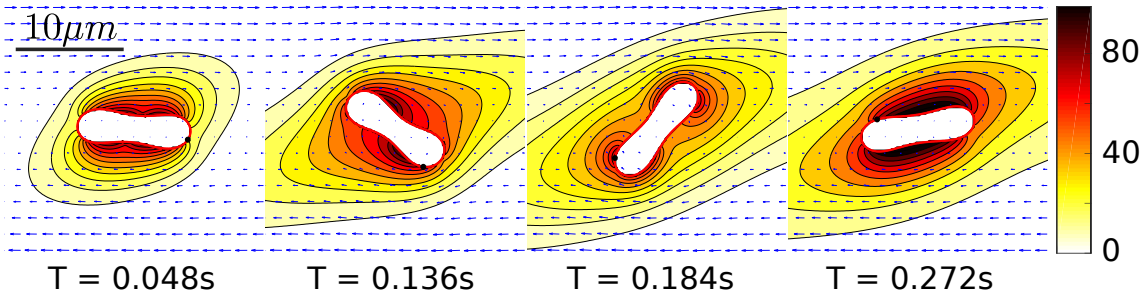

Figure 4.7: A snapshot showing the inhomogeneous ATP release along the membrane, with $\tau = 0.6$, $\lambda = 8$, $Ca = 1$, $\dot{\gamma}_w = 50s^{-1}$ and Peclet number 1.91. In this situation, the magnitude of $\sigma_{mem} \approx \dot{\gamma}_w \cdot \eta_{ex} = 0.075Pa$ is close enough to $\sigma_c = 0.05Pa$, which leads to strong inhomogeneity of ATP flux along the membrane (not each membrane point reaches its threshold value at a given time). The contour map from white to red represents a relative local concentration, while the blue arrows represent the velocity field, the black dot on the membrane is a virtual tracer particle. The unit for color bar is $nmol/L$, but note that the concentration gradient in the normal direction along the membrane is more relevant, as it is proportional to the ATP release rate.

release. This suggests that pathologies leading to an increase in RBC rigidity may be associated with an impairment in ATP release (see Fig. B.2).

4.4 ATP Release in Confined Poiseuille Flow

In order to study how the ATP release happens in microcirculation, we start from long straight channels that mimic the pre-capillary ateriole. Vesicles as well as RBCs under Poiseuille flow have shown various shapes and dynamics [Kaoui et al., 2011, Aouane et al., 2014b, Fedosov et al., 2014, Quint et al., 2017]. Typical examples are parachute and slipper shapes. The observed shapes and dynamics depend, in particular, on flow conditions (capillary number, confinement, etc...). Since our study focuses here on a 2D vesicle, we shall refer to the phase diagram of shapes obtained in [Kaoui et al., 2011], where besides the parachute and slipper shapes, a snaking motion is also revealed. We consider here also a single vesicle. In capillaries the hematocrit is quite low (it can drop down to 5% [Sutera et al., 1970, Popel and Johnson, 2005]), so that focusing on a single cell constitutes a reasonable assumption. The imposed flow is of Poiseuille type. We define the degree of confinement as $Cn = 2R_0/W$. We recall the general definition of the capillary number $Ca = \mu_{ex}\dot{\gamma}_w R_0^3/\kappa$. The wall shear stress in a Poiseuille flow is given by $\dot{\gamma}_w = 4u_{max}/W$, where u_{max} is the maximum velocity at the channel center-line. Assuming that a RBC has a characteristic radius around

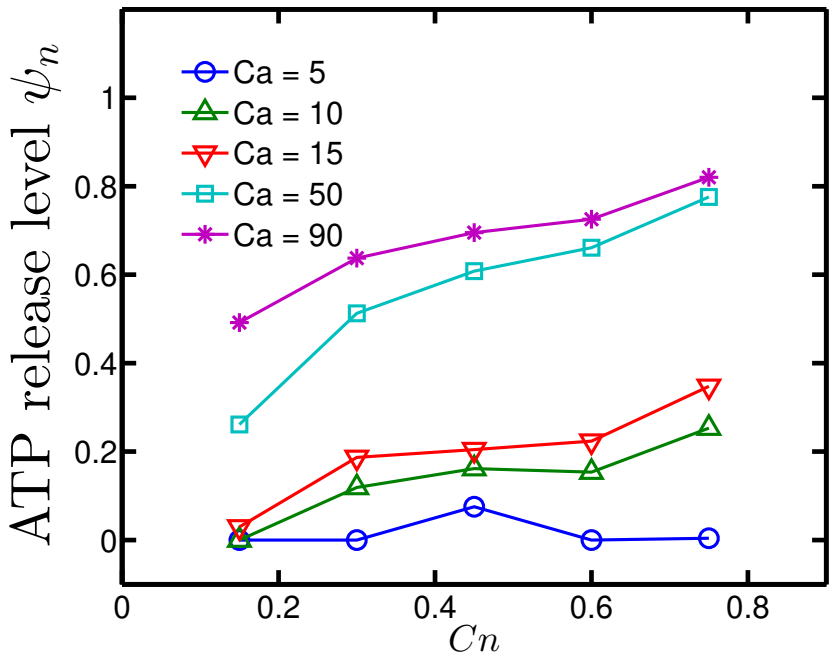

Figure 4.8: ATP release levels for Poiseuille flow in long straight channels.

$R_0 = 3\mu m$ and bending modulus $\kappa = 3\times10^{-19}J$, we can map the non-dimensional pair (Ca, Cn) onto physical units (u_{max}, W), if need be. We have the following relations:

$$\begin{aligned} u_{max} &= \frac{\kappa}{2\mu R_0^2}\frac{Ca}{Cn} \\ W &= \frac{2R_0}{Cn} \end{aligned} \tag{4.11}$$

We explored $Ca = [5, 10, 15, 50, 90]$ and $Cn = [0.15, 0.3, 0.45, 0.6, 0.75]$, the length of the periodic simulation box is fixed at $L = 53.3R_0$, which is validated to be long enough to eliminate artifacts due to periodic boundary conditions. The resulting ATP release levels are shown in Fig. 4.8.

It is quite intuitive that the shear stress generally increases with both the confinement and the capillary number. For $Ca > 15$ the ATP release level increases monotonically by reducing the channel width for a fixed pressure drop. The subtle peak at $Ca < 10$ and $Cn \approx 0.45$ in Fig. 4.8 is due to the slipper - parachute - slipper/snaking transition [Kaoui et al., 2011]. Indeed, the parachute shape, which occurs for $Cn = 0.45$, has a larger cross section in the channel than the snake-like shape (Fig. 4.9 upper). This larger cross section implies a higher membrane shear stress σ_{mem} at two endpoints of the parachute (Fig. 4.9 lower)

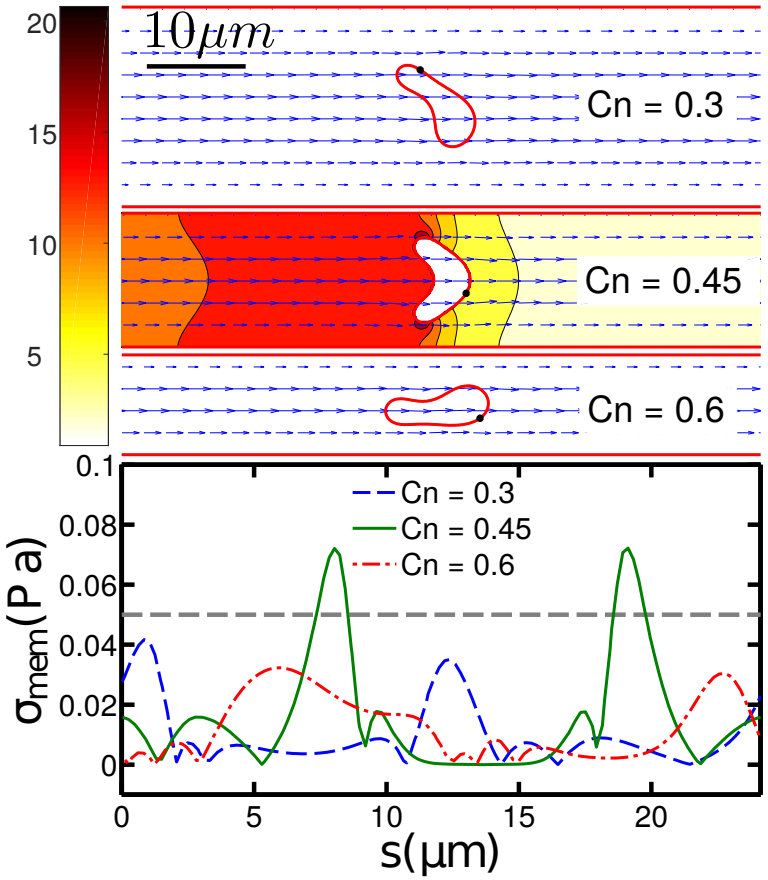

Figure 4.9: Plasmic ATP concentration (upper) and membrane shear stress distribution (lower) for $Ca = 5$ and $Cn = [0.3, 0.45, 0.6]$, Corresponding Peclet numbers are $Pe = [23.5, 10.5, 5.9]$ respectively. The colorbar has a unit $nmol/L$. Note that ATP release rate is proportional to the concentration gradient in the normal direction to the membrane. When $Cn = 0.45$, RBC assumes a parachute shape and has a non-zero ATP release at two lateral endpoints. The horizontal dashed line in (lower) indicates the critical membrane shear stress $\sigma_c = 0.05Pa$

An important remark is in order. The curvature change (shape deformation) level of this single vesicle in the long straight channel never reaches the activation threshold of CFTR (the largest $\dot{c}$ is still one order of magnitude smaller than $\dot{c}_c$, see Fig. B.3). This means that the ATP release effect due to deformation is weak in such a geometry, at least for a single cell. It must be kept in mind, however, that *in vivo* RBCs often meet bifurcations in the microcirculation where they experience large shape deformation. This naturally leads us to discuss the effect of bifurcations.

4.5 ATP Release at and after A Bifurcation

The microcirculation involves a complex vessel network. RBCs flowing in arteries enter arterioles and then capillaries. During their travel in the microcirculation, they experience a cascade of branching vessels. Many numerical studies have been performed in single or multiple bifurcations regarding more or less complex models of blood flow [Audet and Olbricht, 1987, Barber et al., 2008, Doyeux et al., 2011, Hyakutake and Nagai, 2015, Pries et al., 1990, Balogh and Bagchi, 2017]. The arterioles are wrapped by smooth muscle cells and are well innervated, so in principle they are capable of controlling their pressure via vasomotion. The capillary vessels are not endowed with smooth muscle cells, so that their pressure gradient can only be passively affected thanks to arterioles located upstream. The presence of ATP as a signaling molecule may offer another alternative. If a sufficient amount of ATP is released from RBCs at downstream capillaries (due to their ample deformations), a reaction with purinergic receptors (a class of membrane receptors that mediates vascular reactivity etc.) [Dubyak and el Moatassim, 1993, BURNSTOCK, 1999] on the surface of endothelial cells will lead to an intercellular calcium / eNOS signal. This signal can be transmitted to neighboring endothelial cells (in the form of waves) until reaching arterioles, ultimately giving rise to vasodilation in arterioles.

In pre-capillary and capillary networks the topological complexity can significantly contribute to the ATP release. Indeed a RBC frequently encounters bifurcations. At this point the cell is strongly deformed (see Fig. 4.10) when entering a new vessel and scrapes initially along the vessel wall, while progressively moving away from the vessel wall due to a well documented wall-induced lift force [Olla, 1997, Cantat and Misbah, 1999, Seifert, 1999, Vlahovska and Gracia, 2007, Vlahovska et al., 2009, Farutin and Misbah, 2013]. Before the RBC hits a new bifurcation, it travels a length of about $100\mu m$ in capillaries. This scenario is reproduced in our simulation (Fig. 4.10). Close to the wall, the cell has a larger membrane shear stress and higher deformation rate

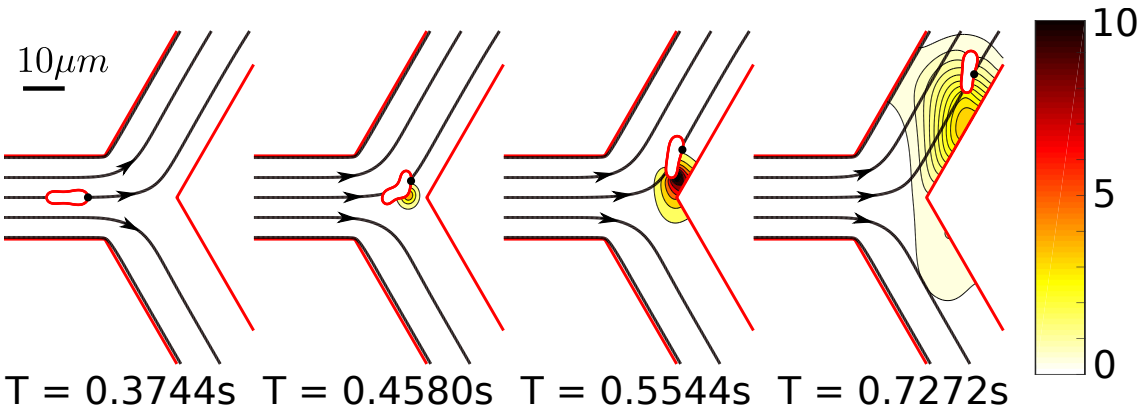

Figure 4.10: Snapshots of bifurcation scenario with inlet $(Ca, Cn) = (5, 0.3)$ and $Pe = 1.06$. The ATP release starts when the cell approaches bifurcation vertex, and ends when it migrates close enough to the center-line. The color bar has a unit $nmol/L$. Note that the ATP release rate is proportional to the concentration gradient in the normal direction to the membrane. Streamlines are shown with black arrows. One may notice that the RBC motion is highly correlated with its local streamline. At $T = 0.4680s$ one may see that the RBC is largely deformed before hitting the vertex since the direction of the streamline already towards the daughter branch.

as compared to the centered cell in a channel. This means that after each branching, a higher ATP release will occur in RBCs. We measured the distance needed for a RBC to return to the daughter branch channel center and thus to the (low) level of release we obtained above for a straight channel. We find that this distance is typically comparable to or longer than the characteristic vessel branching length in the microcirculation. This implies that RBCs are likely to strongly enhance their ATP release in the microvasculature thanks to the cascade of bifurcations.

We have selected a demonstrative case to show the ATP release of a cell hitting a bifurcation. The geometry is composed of one straight vessel with $(Ca, Cn) = (5, 0.3)$ as the inlet and two outlet vessels with $(Ca, Cn) = (3.0, 0.3)$ and $(Ca, Cn) = (2.0, 0.3)$. Their capillary numbers are preset to different values, rather than identical, in order to avoid perfect unrealistic symmetries that artificially lead to a high residence time at the bifurcation vertex, before the cell selects one of the two daughter vessels. The cell is initially positioned at the center-line of the inlet with a relaxed biconcave shape. Fig. 4.10 shows snapshots of the cell position before, at, and after the bifurcation. Fig. 4.11 shows the lateral position and normalized ATP release situation during this process.

Once the cell hits the bifurcation, it deforms significantly close to the wall and

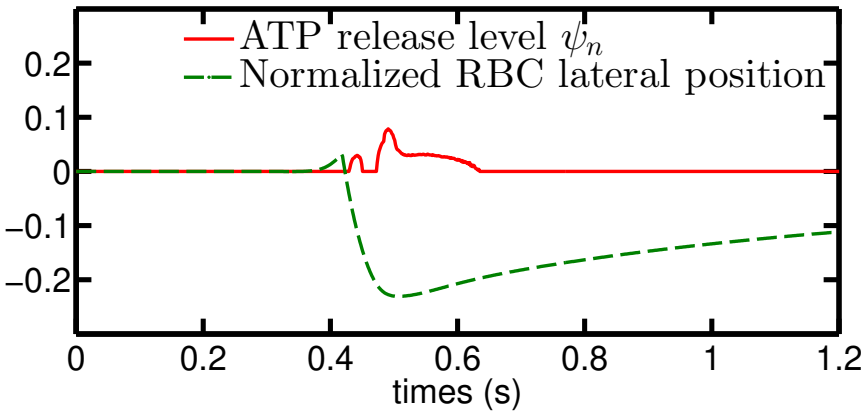

Figure 4.11: A bifurcation configuration composed of inlet and outlet with parameters that do not release ATP shows a slight non-zero release level when the RBC "hits" the bifurcation point. The lateral off-center position correlates strongly with the release level. This implies that the edge-to-center migration affects the ATP release process. The lateral position is defined as the ratio between vessel diameter and the minimal distance of the centroid of RBC to the closest point on center-lines of all vessels, valued from -0.5 to 0.5

begins to lift-off until it reaches the center-line. We have analyzed the ATP release during lift-off. The lateral migration after a bifurcation is a robust feature. We have also investigated the effects of different bifurcation angles, initial positions and capillary number; see Fig. B.5 in appendix B. It is found that the overall features reported above are not significantly affected.. We have found that it is sufficient to consider the case of a straight channel with the cell located initially in the vicinity of the wall. Because the time scale for shape response to stress is fast (as compared to the migration time), this is practically equivalent to following the cell from a bifurcation. We explored again the ranges $Ca = [5, 10, 15, 50, 90]$ and $Cn = [0.15, 0.3, 0.45, 0.6, 0.7]$. It can be seen in Fig. 4.12 that during a typical lift-off (where the ATP release reaches about its basal level in a long straight channel) the cell would have travelled about $100 - 1000\ \mu m$, which is comparable to the typical microvessel length of pre-capillary and capillary networks. The observed nonlinearity at $Ca = 5$ and $Cn = 0.6$ is mainly due to the transition between parachute-to-slipper or snaking, evoked before. We clearly see that the ATP release level is dramatically different from that obtained for long straight channels when the confinement Cn is smaller than about 0.5, which corresponds to $12\mu m$. This is a typical value for arterioles connecting capillaries. When $Cn > 0.5$, the normalized ATP release is, however, not affected much by this lateral migration.

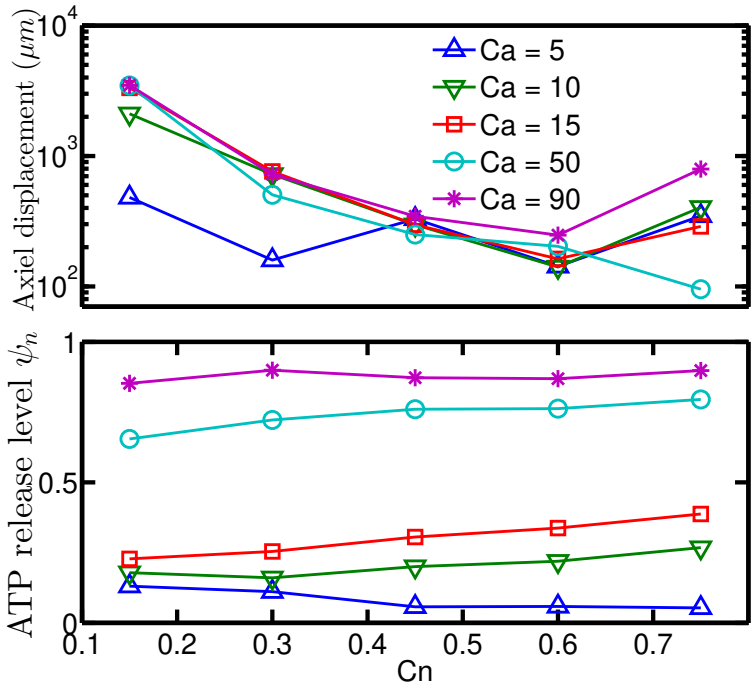

Figure 4.12: RBC axial displacement (upper) and normalized ATP release level (lower). The measurement is during the process of a RBC migration from the wall to the center, ending up with a steady shape and ATP release level. Comparing (the present lower panel) to Fig. 4.8 shows that for low confinement the lifting process causes more ATP release than when the cell is in a steady centered shape.

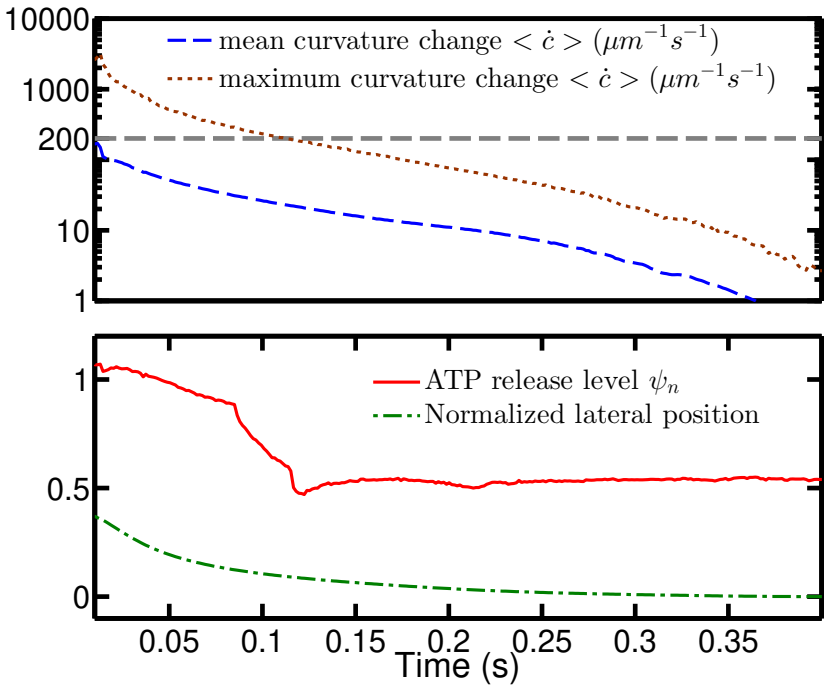

Figure 4.13: The upper figure shows the history of mean and maximum curvature change during the lateral migration process at $(Ca, Cn) = (50, 0.3)$. The horizontal gray dashed line corresponds to the value of the critical curvature change $\dot{c}_c = 200\mu m^{-1}s^{-1}$; The lower figure shows ATP release level and normalized lateral position history at $(Ca, Cn) = (50, 0.3)$

We also confirmed that the release is amplified by large curvature change when $Ca \geq 50$ (Fig. 4.13). When a RBC is close to the wall, the membrane shear stress can be estimated as $\sigma_{mem} \sim \sigma_{wall} = \dot{\gamma}_{wall}\mu_{ex} = \kappa/R_0^3 Ca$. This value is around $0.5Pa$, significantly below the value beyond which the deformation component of the ATP release takes place for the linear shear experiments (which is about 3 Pa; see Fig. 4.6). A possible explanation is that the capillary number is high and that the presence of the wall induces strong distortion of the vesicle making the local deformation high as compared to the linear shear flow, despite the fact that the apparent shear stresses are similar in both cases.

To exemplify the effect of shape deformation close to the wall, Fig. 4.13 gives an example at $(Ca, Cn) = (50, 0.3)$ where one finds that the deformation does affect ATP release level when the RBC is close enough to the wall. It also means that if a vessel network has a shorter characteristic length than usual, it may result in more ATP release per RBC.

4.6 Discussion and Conclusions

In this chapter, we have proposed a model for ATP release from RBCs and have explored it numerically. We have addressed the question of how geometry and stress amplitude in pre-capillary networks affect the ATP release from RBCs. With the help of experimental data, numerical simulations and assumptions on molecular mechanisms, we were able to fix the model and its parameter values that generate results that semi-quantitatively match existing *in vitro* shear experiments. In this model, the mechanical properties are mainly represented by membrane shear stress and curvature change (as an indicator of deformation level). At the molecular level, the Px1 hemichannel is considered as a main player of ATP release thanks to its sensitivity to shear stress level. When the cell deforms significantly, another mechanism becomes possible, in which free actin is detached (due to high deformation) from cytoskeletal defects which in turn activate the CFTR protein. The latter then up-regulates Px1 to promote ATP release. Interestingly enough, despite the oversimplification of the model, using only a Heaviside step function (for shear stress sensing) and a bounded linear function (for deformation sensing), the model remarkably captures the essential pattern of ATP release reported in *in vitro* shear experiments.

A lattice-Boltzmann based numerical solver coupling vesicle dynamics, and solute advection-diffusion with arbitrary moving boundary conditions has been developed. This solver is straightforwardly applicable to more detailed models in the future, including multicellular systems in complex geometry.

An estimate of the distance needed for a RBC after hitting a bifurcation before it returns back to its ATP release level of a steady shape in a long straight channel has been investigated. We found that this distance is hundreds of microns for confinements smaller than 0.3 ($20\mu m$ in diameter) and thousands of microns for a confinement of 0.15 ($40\mu m$ in diameter). This value is comparable or larger than the typical length of a blood vessel branch in pre-capillary arterioles or large capillaries, which implies that bifurcations boost the mechanically dependent ATP release in the microvasculature.

Chapter 5

The Spatial-Temporal Modeling and Simulation of Flow-induced Signaling Process in Microcirculation

In this chapter, we preliminarily discuss the implications of RBCs dynamics in mechano-based local regulation events in microcirculation. In particular, we focus on the interplay between ATP released from deformed RBCs and shear-sensing of the blood vessel occurring at the endothelial monolayer. A numerical approach is employed, in which, the advection-diffusion-reaction of ATP as a vasodilator is fully resolved based on the fluid-membrane-solute model we built in chapter 3 and the RBC releasing ATP model in chapter 4, the endothelial calcium signaling based on a model adopted from [Plank et al., 2006]. The current state of this chapter is mainly demonstrative, and serves as a basis for further investigations.

5.1 Introduction

The metabolic level of a particular tissue can vary dramatically in different circumstances. Changes of metabolism are often accompanied by changes in blood flow rate. For example, skeletal muscles are perfused with more blood during physical exercises [Segal, 2005], similar events are also observed in human cortex [Hoge et al., 1999]. This correlation between metabolic level and blood flow is intrinsically attributed to variations of tissues' oxygen consumption level, implying that the blood flow is not merely passive fluid. Instead, blood flow is routinely regulated by mechanisms with active natures, evidences can be found in a large number of experimental studies [Judy et al., 1976, Roy and Sherrington, 1890, Rees et al., 1989, Segal, 2005, Duncker and Bache, 2008]. Active regulations of blood flow can be either global or local. The en-

docrine hormones typically cause global impact. For example, adrenaline (a hormone released from adrenal gland) may raise up the heart rate as well as the blood pressure, causing an increase of perfusion rate in all vessels. However, different tissues are not always sharing the same metabolic level. This fact motivated studies on understanding local regulation mechanisms of blood flow. The prevalence of several local regulation mechanisms [Segal, 2005] have been confirmed and, interestingly, these are not always associated with oxygen consumption level. In addition to mechanisms based on metabolic level (as well as oxygen consumption level), there are other mechanisms such as spreading of hypoxia due to local diffusion, diffusion of vasodilater and coupled activation of distant sympathetic nerve ends [Segal, 2005].

A prominent example of local regulation follows. This is the so-called myogenic mechanism, which is able to maintain the blood pressure in capillaries despite pressure changes in the parent arteriole, thanks to the pressure sensitive ion channels and intercellular calcium signaling on smooth muscles and endothelial cells [Hill et al., 2001].

Besides hemodynamical pressure, the smooth muscle are sensitive to changes in the luminal shear stress [Koller and Kaley, 1990]. In contrast to vasoconstriction triggered by pressure increase in the myogenic mechanism, the increase of shear stress in arterioles and capillaries results in a vasodilation. This pathway is believed to be closely involved with endothelial cells' ability to sense flow shear stress, in which, endothelial cells encode flow shear stress and vasodilator concentration on the lumen surface into a change in intracellular free calcium ion concentration, which may eventually trigger endothelial nitric oxide synthase (eNOS) pathway in the smooth muscle, causing vasodilation.

Endothelial cells are one of the key players of these hemodynamical forces-dependent local regulation. They form a thin monolayer that covers all inner side of blood vessel. Their capability of responding to blood shear stress and vasodilators (e.g. acetylcholine, phosphate compounds such as ATP and ADP [John and Barakat, 2001]) is believed to be the first step for force-dependent local regulation in microcirculation. Though the origins of this shear sensing ability is not fully understood, experimental and theoretical studies have proposed several molecular candidates, such as mechano-sensitive ion channels (such as $TRPV_4$ [Hartmannsgruber et al., 2007], P_2X_4 [Yamamoto et al., 2000]), G-protein coupled receptors, glycocalyx, integrins and actin filaments, etc. [Yamamoto and Ando, 2011].

Recently, *in vitro* experiments revealed that RBCs under flow may release ATP due to deformation and shear stress [Forsyth et al., 2011, Wan et al., 2008] (also see

chapter 4). In [Sprague et al., 1996], the author present indirect evidences which support the fact that the deformation induced ATP release from RBCs in isolated rabbit lungs increased the production of nitric oxide (an important vasodilator in smooth muscle), thus, involved in local regulation. Inspired by these experimental facts, we hypothesize that the presence of RBCs in microcirculation (in arterioles and capillary networks) may contribute to shear stress-dependent regulations in two ways: i) they perturbe wall shear stress on endothelial surface ii) they release ATP as a vasodilator.

In this chapter, we present a preliminary simulation study on the hypothesized shear stress-dependent local regulation mechanism, focusing on the spatial pattern of ATP concentration and shear stress distribution. A demonstrative branching network is employed to mimic the vessel network geometry. We consider effects from RBC deformation, vasodilator (ATP [Crecelius et al., 2011]) dispersion, wall shear stress and their roles in the endothelial calcium dynamics. This preliminary work may provide some intuitions on this hypothesis and inspirations to forthcoming systematic studies.

5.2 The Modeling of Endothelial Calcium Signaling and Its Coupling to RBC Dynamics in A Demonstrative Vessel Network

5.2.1 Modeling of ATP dynamics

A scheme on the modeling of endothelial calcium signaling and the ATP dispersion in lumen is presented in Fig. 5.1. Consider the lumen region is denoted by Ω, with its normal vector $\hat{n}$ pointing outward (Fig. 5.2). The lumenal ATP concentration a is governed by an advection-duffusion equation

$$\frac{\partial a}{\partial t} + \mathbf{u} \cdot \nabla a = D_a \nabla^2 a \tag{5.1}$$

Here $\mathbf{u}$ is the velocity field, obeying Eqn. (4.3).

We took the vessel network geometry from [Balogh and Bagchi, 2017] and which was extracted from a cat mesentery, where there are three levels of vessel bifurcations in series from arteriole to capillaries, followed by capillaries' convergences to a venule. For blood flow, a periodic boundary condition is imposed in the stream direction in the arteriole and the venule, a fixed pressure drop creates a flow with an average speed around $0.03 cm/s$ in the finest level of capillary (see Fig. 5.2). Under these

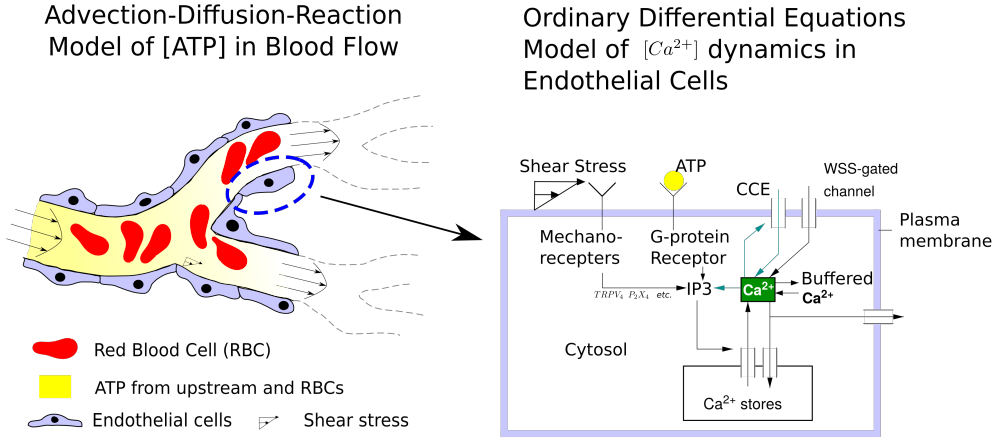

Figure 5.1: A schematic for calcium signaling and ATP dispersion in a micro-vessel network. Free calcium ion concentration and ATP concentration are represented by $[Ca^{2+}]$ and $[ATP]$ respectively. Left panel: Dispersion of ATP and its corresponding flow / RBC dynamics in lumen is fully resolved by a fluid-membrane-solute model, ATP is released from RBC and endothelial wall (lumenal) due to shear stress. Right panel: A lumped element model of calcium signaling in a endothelial cell, adopted from [Plank et al., 2006], considering shear stress and ATP concentration from lumen side, IP_3 dynamics, internal calcium store (Endoplasmic Reticulum) and fuffer proteins (e.g. calmodulin). The schematic plot in right panel is taken from [Plank et al., 2006] and then modified by adding the mechano-receptor coupled cation channel $TRPV_4$ and P_2X_Y [Yamamoto and Ando, 2011, Li et al., 2015]

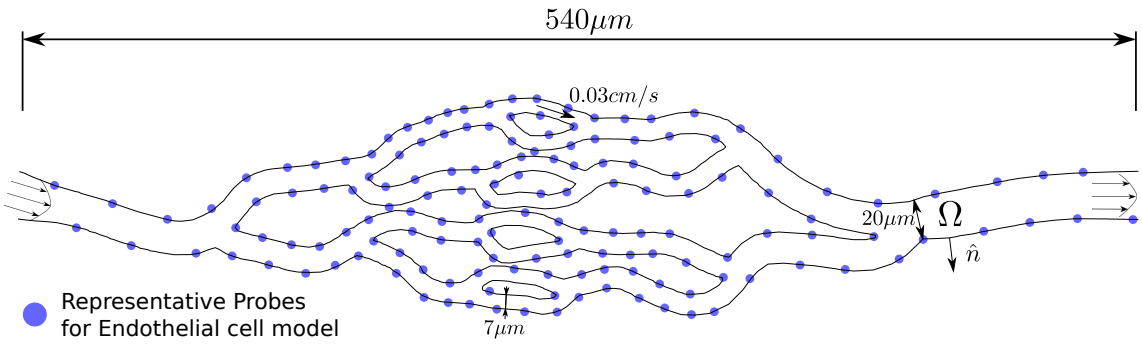

Figure 5.2: The vessel network geometry used in this simulation, taken from [Balogh and Bagchi, 2017]. Dots in purple are representative probes for endothelial cell models to collect ATP concentration and shear stress values.

condition, a RBC takes around 2s to traverse this network. For ATP concentration, a constant concentration a_∞ is fixed at the of the arteriole entrance and at the the venule exit, in order to adapt the mean ATP concentration known for blood plasma.

The Boundary condition for ATP concentration on vessel wall is modeled as ([Plank et al., 2006])

$$D_a \frac{\partial a}{\partial \vec{n}}\bigg|_{\partial\Omega} = -K_a \cdot a + S(\tau) \tag{5.2}$$

D_a is the diffusivity of ATP in blood plasma. $-K_a \cdot a$ on the right hand side of Eqn. (5.2) denotes a ATP up-taking effect from the endothelial wall. The term $S(\tau)$ describes the production rate of ATP on endothelial wall due to shear stress (τ) stimuli. It has a form of

$$S(\tau) = s_0 * \left[1 - \exp(-\frac{\tau}{\tau_m})\right]^3 \tag{5.3}$$

Here s_0 is the maximum ATP production rate per unit length, τ_m is the characteristic wall shear stress.

The release of ATP from RBCs into blood lumen is described as a boundary condition on moving RBCs membranes, which is a function of membrane shear stress and level of deformation (quantified by curvature change rate). The ATP problem was discussed in chapter 4. Following that chapter, we adopt a vesicle model for RBcs. The ATP release from RBC is modeled is also described in chapter 4 (see Eqn. (4.7), Eqn. (4.8 and table 4.1). From here on, we will not distinguish between the terms vesicle and RBC. We chose the characteristic radius for a vesicle $R_0 = 3\mu m$, then the area of a vesicle is $A = \pi R_0^2 \approx 28.3\mu m^2$. The reduced area of a vesicle (or RBC) in 2D, denoted as τ_{RA}, is defined as the ratio between the actual area and the area of

notation and value	description
$D_a = 2.36 \times 10^{-10} m^2 s^{-1}$	diffusion coefficient of ATP in blood lumen
$a_\infty = 100 nMol$	steady physiological plasma ATP concentration
$K_a = 1.68 \times 10^{-5} m s^{-1}$	ATP uptake rate
$s_0 = 10^{-3} nMol m s^{-1}$	maximum ATP production rate on EC surface
$\tau_m = 1 Pa$	characteristic wall shear stress

Table 5.1: parameters relevant to lumen ATP concentration, all values are taken from [Plank et al., 2006, John and Barakat, 2001]

a circle having the same perimeter. For definitness we set $\tau_{RA} = 0.7$. We define the hematocrit as the ratio between the total area of vesicles and the area of the vessel network, This value is fixed at 0.15, as it is a typical value in microcirculaiton. Table 5.1 presents parameters of ATP dynamics (in addition to the parameters defined in chapter 4). With ATP diffusivity D_a, the mean velocity in the finest capillary (around $0.03 cm/s$, see Fig. 5.2) and the capillary diameter (around $7 \mu m$, see Fig. 5.2), we estimate that the Peclet number in this case is roughly around 10, which means that the advection by flow field may play a relatively important role.

5.2.2 Modeling of Calcium Dynamics in Endothelial Cells

The acute calcium response of endothelial cells to flow change typically last around few hundreds to a thousand seconds [Wiesner et al., 1996, Wiesner et al., 1997, Plank et al., 2006]. We now estimate the characteristic time scale for diffusion inside a single endothelial cell. The size of typical endothelial cells is of about $d_{EC} = 10 \mu m$ in diameter and $2 \mu m$ in thickness. The effective diffusivity of free calcium ion inside an endothelial cell is around $D_{ca} = 10^{-12} m^2/s$ (data estimated from [Keener and Sneyd, 1998] by taking into account the effect from buffering proteins). The characteristic time for calcium diffusion inside a single cell is estimated as $t_c = d_{EC}^2 / D_{ca} \approx 10 s$. This characteristic time is quite small compared to the typical time scale of an acute response, thus, we model the calcium dynamics inside a single cell with spatial gradients omitted.

As a preliminary step, we fully adopt the calcium signaling model from [Plank et al., 2006]. Fig. 5.1 (right panel) provides a sketch of the main players for calcium dynamics in a single cell, the details can be found in [Plank et al., 2006]. We recall only the essential descriptions here, in correspondence with schematic plot in the right panel of Fig. 5.1 . The cytoplasmic free caicum ion concentration is termed as Ca_c. The binding of ATP to endothelial surface receptors forms a receptor-ligand complex, which triggers the activation of G-progein and phospholipase C and the **cleavage** of

PIP_2 (phosphatidylinositol 4,5-bisphosphate, which functions as an intermediate in the IP_3 pathway), and eventually form the second messenger IP_3 (Inositol trisphosphate, a main player in intracellular calcium dynamics). This process is formulated as

$$\frac{d[I](t)}{dt} = k_i \frac{a(t)}{K_c + a(t)} \frac{Ca_c}{K1 + Ca_c} - k_2[I]$$

Here $[I]$ denotes the IP_3 concentration, $a(t)$ is the ATP concentration at a particular location in the vessel network.

Successively, the IP_3 diffuses onto an internal calcium store (endoplasmic reticulum), triggers an influx of free calcium ions from internal store into cytoplasm. This influx is strengthened via a positive feedback , termed as CICR (calcium-induced calcium release [Plank et al., 2006, Tran et al., 2000]). This influx from internal store into cytosol is modeled as

$$q_{rel} = k3 \frac{Ca_c}{K_{CICR} + Ca_c} \left(\frac{[I]}{K2 + [I]} \right)^3 Ca_s$$

Here q_{rel} denotes the influx due to the CICR effect, Ca_s is the calcium concentration in the internal store. Another influx of calcium is due to the CCE effect (capacitative calcium entry [Putney et al., 2001]), which suggested that the depletion of internal calcium store triggers calcium influx from blood vessel lumen into cytoplasm. Together with the contribution from mechano-sensitive cation channels, this influx is described as

$$q_{in} = k_{CCE}(Ca_{s0} - Ca_s)(Ca_{ex} - Ca_c) + \frac{q_{max}}{1 + \alpha \exp(-W(\tau))}$$

Here the notations are: q_{in}– the influx of calcium concentration from vessel lumen, k_{CCE}–the CCE coefficient, Ca_{s0}–the characteristic calcium concentration of internal storage, Ca_{ex} and Ca_c are calcium concentration of vessel lumen (as a constant) and cytoplasmic calcium concentration, respectively. q_{max} is the maximum influx of mechano-sensitive cation channels. α and $W(\tau)$ are parameters which allow us to calculate probability of mechano-sensitive cation channels opening, which can be found in [Wiesner et al., 1996]. $W(\tau)$ is positively correlated with wall shear stress τ.

The dynamics of cytoplasmic calcium store is then described by setting the temporal variation of Ca_c as a sum of mainly the fluxes discussed above (other terms are compensated [Plank et al., 2006], such as q_{buff} which describes the binding of free cytoplasmic calcium to buffering protein, and q_res which describes the outflux from cytosol to blood lumen due to ATPase).

$$\frac{dCa_s}{dt} = q_{rel} + q_{in} - q_{buff} - q_{out}$$

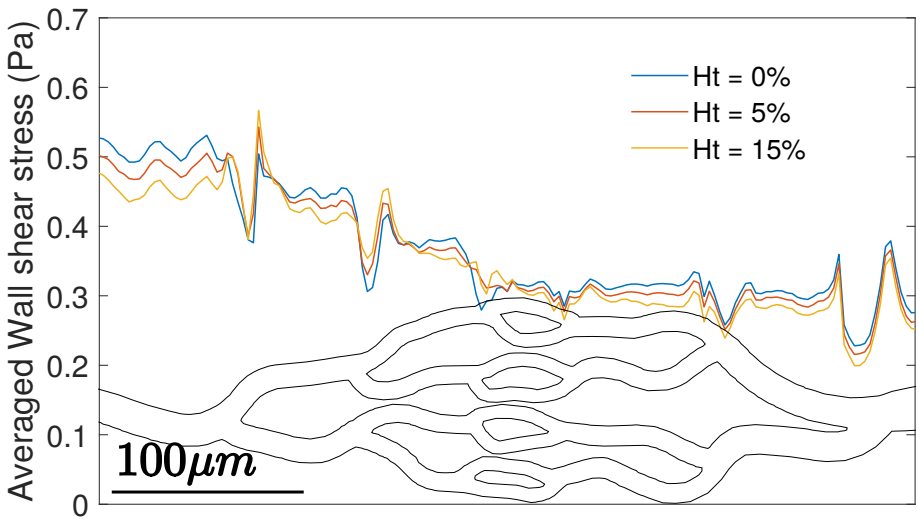

Figure 5.3: Averaged wall shear stress distribution in stream direction with different Ht. The effect from RBCs in this particular network and flow condition (fixed pressure drop) is minor.

A systematic investigation of the calcium dynamics and its coupling to flow and ATP release from RBCs is currently under investigation. Here, we only only discuss how input from ATP concentration and wall shear stress will qualitatively affect on calcium dynamics.

5.3 Results

Wall shear stress and wall concentration of ATP are the key inputs to endothelial calcium dynamics. We investigate on how changes in hematocrit shift the ATP concentration and wall shear stress distribution in this particular vessel network. Three hematocrit values, $Ht = 0\%$, 5% and 15% are investigated. Statistical results are evaluated after all transients due to initial conditions have decayed.

Figure 5.3 shows that the vessel network geometry (precisely the positions of bifurcation or convergences) is highly correlated with shear stress decreases. On the other hand, the presence of RBCs has only minor effects on averaged wall shear stress as pressure drop is fixed. In general, the wall shear stress with this magnitude around 0.3 to 0.5 Pa generates a relatively small amount of ATP, compaed to the amount in uptaking effect (see the first and the second terms on the right hand side of Eqn. (5.2)). It can be seen from Eqn. (5.3) that the production rate is sensitive to the choice of τ_m. We fix this value to a constant in this demonstrative case, despite that other values such as 0.1Pa and 10Pa were also suggested in [John and Barakat, 2001]

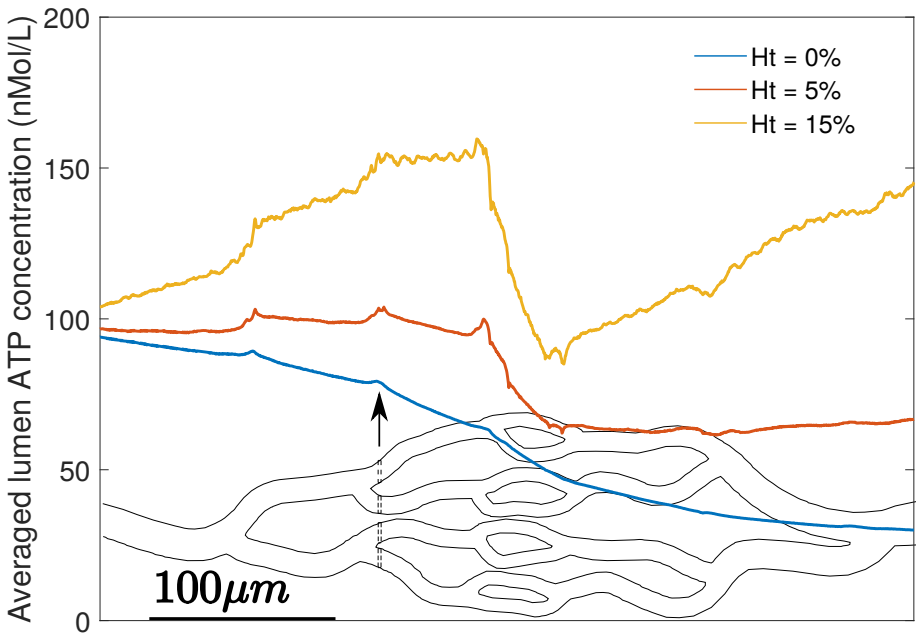

Figure 5.4: Averaged ATP concentration distribution in stream direction with different Ht. With the increase of hematocrit, capillaries at the arteriole side gains relatively higher ATP concentration, comparing to capilarries connecting to venule. This mean ATP concentration is calculated by averaging along the total cross section and time.

due to the adaptation to different flow conditions in different tissues.

Since the generation of ATP due to wall shear stress is relatively small, the dominance of uptaking effect on the endothelial–luman surface implies a descending distribution of ATP concentration from arteriole to capillary and to venule, which is observed in the simulation with $Ht = 0\%$ (see the blue curve in Fig. 5.4). In these results, the mean ATP concentration at a particular position is averaged both over time and over the total cross section (shown by the dashed lines in Fig. 5.4). As RBCs release ATP when deforming and subjected to membrane shear stress, we observed a dramatic increase of ATP concentration in branching arterioles. We think this is due to the RBCs' hitting at bifurcation, after which a RBC tends to have its lateral position closer to the wall, gaining a larger membrane shear stress (as we discussed in chapter 4). In addition, it can be seen from Snapshots in Fig. 5.5, that RBCs stay close to the center line in the feeding arteriole, but move close to wall after hitting a bifurcation, releasing thus more ATP. In the finest capillary, a drop in averaged ATP concentration is observed in Fig. 5.4). This could be attributed to the close contact between RBC membrane and endothelial wall which facilitates the ATP uptaking, as the uptaking rate is proportional to ATP concentration (see Eqn.

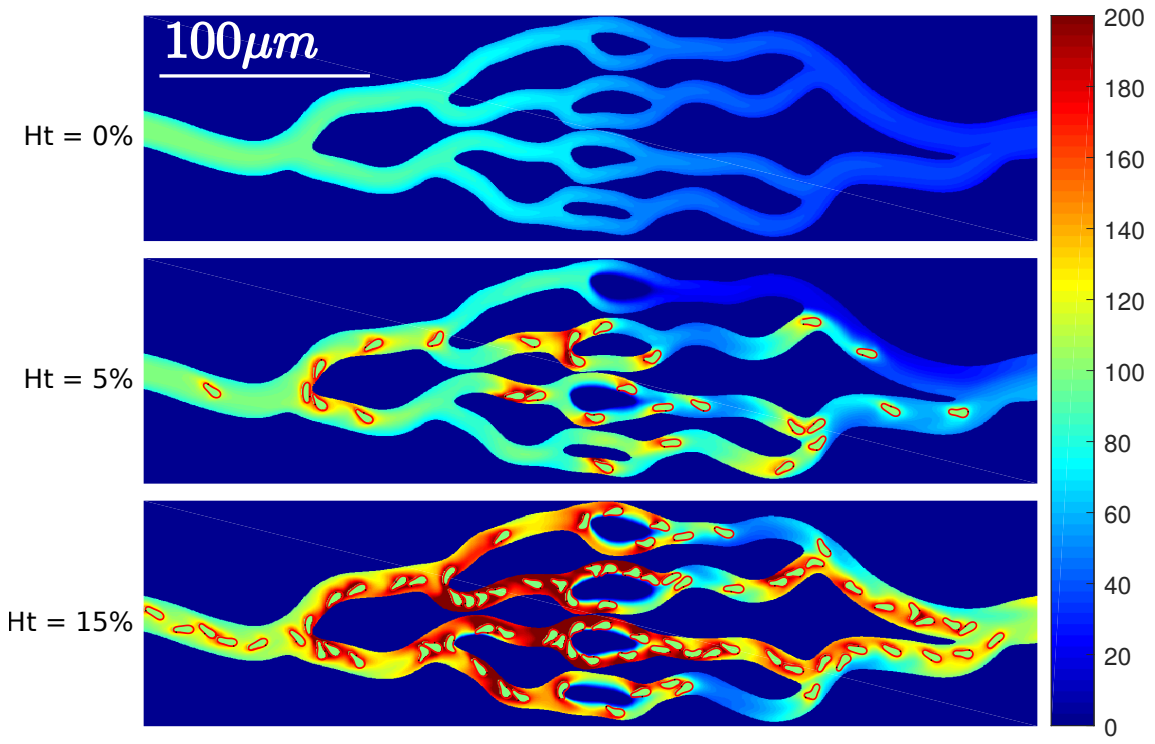

Figure 5.5: Snapshots for ATP concentration and RBC shapes in vessel network. The color bar represents the local ATP concentration (nMol/L)

5.2).

To sum up the results of ATP and wall shear stress distribution, in this particular vessel network and corresponding flow conditions, the RBCs boost in general the ATP concentration. The increase is larger in capillaries, on the arteriole side, than on the venule side. This effect is at present thought to be associated to the RBCs hitting bifurcation and undergoing high stress and deformation (which are the source of ATP release). After those events, RBCs migrate towards center and the deformation amplitude is reduced, resulting thus in a decline of ATP release.

5.4 Conclusion

In this chapter, we carried out the preliminary studies on the ATP signaling process and its coupling to mechanical properties of flood flow in micro circulation. By taking into account the ATP release model from chapter 4, we found that the presence of RBCs boost the ATP concentration. The concentration is found to the highest in capillaries close to the arteriole side. This may attributeed to RBCs' hitting bifurcations and their lateral migration towards center after bifurcations. The ATP

increase in capillaries on the venule side is relatively smaller. This could be a result of ATP uptaking by endothelial wall in the narrowest capillary, where the close gap between RBC membrane and vessel wall increases the ATP concentration along the wall, facilitating thus the uptaking rate. These effects are amplified with an increase in hematocrit. The wall shear stress, which is not affected much by the presence of RBCs, is maintained at around 0.3 to 0.5Pa in this particular flow condition. We are now in a position to study systematically the coupling to calcium signaling, that we are currently investigating.

Chapter 6

Conclusion

This thesis has been devoted to coupling between RBC dynamics and chemical solute dispersion in microcirculation. Below we sum up the main results and discuss the perspectives.

6.1 Summary and perspectives for Chapter 2

In chapter 2, the shape dynamics and rheological properties of vesicles (a widely used model of RBCs) in pressure-driven flow are systematically studied. By considering the effect of viscosity contrast λ, several branches of solutions were found, including centered parachute and slipper, snaking parachute, off-centered slipper and complex trilobe dynamics. We have shown that the trilobe shape is not a property to be linked to membrane cytoskeleton, unlike the claim in [Mauer et al., 2018]. In the analysis of multiple vesicle situations, we linked the rheology to spatial organization. A decrease of the normalized viscosity $[\eta]$ in relatively small concentration regime is confirmed in pressure-driven flow, and is not only a property associated to a shear flow [Thiébaud et al., 2014]. Interestingly, the result from pressure-driven flow (more relevant to blood circulation) shows that the normalized viscosity decrease in the range 0-15%, which is more or less the range of hematocrit in microcirculation. The spatial organizations of the cells tend to strongly moderate the increase with hematocrit; cells organize themselves into particular pattern (single and dense files in the center-line).

It would be interesting to investigate in the future whether the decrease of $[\eta]$ is a robust feature that also exists in 3D with more realistic models and for higher concentrations. A relevant work by [Thiébaud et al., 2014] pertaining to shear flow, had shown the same rheological tendency as in 2D. However their studies were confined to dilute suspension (around 5 %). It would also be an interesting task to investigate the spatial organizations in 3D.

6.2 Summary and perspectives for Chapter 3

In chapter 3, in order to tackle the chemical dispersions originated from or affected by moving RBCs in microcirculation, we developed a 2D advection diffusion solver based on Lattice Boltzmann Method. The key feature of this solver is that it can handle arbitrary moving boundaries and general boundary conditions. Based on asymptotic analysis, we proved that this boundary scheme enjoys a second order precision. This has also been confirmed by numerical simulations. By coupling this solver with an existing fluid–membrane solver [Shen et al., 2017a] in our laboratory, we managed to exemplify the capability of this solver for drug delivery in arterioles. We confirmed that with the assumption of instant absorption on vessel walls, when the margination effect of liposome (a rigid drug carrier with a round shape and a diameter around few micrometers) is strong, the presence of RBCs facilitates the absorption process. The results should be generalized to carry out systematic studies with multiple liposomes focusing on statistical effects, which could provide more insights into this problem.

Two interesting expansions on the numerical aspect could be carried out in the future. The first one: an extension to 3D. In that case a more elaborate ATP release model (e.g. taking into account shear elasticity due to cytoskeleton network). The second one: to make the boundary scheme inherently mass-conservative. The current scheme conserves mass well for cases with moderate Peclet numbers (such cases are frequent in biological cases, as we have encountered in this work). The introduction of mass conservation scheme can largely expand the solver's feasibility into applications involved with high Peclet numbers (e.g. dissipation and absorption of pollutant).

6.3 Summary and perspectives for Chapter 4

In chapter 4, we modeled the ATP release from a RBC by using both *in vitro* experimental data [Forsyth et al., 2011] and assumptions on the molecular level. Interestingly, a simple model was successful in capturing the essential behavior in comparison to experimental data. A plateau of release level against apparent shear stress $\sigma_{app} \leq 3Pa$, and an increase of release when $\sigma_{app} > 3Pa$, see Fig. 4.2 upper panel for experimental results and Fig. 4.6 lower panel for simulation results. Later on, this model was implemented in pipe flow and bifurcations, which are representative cases of blood microcirculation. We found that a lifting process appears to happen after a RBC hits a bifurcation. This can contribute to a substantial portion to ATP release. This implies that the complexity of the geometry of capillary and

pre-capillary arteriole network may boost the mechanically dependent ATP release in the microvasculature.

This ATP release model is a concise one that represents several of the essential behaviors of *in vitro* experiments [Forsyth et al., 2011]. For quantitative comparison with respect to the experiments, one requires a more elaborate model. For example, in some other experiments, such as [Wan et al., 2008] a lag between mechanical stimulus and ATP release (around 0.05 to 0.08 seconds) has been observed. Taking into account these effects in the model will strengthen its reliability in more generic scenarios such as in larger arterioles (where the blood flow is much faster than in capillaries that will amplify the effect of this lag effect).

6.4 Summary and perspectives for Chapter 5

In chapter 5, we carried out preliminary studies on the ATP signaling process. By adopting the model of ATP release from RBCs in chapter 4, we were able to calculate the ATP distribution in a capillary network. The calcium signaling of endothelial cells is triggered by change in wall shear stress and ATP concentration in the blood lumen. We have demonstrated the capability of our fluid–membrane–solute solver to couple ATP distribution to the intracellular calcium signals. Further explorations need to be done by considering the effect from gap junctions (which may induce intercellular calcium waves).

Finally, it will be an interesting task to implement a realistic capillary network, so that the geometrical effects can be estimated directly from simulations.

Appendix A

Asymptotic Analysis for Advection-diffusion Lattice-Boltzmann Method and the Boundary Treatment

A.1 Asymptotic Analysis of the Bulk Equations and Boundary Conditions

In this appendix, we show on one hand that the lattice-Boltzmann equations are equivalent in the asymptotic limit to the advection-diffusion equation and on the other hand they allow to derive the boundary conditions (Eq. (3.13)); see [Huang and Yong, 2015]. Similar procedures were used in [Junk et al., 2005, Yoshida and Nagaoka, 2010] for other strategy of handling boundary conditions, different from that given by Eq. (3.13) (which we may view as a modified bounce-back scheme). By using our strategy, we will prove analytically here that this boundary condition enjoys a second order precision. We deal here with the zigzag boundary which is defined to pass through the middle of the mesh segment (dashed line in Fig. 3.1 (b)). It is this choice that allowed us to reach the second-order precision.

Let us first introduce the diffusive scaling which is based on the idea of finding a suitable pair of scaling size (which is also the numerical mesh size) $(\Delta t, \Delta x)$ that makes the diffusivity in numerical simulation $D^{'}$ (as it was defined in Eq. (3.9)) close to $O(1)$ in magnitude. This conditions reads

$$D^{'} = \frac{\Delta t}{\Delta x^2} D \sim O(1) \tag{A.1}$$

The following choice of scales satisfies our constraint

$$\begin{aligned} \Delta t &= a\epsilon^2 \\ \Delta x &= \epsilon \end{aligned} \tag{A.2}$$

Here $a = \Delta t/\Delta x^2 = D^{'}/D$ is a constant value representing the ratio between numerical diffusivity $D^{'}$ and physical diffusivity D. The factor ϵ is a small parameter and is often introduced in this way in the context of asymptotic analysis. Accordingly the scaling of velocity is given by

$$\mathbf{u}^{'} = \frac{\Delta t}{\Delta x}\mathbf{u} = a\epsilon\mathbf{u} \tag{A.3}$$

Our asymptotic analysis below obtained in the limit $\epsilon \to 0$ will show that (i) the Boltzmann equation recovers the advection-diffusion equation, and (ii) the convergence to the advection-diffusion equation if of order $O(\epsilon^2)$ for both the bulk equations and the boundary conditions.

The Boltzmann equation (combining collision and streaming process (Eqs, (3.5 - 3.7)) reads, by omitting the reaction term, as

$$g_i(t + a\epsilon^2, \mathbf{x} + \hat{c}_i\epsilon) - g_i = \frac{1}{\tau}\left[w_i c(1 + 3a\mathbf{u}\cdot\hat{c}_i\epsilon) - g_i\right] \tag{A.4}$$

The unspecified argument in g_i is $(t, \mathbf{x})$ and is omitted here, $\hat{c}_i = \mathbf{c}_i/(\Delta x/\Delta t)$ is the normalized unit vector of micro velocities defined in Eq. (3.4).

We will expand g_i and c in powers of ϵ up to third order. It turns out that the second order provides the leading order contribution for the advection-diffusion problem, whereas the third order is necessary for obtaining the desired precision. The expansion reads

$$\begin{cases} g_i = g_i^{(0)} + \epsilon g_i^{(1)} + \epsilon^2 g_i^{(2)} + \epsilon^3 g_i^{(3)} + O(\epsilon^4) \\ c = c^{(0)} + \epsilon c^{(1)} + \epsilon^2 c^{(2)} + \epsilon^3 c^{(3)} + O(\epsilon^4) \end{cases} \tag{A.5}$$

Expanding Eq. (A.4) in power series of ϵ and ignoring terms of higher order than ϵ^3 we obtain

$$\begin{aligned} g_i(t + a\epsilon^2, \mathbf{x} + \hat{c}_i\epsilon) - g_i = &\sum_{n=1}^{3} \frac{1}{n!}\left(a\epsilon^2\frac{\partial}{\partial t} + \epsilon(\hat{c}_i\cdot\nabla)\right)^n g_i \\ &+ O(\epsilon^4) \end{aligned} \tag{A.6}$$

For Eq. (3.1) we get

$$\sum_{n=0}^{3}\left(c^{(n)} - \sum_{i=0}^{4} g^{(n)}\right)\epsilon^n + O(\epsilon^4) = 0 \tag{A.7}$$

Equating terms of similar order in ϵ in (A.7) provides

$$c^{(n)} = \sum_{i=0}^{4} g_i^{(n)} \tag{A.8}$$

Reporting (A.5) and (A.6) into (A.4) we obtain, by equating terms of the same order, the following hierarchical equations

$$\begin{aligned}
g_i^{(0)} =& w_i c^{(0)} \\
g_i^{(1)} =& w_i c^{(1)} + \frac{1}{2} a \hat{c}_i \cdot \mathbf{u} c^{(0)} - \tau (\hat{c}_i \cdot \nabla) g_i^{(0)} \\
g_i^{(2)} =& w_i c^{(2)} + \frac{1}{2} a \hat{c}_i \cdot \mathbf{u} c^{(1)} - \tau (\hat{c}_i \cdot \nabla) g_i^{(1)} - \tau \left[a \frac{\partial}{\partial t} + \frac{1}{2} (\hat{c}_i \cdot \nabla)^2 \right] g_i^{(0)} \\
g_i^{(3)} =& w_i c^{(3)} + \frac{1}{2} a \hat{c}_i \cdot \mathbf{u} c^{(2)} - \tau (\hat{c}_i \cdot \nabla) g_i^{(2)} - \tau \left[a \frac{\partial}{\partial t} + \frac{1}{2} (\hat{c}_i \cdot \nabla)^2 \right] g_i^{(1)} - \\
& \tau \left[a (\hat{c}_i \cdot \nabla) \frac{\partial}{\partial t} + \frac{1}{6} (\hat{c}_i \cdot \nabla)^3 \right] g_i^{(0)}
\end{aligned} \tag{A.9}$$

By summing over i (from 0 to 4) the first equation in (A.9), and using Eq.(A.8) and the fact that the weight factors obey $\sum_{i=0}^{4} w_i = 1$, we find that the resulting equation is automatically satisfied. Performing the same operation with the second equation yields the same conclusion, by using Eq.(A.8) and the first equation in (A.9), and by virtue of the fact that $\sum_{i=0}^{4} \hat{c}_i = 0$, and that w_i enjoys a symmetry property ($w_1 = w_2$ and $w_3 = w_4$). Performing again the same operation with the third equation, and using the previous orders results leads (after simple algebraic manipulations) to an advection diffusion equation

$$\frac{\partial c^{(0)}}{\partial t} + \mathbf{u} \cdot \nabla c^{(0)} = \nabla \cdot \left[\frac{2\tau - 1}{6a} \nabla c^{(0)} \right] \tag{A.10}$$

Finally, performing the same operation with the last equation yields

$$\frac{\partial c^{(1)}}{\partial t} + \mathbf{u} \cdot \nabla c^{(1)} = \nabla \cdot \left[\frac{2\tau - 1}{6a} \nabla c^{(1)} \right] \tag{A.11}$$

This proves that the lattice Boltzmann scheme (A.4) converges to the advection diffusion equation with an error term $O(\Delta x^2)$. The relation between diffusivity D and relaxation time τ is given by $(2\tau - 1)/(6a) = D$, which also gives $\tau = 3\Delta t / \Delta x^2 D + 1/2$.

A.2 Boundary Condition: A Modified Half-Way Bounce-Back Scheme

In this section, we attempt to explain the boundary scheme for the static zigzag boundary, which is given by Eq. (3.13). This relation has been originally proposed

in Ref. [Huang and Yong, 2015], in which, a second-order convergence is observed in numerical experiments [Huang et al., 2016]. We present here a simplified derivation for the particular zigzag boundary which intersects with mesh segments only at middle points (dashed-dotted line in Fig.3.1 b). Our derivation will prove analytically the second order precision.

A representative point of the discretized boundary is designated as $\mathbf{M}$ in Fig. 3.2, and $\mathbf{x}$ is a lattice point next to the boundary, and we have the relation $\mathbf{M} = \mathbf{x} - 1/2\hat{c}_i\Delta x$. A Dirichlet boundary condition is defined as $c(\mathbf{M}) = \alpha_{3,D}^{(mid)}$, whereas a Neumann boundary condition, since the normal direction of the zigzag boundary coincides with $\hat{c}_{\bar{i}}$, can be written as $(\hat{c}_{\bar{i}} \cdot \nabla)c(\mathbf{M}) = \alpha_{3,N}^{(mid)}$. The subscript D and N represents Dirichlet and Neumann respectively. $\bar{i}$ is an index which corresponds to inverse direction of $\hat{c}_i$, that is $\hat{c}_{\bar{i}} = -\hat{c}_i$. However, in the LMB spirit $c(\mathbf{M})$ is not known, since the concentration field is defined at the lattice points only. Therefore we have to express $c(\mathbf{M})$ as a function of its nearest lattice point located at $\mathbf{x}$. By expanding these boundary around the lattice point at position $\mathbf{x}$ we obtain

$$\begin{aligned}
\alpha_{3,D}^{(mid)} &= c(\mathbf{M}) \\
&= c - \frac{1}{2}\epsilon(\hat{c}_{\bar{i}} \cdot \nabla)c + O(\epsilon^2) \\
&= \left[c^{(0)} - (\frac{1}{2}(\hat{c}_i \cdot \nabla)c^{(0)} - c^{(1)})\right]\epsilon + O(\epsilon^2) \\
\alpha_{3,N}^{(mid)} &= (\hat{c}_{\bar{i}} \cdot \nabla)c(\mathbf{M}) \\
&= -(\hat{c}_i \cdot \nabla)c + \epsilon\frac{1}{2}(\hat{c}_i \cdot \nabla)^2 c + O(\epsilon^2) \\
&= (\hat{c}_i \cdot \nabla)\left[c^{(0)} - \epsilon(\frac{1}{2}(\hat{c}_i \cdot \nabla)c^{(0)} - c^{(1)})\right] + O(\epsilon^2)
\end{aligned} \tag{A.12}$$

For brevity, all unspecified arguments on the right hand side are understood to be $(\mathbf{x}, t)$.

The main question now is how to substitute the streaming step (3.6) at the boundary, in a such a way to respect the above boundary conditions. $g_i(t + \Delta t, \mathbf{x})$ is the unknown incoming distribution function that needs to be determined. Inspired by the traditional bounce back condition (for Navier-stokes equation) we introduce the distribution $g_{\bar{i}}^*(t, \mathbf{x})$, which is the known post-collision distribution function (defined by Eq. (3.5)), but defined for opposite micro velocities; the subscript $\bar{i}$ means that the corresponding micro velocity direction is pointing outward (see $\hat{c}_{\bar{i}}$ in Fig. 3.2). The classical bounce-back boundary condition is given by $g_i(t + \Delta t, \mathbf{x}) = g_{\bar{i}}^*(t, \mathbf{x})$ for zero-flux boundary condition in the pure diffusion problem (the relation is analogous

to the non-slip boundary condition in Navier-Stokes LBM). This is quite intuitive, since from time t to $t+1$ the number of particle crossing the boundary from each side is equal and opposite. The question is how to extend this relation to the present problem.

To deal with this question, we use the same asymptotic expansion in powers if ϵ, as performed in the preceding appendix, for $g_{\bar{i}}^*(t,\mathbf{x})$ and $g_i(t+\Delta t,\mathbf{x})$. With the help of the post-collision and equilibrium distribution function definition (Eq. (3.5) and (3.7)) and the asymptotic expansion (equation (A.9)),we find for $g_{\bar{i}}^*(t,\mathbf{x})$ and $g_i(t+\Delta t,\mathbf{x})$ the following expressions up second order in ϵ

$$
\begin{aligned}
g_{\bar{i}}^*(t,\mathbf{x}) =& g_{\bar{i}}(t,\mathbf{x}) + \frac{1}{\tau}(g_{\bar{i}}^{eq} - g_{\bar{i}}) \\
=& w_i c^{(0)} + \epsilon w_i \left(-(3a\hat{c}_i\cdot\mathbf{u} - (\tau-1)(\hat{c}_i\cdot\nabla))c^{(0)} + c^{(1)}\right) + \\
& \epsilon^2 w_i \left\{ (\tau-1)[(\tau-\frac{1}{2})(\hat{c}_i\cdot\nabla)^2 - 3a\hat{c}_i\cdot\mathbf{u}(\hat{c}_i\cdot\nabla) - a\frac{\partial}{\partial t}]c^{(0)} - \right. \\
& \left. (3a\hat{c}_i\cdot\mathbf{u} - (\tau-1)(\hat{c}_i\cdot\nabla))c^{(1)} + c^{(2)} \right\} + \\
& O(\epsilon^3) \\
g_i(t+\Delta t,\mathbf{x}) =& g_i(t,\mathbf{x}) + a\epsilon^2\frac{\partial}{\partial t}g_i + O(\epsilon^3) \\
=& w_i c^{(0)} + \epsilon w_i \left((3a\hat{c}_i\cdot\mathbf{u} - (\tau-1)(\hat{c}_i\cdot\nabla))c^{(0)} + c^{(1)}\right) + \\
& \epsilon^2 w_i \left\{ [\tau(\tau-\frac{1}{2})(\hat{c}_i\cdot\nabla)^2 - \tau 3a\hat{c}_i\cdot\mathbf{u}(\hat{c}_i\cdot\nabla) - (\tau-1)a\frac{\partial}{\partial t}]c^{(0)} + \right. \\
& \left. (3a\hat{c}_i\cdot\mathbf{u} - \tau(\hat{c}_i\cdot\nabla))c^{(1)} + c^{(2)} \right\} + \\
& O(\epsilon^3)
\end{aligned}
\tag{A.13}
$$

Here the symmetrical structure of the micro velocities $\hat{c}_i + \hat{c}_{\bar{i}} \equiv 0$ has been exploited. A close inspection of the above equations and the boundary conditions (A.12) allow one to infer the proper writing of the streaming process. Indeed, summation and subtraction of $g_i(t+\Delta t,\mathbf{x})$ and $g_{\bar{i}}^*(t,\mathbf{x})$ provide interesting results if one focuses on zeroth and first order terms only. The results are given by

$$\begin{aligned}\frac{g_i^*(t,\mathbf{x})+g_i(t+\Delta t,\mathbf{x})}{2w_i} &= \left[c^{(0)}-\epsilon(\frac{1}{2}(\hat{c}_i\cdot\nabla)c^{(0)}-c^{(1)})\right]+O(\epsilon^2)\\ \frac{g_i^*(t,\mathbf{x})-g_i(t+\Delta t,\mathbf{x})}{2w_i\epsilon} &= 3a\hat{c}_i\cdot\mathbf{u}\left[c^{(0)}-\epsilon(\frac{1}{2}(\hat{c}_i\cdot\nabla)c^{(0)}-c^{(1)})\right]-\\ &\quad(\tau-\frac{1}{2})(\hat{c}_i\cdot\nabla)\left[c^{(0)}-\epsilon(\frac{1}{2}(\hat{c}_i\cdot\nabla)c^{(0)}-c^{(1)})\right]+O(\epsilon^2)\end{aligned} \tag{A.14}$$

Interestingly, the right hand sides of Eqs. (A.14) are linear combination of the boundary condition (Eq.(A.12)), and in addition they both have the same magnitude regarding the error term $O(\epsilon^2)$. By substituting $\alpha_{3,D}^{(mid)}$ and $\alpha_{3,N}^{(mid)}$ into Eq.(A.14), the boundary scheme (Eq. (3.13)) can be straightforwardly extracted. Note that in the special case when $\mathbf{u}\equiv 0$ and $\alpha_{3,N}^{(mid)}\equiv 0$, the boundary scheme will coincide with the classical bounce-back one. An important point is worth of mention. The choice of the zigzag boundary passing precisely at the middle of the lattice segments is not innocuous. Had we chosen another definition, then the precision would have degraded to lower order, namely $O(\epsilon)$ instead of $O(\epsilon^2)$.

Appendix B

The Miscellaneous for ATP Release by Red Blood Cells Under Flow Study

B.1 Mean membrane / apparent shear stress in shear simulation

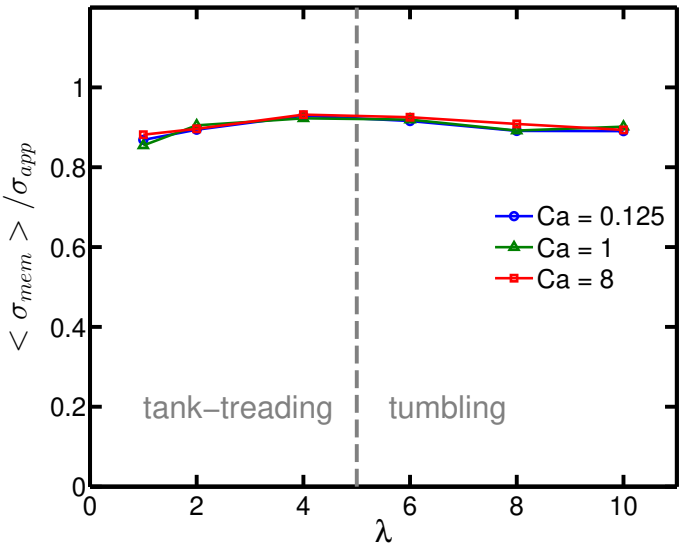

Figure B.1: shear stress vs viscosity contrast

B.2 ATP release level under shear with different μ_{in} and fixed $\mu_{ex} = 0.001Pa$

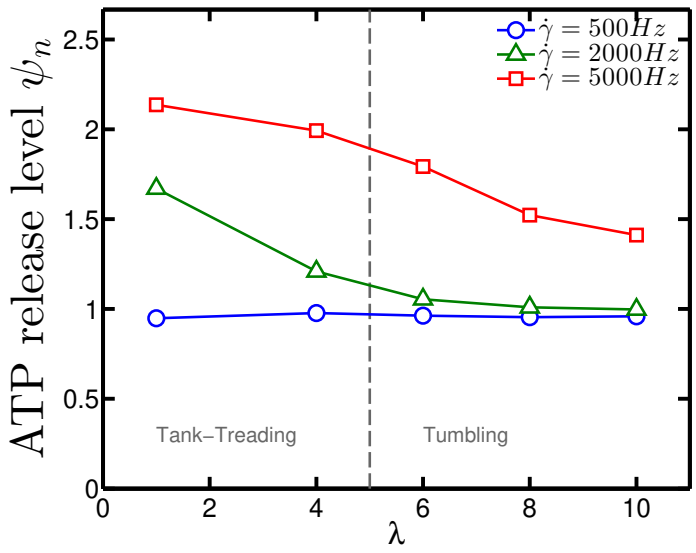

Figure B.2: Under linear shear flow with an adequately large shear rate, increasing μ_{in} (as well as $\lambda = \mu_{in}/\mu_{ex}$) results in a drop of ATP release level due to the reduction of curvature change in TT to TB transition.

B.3 Mean shear stress and deformation level in a long straight channel

Since the gray dashed line in Fig. B.4 represents the critical curvature change $\dot{c}_c = 200\mu m^{-1}s^{-1}$, it is clearly seen that the ATP release levels in long straight channel are not affected by shape deformation, but only by shear stress.

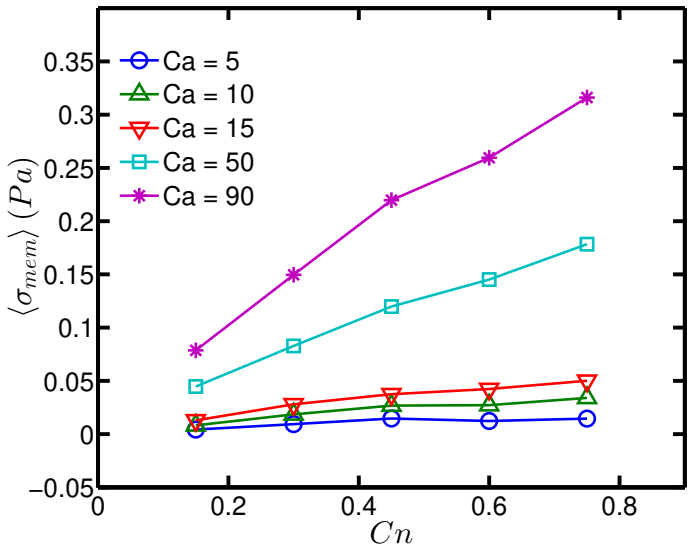

Figure B.3: mean shear stress in long straight channel

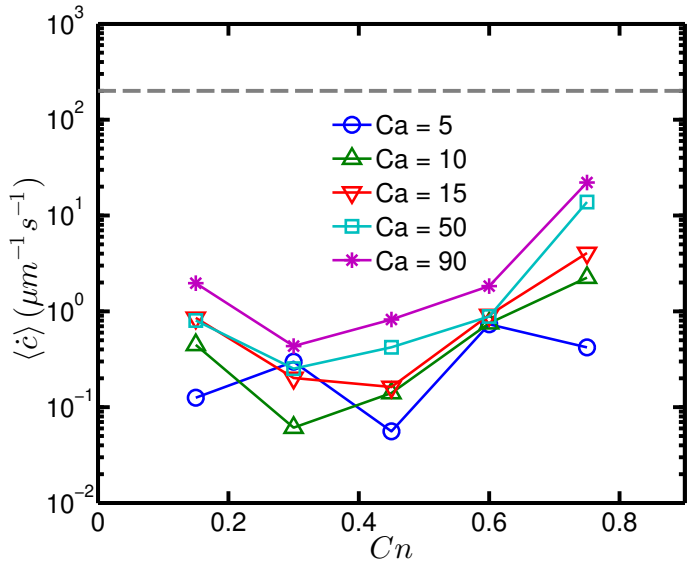

Figure B.4: mean curvature change in long straight channel

B.4 Estimation of the phenomenological ATP flux coefficient k_σ

From the experimental configuration in [Forsyth et al., 2011] we know that the RBC solution has a Hematocrit $h_t = 1\%$. The suspension is subjected to a linear shear flow for a period of time $T = 30s$. Comparing to typical plasma ATP concentration $a_0 = 1000nmol/L$ (value from [Gorman et al., 2007]), the experiments [Forsyth et al., 2011] reported that the relative amount (compared to static conditions) of ATP release is three-fold, $f = 3$, in the plateau regime of Fig. 4.2 (upper) in the main text. The total amount of ATP release from a RBC during this 30s can then be estimated as

$$\Phi_{tot} = f a_0 \cdot (\frac{4}{3}\pi R_0^3 \tau / h_t) \tag{B.1}$$

Since our ATP release criterion is based on the surface stress of the cell, k_σ has a dimension of a flux per unit area and unit time, and taking $4\pi R_0^2$ for the area of a RBC, we obtain the following estimate for k_σ

$$\begin{aligned} k_\sigma &\approx \frac{\Phi_{tot}}{4\pi R_0^2 \cdot T} \\ &\approx 7 \times 10^3 (nmol/L) \cdot \mu m/s \end{aligned} \tag{B.2}$$

Recall that the characteristic radius $R_0 = 3\mu m$ and the reduced volume (or reduced area in 2D) $\tau = 0.7$.

B.5 Lateral migration of a RBC after bifurcation

We have investigate different angles (defined in Fig. B.5) between feeding channel and down-stream branch channels. The angles are varied in the range of $0° < \theta_1, \theta_2 < 90°$ with an indentation of 30°. Moreover, we have initially set the vesicle at different positions, such are: center-line (lateral position 0), faster zone (lateral position 0.25) and slower zone (lateral position -0.25); see Fig. B.5. The capillary numbers are taken as $Ca = 5$ and 50 (Ca as defined in the article, is proportional to velocity). The confinement $Cn = 0.3$ is chosen to be the same value as in the main text.

We find for most cases that when a vesicle is initially located at the center-line it will be "scattered" to an off-centered lateral position (the middle panel in Fig. B.5 (b)). Consider a vesicle in a vessel network, which has been off-centered. After some time it has some probability to go back to the center-line if it enters the faster zone of a daughter branch (the upper panel in Fig. B.5 (b)). However, even if it goes back to the centerline by this scenario, this vesicle will be again scattered towards off-centered position after the next bifurcation. When a vesicle enter the slower zone, its probability to get off-centered becomes high.

This gives a hint to the idea that within a complex vessel network (with many bifurcations), an RBC will often go to off-center position due to the presence of bifurcations.

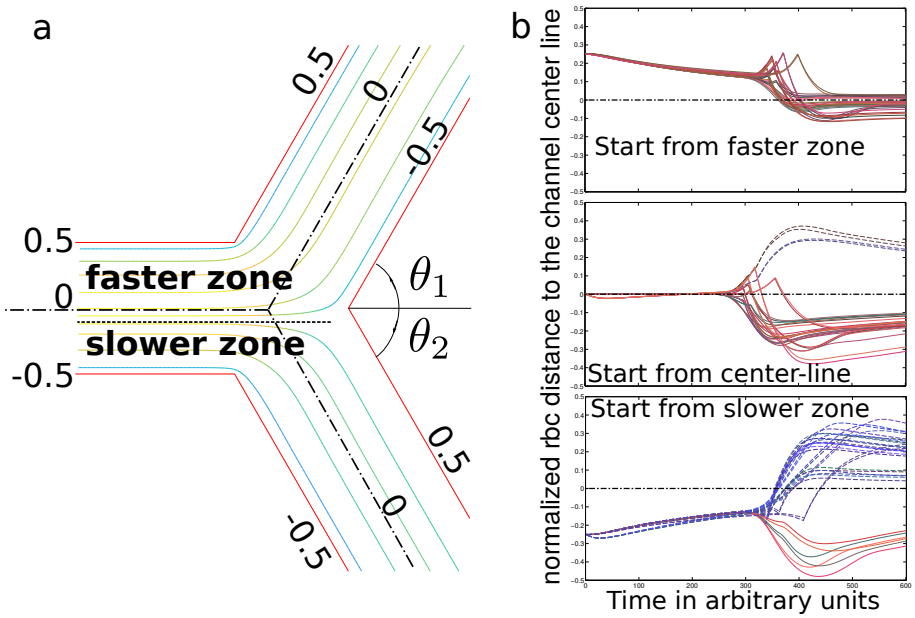

Figure B.5: (a) Schematic for definition of θ_1, θ_2, normalized lateral position and faster (upper) / slower (lower) zone. The dashed line represents the border (or separation line) for streamlines entering faster or slower branch. The dashed-dotted lines represent the centerlines of feeding and branching channels. A normalized lateral distance of two parallel walls in a given channel is defined as -0.5 and 0.5, counted from the centerline (the latter is defined to be the zero line). (b) Simulation results with different bifurcation angles, initial position and speeds. Curves on the right panel with a color close to red indicate that the RBCs enter the faster branch, while colors close to blue refer to RBCs entering the slower branch.

References

[Abkarian and Viallat, 2008] Abkarian, M. and Viallat, A. (2008). Vesicles and red blood cells in shear flow. *Soft Matter*, 4(4):653–657.

[Akbarzadeh et al., 2013] Akbarzadeh, A., Rezaei-Sadabady, R., Davaran, S., Joo, S. W., Zarghami, N., Hanifehpour, Y., Samiei, M., Kouhi, M., and Nejati-Koshki, K. (2013). Liposome: classification, preparation, and applications. *Nanoscale Res. Lett.*, 8(1):102.

[Allen and Cullis, 2013] Allen, T. M. and Cullis, P. R. (2013). Liposomal drug delivery systems: from concept to clinical applications. *Adv. Drug Deliv. Rev*, 65(1):36–48.

[Ando and Yamamoto, 2013] Ando, J. and Yamamoto, K. (2013). Flow detection and calcium signalling in vascular endothelial cells. *Cardiovasc Res.*, 99(2):260–268.

[Aouane et al., 2014a] Aouane, O., Thiébaud, M., Benyoussef, A., Wagner, C., and Misbah, C. (2014a). Vesicle dynamics in a confined poiseuille flow: From steady state to chaos. *Phys. Rev. E*, 90(3):033011.

[Aouane et al., 2014b] Aouane, O., Thiébaud, M., Benyoussef, A., Wagner, C., and Misbah, C. (2014b). Vesicle dynamics in a confined poiseuille flow: From steady state to chaos. *Phys. Rev. E*, 90:033011.

[Audet and Olbricht, 1987] Audet, D. and Olbricht, W. (1987). The motion of model cells at capillary bifurcations. *Microvasc. Res.*, 33(3):377–396.

[Balogh and Bagchi, 2017] Balogh, P. and Bagchi, P. (2017). Direct numerical simulation of cellular-scale blood flow in 3d microvascular networks. *Biophys. J*, 113(12):2815–2826.

[Barakat, 2013] Barakat, A. I. (2013). Blood flow and arterial endothelial dysfunction: Mechanisms and implications. *Comptes Rendus Physique*, 14(6):479–496.

[Barbee and Cokelet, 1971] Barbee, J. H. and Cokelet, G. R. (1971). The fahraeus effect. *Microvasc. Res.*, 3(1):6–16.

[Barber et al., 2008] Barber, J. O., Alberding, J. P., Restrepo, J. M., and Secomb, T. W. (2008). Simulated two-dimensional red blood cell motion, deformation, and partitioning in microvessel bifurcations. *Ann. Biomed. Eng.*, 36(10):1690–1698.

[Betz et al., 2009] Betz, T., Lenz, M., Joanny, J.-F., and Sykes, C. (2009). Atp-dependent mechanics of red blood cells. *Proc. Natl. Acad. Sci. USA*, 106(36):15320–15325.

[Brust et al., 2014] Brust, M., Aouane, O., Thiébaud, M., Flormann, D., Verdier, C., Kaestner, L., Laschke, M., Selmi, H., Benyoussef, A., Podgorski, T., et al. (2014). The plasma protein fibrinogen stabilizes clusters of red blood cells in microcapillary flows. *Sci. Rep.*, 4:4348.

[BURNSTOCK, 1999] BURNSTOCK, G. (1999). Release of vasoactive substances from endothelial cells by shear stress and purinergic mechanosensory transduction. *J. Anat.*, 194(3):335–342.

[Cantat and Misbah, 1999] Cantat, I. and Misbah, C. (1999). Lift force and dynamical unbinding of adhering vesicles under shear flow. *Phys. Rev. Lett.*, 83(4):880.

[Chasan et al., 2002] Chasan, B., Geisse, N. A., Pedatella, K., Wooster, D. G., Teintze, M., Carattino, M. D., Goldmann, W. H., and Cantiello, H. F. (2002). Evidence for direct interaction between actin and the cystic fibrosis transmembrane conductance regulator. *Eur Biophys J.*, 30(8):617–624.

[Chen and Lai, 2014] Chen, K.-Y. and Lai, M.-C. (2014). A conservative scheme for solving coupled surface-bulk convection–diffusion equations with an application to interfacial flows with soluble surfactant. *J. Comput. Phys*, 257:1–18.

[Chen et al., 2013a] Chen, Q., Zhang, X., and Zhang, J. (2013a). Improved treatments for general boundary conditions in the lattice boltzmann method for convection-diffusion and heat transfer processes. *Phys. Rev. E*, 88(3):033304.

[Chen et al., 2013b] Chen, Q., Zhang, X., and Zhang, J. (2013b). Improved treatments for general boundary conditions in the lattice boltzmann method for convection-diffusion and heat transfer processes. *Phys. Rev. E*, 88(3):033304.

[Chen and Doolen, 1998] Chen, S. and Doolen, G. D. (1998). Lattice boltzmann method for fluid flows. *Annu. Rev. Fluid Mech*, 30(1):329–364.

[Coupier et al., 2012] Coupier, G., Farutin, A., Minetti, C., Podgorski, T., and Misbah, C. (2012). Shape diagram of vesicles in poiseuille flow. *Phys. Rev. Lett.*, 108(17):178106.

[Coupier et al., 2008] Coupier, G., Kaoui, B., Podgorski, T., and Misbah, C. (2008). Noninertial lateral migration of vesicles in bounded poiseuille flow. *Phys. Fluids*, 20(11):111702.

[Crecelius et al., 2011] Crecelius, A. R., Kirby, B. S., Richards, J. C., Garcia, L. J., Voyles, W. F., Larson, D. G., Luckasen, G. J., and Dinenno, F. A. (2011). Mechanisms of atp-mediated vasodilation in humans: modest role for nitric oxide and vasodilating prostaglandins. *Am. J Physiol. Heart Circ. Physiol.*, 301(4):H1302–H1310.

[Davies, 1995] Davies, P. F. (1995). Flow-mediated endothelial mechanotransduction. *Physiol. Rev*, 75(3):519–560.

[Dietrich et al., 2000] Dietrich, H. H., Ellsworth, M. L., Sprague, R. S., and Ralph G. Dacey, J. (2000). Red blood cell regulation of microvascular tone through adenosine triphosphate. *Am. J. Physiol. Heart Circ. Physiol.*, 278(4):H1294–H1298. PMID: 10749727.

[Doyeux et al., 2011] Doyeux, V., Podgorski, T., Peponas, S., Ismail, M., and Coupier, G. (2011). Spheres in the vicinity of a bifurcation: elucidating the zweifach–fung effect. *J. Fluid Mech.*, 674:359–388.

[Dubyak and el Moatassim, 1993] Dubyak, G. R. and el Moatassim, C. (1993). Signal transduction via p2-purinergic receptors for extracellular atp and other nucleotides. *Am. J. Physiol. Cell Physiol.*, 265(3):C577–C606.

[Duncker and Bache, 2008] Duncker, D. J. and Bache, R. J. (2008). Regulation of coronary blood flow during exercise. *Physiol. Rev.*, 88(3):1009–1086.

[Ellsworth et al., 2009] Ellsworth, M. L., Ellis, C. G., Goldman, D., Stephenson, A. H., Dietrich, H. H., and Sprague, R. S. (2009). Erythrocytes: oxygen sensors and modulators of vascular tone. *Physiology*, 24(2):107–116.

[Fahraeus and Lindqvist, 1931] Fahraeus, R. and Lindqvist, T. (1931). The viscosity of the blood in narrow capillary tubes. *American Journal of Physiology-Legacy Content*, 96(3):562–568.

[Farutin and Misbah, 2011] Farutin, A. and Misbah, C. (2011). Symmetry breaking of vesicle shapes in poiseuille flow. *Phys. Rev. E*, 84(1):011902.

[Farutin and Misbah, 2012] Farutin, A. and Misbah, C. (2012). Squaring, parity breaking, and s tumbling of vesicles under shear flow. *Phys. Rev. Lett.*, 109(24):248106.

[Farutin and Misbah, 2013] Farutin, A. and Misbah, C. (2013). Analytical and numerical study of three main migration laws for vesicles under flow. *Phys. Rev. Lett.*, 110(10):108104.

[Farutin and Misbah, 2014] Farutin, A. and Misbah, C. (2014). Symmetry breaking and cross-streamline migration of three-dimensional vesicles in an axial poiseuille flow. *Phys. Rev. E*, 89(4):042709.

[Fedosov et al., 2014] Fedosov, D. A., Peltomäki, M., and Gompper, G. (2014). Deformation and dynamics of red blood cells in flow through cylindrical microchannels. *Soft Matter*, 10(24):4258–4267.

[Feng and Michaelides, 2004] Feng, Z.-G. and Michaelides, E. E. (2004). The immersed boundary-lattice boltzmann method for solving fluid–particles interaction problems. *J. Comput. Phys.*, 195(2):602–628.

[Fischer and Korzeniewski, 2013] Fischer, T. M. and Korzeniewski, R. (2013). Threshold shear stress for the transition between tumbling and tank-treading of red blood cells in shear flow: dependence on the viscosity of the suspending medium. *J. Fluid Mech.*, 736:351–365.

[Fischer et al., 1978a] Fischer, T. M., Stohr-Lissen, M., and Schmid-Schonbein, H. (1978a). The red cell as a fluid droplet: tank tread-like motion of the human erythrocyte membrane in shear flow. *Science*, 202(4370):894–896.

[Fischer et al., 1978b] Fischer, T. M., Stohr-Lissen, M., and Schmid-Schonbein, H. (1978b). The red cell as a fluid droplet: tank tread-like motion of the human erythrocyte membrane in shear flow. *Science*, 202(4370):894–896.

[Flormann, 2017] Flormann, D. A. D. (2017). *La caractérisation physique de l'agrégation des globules rouges*. PhD thesis, Grenoble Alpes.

[Forsyth et al., 2011] Forsyth, A. M., Wan, J., Owrutsky, P. D., Abkarian, M., and Stone, H. A. (2011). Multiscale approach to link red blood cell dynamics, shear viscosity, and atp release. *Proc. Natl. Acad. Sci. USA.*, 108(27):10986–10991.

[Galie et al., 2014] Galie, P. A., Nguyen, D.-H. T., Choi, C. K., Cohen, D. M., Janmey, P. A., and Chen, C. S. (2014). Fluid shear stress threshold regulates angiogenic sprouting. *Proc. Natl. Acad. Sci. USA*, 111(22):7968–7973.

[Gebäck and Heintz, 2014] Gebäck, T. and Heintz, A. (2014). A lattice boltzmann method for the advection-diffusion equation with neumann boundary conditions. *Comm. Comput. Phys.*, 15(2):487–505.

[Gekle, 2016] Gekle, S. (2016). Strongly accelerated margination of active particles in blood flow. *Biophys. J.*, 110(2):514–520.

[Gekle, 2017] Gekle, S. (2017). Dispersion of solute released from a sphere flowing in a microchannel. *J. Fluid Mech*, 819:104–120.

[Ghigliotti et al., 2010] Ghigliotti, G., Biben, T., and Misbah, C. (2010). Rheology of a dilute two-dimensional suspension of vesicles. *J. Fluid Mech*, 653:489–518.

[Gijsen et al., 1999] Gijsen, F. J., van de Vosse, F. N., and Janssen, J. (1999). The influence of the non-newtonian properties of blood on the flow in large arteries: steady flow in a carotid bifurcation model. *J. Biomech.*, 32(6):601–608.

[Gorman et al., 2007] Gorman, M. W., Feigl, E. O., and Buffington, C. W. (2007). Human plasma atp concentration. *Clin. Chem.*, 53(2):318–325.

[Gov and Safran, 2005] Gov, N. S. and Safran, S. A. (2005). Red blood cell membrane fluctuations and shape controlled by atp-induced cytoskeletal defects. *Biophys. J.*, 88(3):1859–1874.

[Guckenberger and Gekle, 2018] Guckenberger, A. and Gekle, S. (2018). A boundary integral method with volume-changing objects for ultrasound-triggered margination of microbubbles. *J. Fluid Mech*, 836:952–997.

[Hariprasad and Secomb, 2015] Hariprasad, D. S. and Secomb, T. W. (2015). Prediction of noninertial focusing of red blood cells in poiseuille flow. *Phys. Rev. E*, 92(3):033008.

[Hartmannsgruber et al., 2007] Hartmannsgruber, V., Heyken, W.-T., Kacik, M., Kaistha, A., Grgic, I., Harteneck, C., Liedtke, W., Hoyer, J., and Köhler, R. (2007). Arterial response to shear stress critically depends on endothelial trpv4 expression. *PloS One*, 2(9):e827.

[He and Luo, 1997] He, X. and Luo, L.-S. (1997). Theory of the lattice boltzmann method: From the boltzmann equation to the lattice boltzmann equation. *Phys. Rev. E*, 56(6):6811.

[Helfrich, 1973] Helfrich, W. (1973). Elastic properties of lipid bilayers: theory and possible experiments. *Z. Naturforsch. C Bio. Sci.*, 28(11-12):693–703.

[Hill et al., 2001] Hill, M. A., Zou, H., Potocnik, S. J., Meininger, G. A., and Davis, M. J. (2001). Invited review: arteriolar smooth muscle mechanotransduction: Ca2+ signaling pathways underlying myogenic reactivity. *Journal of applied physiology*, 91(2):973–983.

[Hoge et al., 1999] Hoge, R. D., Atkinson, J., Gill, B., Crelier, G. R., Marrett, S., and Pike, G. B. (1999). Linear coupling between cerebral blood flow and oxygen consumption in activated human cortex. *Proc. Natl. Acad. Sci. USA*, 96(16):9403–9408.

[Hu et al., 2018] Hu, W.-F., Lai, M.-C., and Misbah, C. (2018). A coupled immersed boundary and immersed interface method for interfacial flows with soluble surfactant. *Comput. Fluids*, 168:201–215.

[Huang et al., 2009] Huang, H., Sugiyama, K., and Takagi, S. (2009). An immersed boundary method for restricted diffusion with permeable interfaces. *J. Comput. Phys*, 228(15):5317–5322.

[Huang et al., 2016] Huang, J., Hu, Z., and Yong, W.-A. (2016). Second-order curved boundary treatments of the lattice boltzmann method for convection–diffusion equations. *J. Comput. Phys*, 310:26–44.

[Huang and Yong, 2015] Huang, J. and Yong, W.-A. (2015). Boundary conditions of the lattice boltzmann method for convection–diffusion equations. *J. Comput. Phys*, 300:70–91.

[Hyakutake and Nagai, 2015] Hyakutake, T. and Nagai, S. (2015). Numerical simulation of red blood cell distributions in three-dimensional microvascular bifurcations. *Microvasc. Res.*, 97:115–123.

[Jafarnejad et al., 2015] Jafarnejad, M., Cromer, W., Kaunas, R., Zhang, S., Zawieja, D., and Moore Jr, J. (2015). Measurement of shear stress-mediated intracellular calcium dynamics in human dermal lymphatic endothelial cells. *Am. J. Physiol. Heart Circ. Physiol.*, 308(7):H697–H706.

[John and Barakat, 2001] John, K. and Barakat, A. I. (2001). Modulation of atp/adp concentration at the endothelial surface by shear stress: effect of flow-induced atp release. *Ann. Biomed. Eng.*, 29(9):740–751.

[Judy et al., 1976] Judy, W. V., Watanabe, A. M., Henry, D. P., Besch Jr, H., Murphy, W. R., and Hockel, G. M. (1976). Sympathetic nerve activity: role in regulation of blood pressure in the spontaenously hypertensive rat. *Circ. Res.*, 38(6):21–29.

[Junk et al., 2005] Junk, M., Klar, A., and Luo, L.-S. (2005). Asymptotic analysis of the lattice boltzmann equation. *J. Comput. Phys*, 210(2):676–704.

[Kabacaoğlu et al., 2017] Kabacaoğlu, G., Quaife, B., and Biros, G. (2017). Quantification of mixing in vesicle suspensions using numerical simulations in two dimensions. *Phys. Fluids*, 29(2):021901.

[Kaoui, 2018] Kaoui, B. (2018). Computer simulations of drug release from a liposome into the bloodstream. *Eur. Phys. J. E*, 41(2):20.

[Kaoui et al., 2009] Kaoui, B., Biros, G., and Misbah, C. (2009). Why do red blood cells have asymmetric shapes even in a symmetric flow? *Phys. Rev. Lett.*, 103(18):188101.

[Kaoui et al., 2018] Kaoui, B., Lauricella, M., and Pontrelli, G. (2018). Mechanistic modelling of drug release from multi-layer capsules. *Comput. Biol. Med.*, 93:149–157.

[Kaoui et al., 2008] Kaoui, B., Ristow, G., Cantat, I., Misbah, C., and Zimmermann, W. (2008). Lateral migration of a two-dimensional vesicle in unbounded poiseuille flow. *Phys. Rev. E*, 77(2):021903.

[Kaoui et al., 2011] Kaoui, B., Tahiri, N., Biben, T., Ez-Zahraouy, H., Benyoussef, A., Biros, G., and Misbah, C. (2011). Complexity of vesicle microcirculation. *Phys. Rev. E*, 84(4):041906.

[Keener and Sneyd, 1998] Keener, J. P. and Sneyd, J. (1998). *Mathematical physiology*, volume 1. Springer.

[Khakh and Burnstock, 2009] Khakh, B. S. and Burnstock, G. (2009). The double life of atp. *Sci. Am.*, 301(6):84–92.

[Koller and Kaley, 1990] Koller, A. and Kaley, G. (1990). Endothelium regulates skeletal muscle microcirculation by a blood flow velocity-sensing mechanism. *Am. J Physiol. Heart Circ. Physiol.*, 258(3):H916–H920.

[Krüger, 2016] Krüger, T. (2016). Effect of tube diameter and capillary number on platelet margination and near-wall dynamics. *Rheol Acta*, 55(6):511–526.

[Krüger et al., 2017] Krüger, T., Kusumaatmaja, H., Kuzmin, A., Shardt, O., Silva, G., and Viggen, E. M. (2017). *The Lattice Boltzmann Method*. Springer.

[Krüger et al., 2009] Krüger, T., Varnik, F., and Raabe, D. (2009). Shear stress in lattice boltzmann simulations. *Phys. Rev. E*, 79(4):046704.

[Kumar and Graham, 2012] Kumar, A. and Graham, M. D. (2012). Mechanism of margination in confined flows of blood and other multicomponent suspensions. *Phys. Rev. Lett*, 109(10):108102.

[Ladd and Verberg, 2001] Ladd, A. J. C. and Verberg, R. (2001). Lattice-boltzmann simulations of particle-fluid suspensions. *J. Stat. Phys.*, 104(5):1191–1251.

[Lallemand and Luo, 2003] Lallemand, P. and Luo, L.-S. (2003). Lattice boltzmann method for moving boundaries. *J. Comput. Phys*, 184(2):406–421.

[Lanotte et al., 2016] Lanotte, L., Mauer, J., Mendez, S., Fedosov, D. A., Fromental, J.-M., Claveria, V., Nicoud, F., Gompper, G., and Abkarian, M. (2016). Red cells' dynamic morphologies govern blood shear thinning under microcirculatory flow conditions. *Proc. Natl. Acad. Sci. USA*, 113(47):13289–13294.

[Lee et al., 2010] Lee, P., Griffith, B. E., and Peskin, C. S. (2010). The immersed boundary method for advection–electrodiffusion with implicit timestepping and local mesh refinement. *J. Comput. Phys*, 229(13):5208–5227.

[Li et al., 2013] Li, L., Mei, R., and Klausner, J. F. (2013). Boundary conditions for thermal lattice boltzmann equation method. *J. Comput. Phys*, 237:366–395.

[Li et al., 2017] Li, L., Mei, R., and Klausner, J. F. (2017). Lattice boltzmann models for the convection-diffusion equation: D2q5 vs d2q9. *International Journal of Heat and Mass Transfer*, 108:41–62.

[Li et al., 2015] Li, L.-F., Xiang, C., and Qin, K.-R. (2015). Modeling of trpv4-c1-mediated calcium signaling in vascular endothelial cells induced by fluid shear stress and atp. *Biomech. Model Mechanobiol.*, 14(5):979–993.

[Liu et al., 1987] Liu, S.-C., Derick, L. H., and Palek, J. (1987). Visualization of the hexagonal lattice in the erythrocyte membrane skeleton. *J. Cell Biol.*, 104(3):527–536.

[Locovei et al., 2006] Locovei, S., Bao, L., and Dahl, G. (2006). Pannexin 1 in erythrocytes: function without a gap. *Proc. Natl. Acad. Sci. USA.*, 103(20):7655–7659.

[Malek et al., 1999] Malek, A. M., Alper, S. L., and Izumo, S. (1999). Hemodynamic shear stress and its role in atherosclerosis. *Jama*, 282(21):2035–2042.

[Markl and Körner, 2015] Markl, M. and Körner, C. (2015). Free surface neumann boundary condition for the advection–diffusion lattice boltzmann method. *J. Comput. Phys.*, 301:230–246.

[Mauer et al., 2018] Mauer, J., Mendez, S., Lanotte, L., Nicoud, F., Abkarian, M., Gompper, G., and Fedosov, D. A. (2018). Flow-induced transitions of red blood cell shapes under shear. *Phys. Rev. Lett.*, 121(11):118103.

[Mohamad, 2011] Mohamad, A. A. (2011). *Lattice Boltzmann method: fundamentals and engineering applications with computer codes*. Springer Science & Business Media.

[Müller et al., 2016] Müller, K., Fedosov, D. A., and Gompper, G. (2016). Understanding particle margination in blood flow–a step toward optimized drug delivery systems. *Med. Eng. Phys.*, 38(1):2–10.

[Needham et al., 2000] Needham, D., Anyarambhatla, G., Kong, G., and Dewhirst, M. W. (2000). A new temperature-sensitive liposome for use with mild hyperthermia: characterization and testing in a human tumor xenograft model. *Cancer Res.*, 60(5):1197–1201.

[Noguchi and Gompper, 2005] Noguchi, H. and Gompper, G. (2005). Shape transitions of fluid vesicles and red blood cells in capillary flows. *Proc. Natl. Acad. Sci. USA*, 102(40):14159–14164.

[Novak and Slepchenko, 2014] Novak, I. L. and Slepchenko, B. M. (2014). A conservative algorithm for parabolic problems in domains with moving boundaries. *J. Comput. Phys*, 270:203–213.

[Olla, 1997] Olla, P. (1997). The lift on a tank-treading ellipsoidal cell in a shear flow. *J. Phys. II*, 7(10):1533–1540.

[Park et al., 2010] Park, Y., Best, C. A., Auth, T., Gov, N. S., Safran, S. A., Popescu, G., Suresh, S., and Feld, M. S. (2010). Metabolic remodeling of the human red blood cell membrane. *Proc. Natl. Acad. Sci. USA*, 107(4):1289–1294.

[Peskin, 2002] Peskin, C. S. (2002). The immersed boundary method. *Acta Numer.*, 11:479–517.

[Plank et al., 2006] Plank, M. J., Wall, D. J., and David, T. (2006). Atherosclerosis and calcium signalling in endothelial cells. *Prog. Biophys. Mol. Biol.*, 91(3):287–313.

[Popel and Johnson, 2005] Popel, A. S. and Johnson, P. C. (2005). Microcirculation and hemorheology. *Annu. Rev. Fluid Mech.*, 37:43–69.

[Pozrikidis, 1992] Pozrikidis, C. (1992). *Boundary integral and singularity methods for linearized viscous flow*. Cambridge University Press.

[Prado et al., 2015] Prado, G., Farutin, A., Misbah, C., and Bureau, L. (2015). Viscoelastic transient of confined red blood cells. *Biophys. J.*, 108(9):2126–2136.

[Pries et al., 1992] Pries, A., Neuhaus, D., and Gaehtgens, P. (1992). Blood viscosity in tube flow: dependence on diameter and hematocrit. *American Journal of Physiology-Heart and Circulatory Physiology*, 263(6):H1770–H1778.

[Pries et al., 1990] Pries, A. R., Secomb, T. W., Gaehtgens, P., and Gross, J. (1990). Blood flow in microvascular networks. *Circ. Res*, 67:826–834.

[Putney et al., 2001] Putney, J. W., Broad, L. M., Braun, F.-J., Lievremont, J.-P., and Bird, G. S. J. (2001). Mechanisms of capacitative calcium entry. *J. Cell Sci.*, 114(12):2223–2229.

[Quaife and Biros, 2014] Quaife, B. and Biros, G. (2014). High-volume fraction simulations of two-dimensional vesicle suspensions. *J. Comput. Phys*, 274:245–267.

[Quint et al., 2017] Quint, S., Christ, A., Guckenberger, A., Himbert, S., Kaestner, L., Gekle, S., and Wagner, C. (2017). 3d tomography of cells in micro-channels. *Appl. Phys. Lett.*, 111(10):103701.

[Rahimian et al., 2010] Rahimian, A., Veerapaneni, S. K., and Biros, G. (2010). Dynamic simulation of locally inextensible vesicles suspended in an arbitrary two-dimensional domain, a boundary integral method. *Journal of Computational Physics*, 229(18):6466–6484.

[Rees et al., 1989] Rees, D., Palmer, R., and Moncada, S. (1989). Role of endothelium-derived nitric oxide in the regulation of blood pressure. *Proc. Natl. Acad. Sci. USA*, 86(9):3375–3378.

[Resnick et al., 2003] Resnick, N., Yahav, H., Shay-Salit, A., Shushy, M., Schubert, S., Zilberman, L. C. M., and Wofovitz, E. (2003). Fluid shear stress and the vascular endothelium: for better and for worse. *Prog. Biophys. Mol. Biol.*, 81(3):177–199.

[Risau, 1997] Risau, W. (1997). Mechanisms of angiogenesis. *Nature*, 386(6626):671.

[Roy and Sherrington, 1890] Roy, C. S. and Sherrington, C. S. (1890). On the regulation of the blood-supply of the brain. *J. Physiol*, 11(1-2):85–158.

[Saotome et al., 2017] Saotome, K., Murthy, S. E., Kefauver, J. M., Whitwam, T., Patapoutian, A., and Ward, A. B. (2017). Structure of the mechanically activated ion channel Piezo1. *Nature*.

[Scheffer et al., 2001] Scheffer, L., Bitler, A., Ben-Jacob, E., and Korenstein, R. (2001). Atomic force pulling: probing the local elasticity of the cell membrane. *Eur. Biophys. J.*, 30(2):83–90.

[Schwartz, 1962] Schwartz, C. J. (1962). Observations on localization of arterial plaques. *Circ. Res.*, pages 63–73.

[Segal, 2005] Segal, S. S. (2005). Regulation of blood flow in the microcirculation. *Microcirculation*, 12(1):33–45.

[Seifert, 1999] Seifert, U. (1999). Hydrodynamic lift on bound vesicles. *Phys. Rev. Lett.*, 83(4):876.

[Sercombe et al., 2015] Sercombe, L., Veerati, T., Moheimani, F., Wu, S. Y., Sood, A. K., and Hua, S. (2015). Advances and challenges of liposome assisted drug delivery. *Front. Pharmacol.*, 6:286.

[Shen et al., 2017a] Shen, Z., Farutin, A., Thiébaud, M., and Misbah, C. (2017a). Interaction and rheology of vesicle suspensions in confined shear flow. *Phys. Rev. Fluids*, 2(10):103101.

[Shen et al., 2017b] Shen, Z., Farutin, A., Thiébaud, M., and Misbah, C. (2017b). Interaction and rheology of vesicle suspensions in confined shear flow. *Phys. Rev. Fluids*, 2:103101.

[Snyder and Sheafor, 1999] Snyder, G. K. and Sheafor, B. A. (1999). Red blood cells: centerpiece in the evolution of the vertebrate circulatory system. *American zoologist*, 39(2):189–198.

[Sprague et al., 1998a] Sprague, R. S., Ellsworth, M. L., Stephenson, A. H., Kleinhenz, M. E., and Lonigro, A. J. (1998a). Deformation-induced atp release from red blood cells requires cftr activity. *Am. J. Physiol. Heart Circ. Physiol.*, 275(5):H1726–H1732.

[Sprague et al., 1998b] Sprague, R. S., Ellsworth, M. L., Stephenson, A. H., Kleinhenz, M. E., and Lonigro, A. J. (1998b). Deformation-induced atp release from red blood cells requires cftr activity. *Am. J. Physiol. Heart Circ. Physiol.*, 275(5):H1726–H1732.

[Sprague et al., 1996] Sprague, R. S., Ellsworth, M. L., Stephenson, A. H., and Lonigro, A. J. (1996). Atp: the red blood cell link to no and local control of the pulmonary circulation. *Am. J. Physiol. Heart Circ. Physiol.*, 271(6):H2717–H2722.

[Subczynski et al., 1992] Subczynski, W. K., Hopwood, L. E., and Hyde, J. S. (1992). Is the mammalian cell plasma membrane a barrier to oxygen transport? *J. Gen. Physiol.*, 100(1):69–87.

[Succi, 2001] Succi, S. (2001). *The lattice Boltzmann equation: for fluid dynamics and beyond*. Oxford university press.

[Suga, 2006] Suga, S. (2006). Numerical schemes obtained from lattice boltzmann equations for advection diffusion equations. *International Journal of Modern Physics C*, 17(11):1563–1577.

[Sutera et al., 1970] Sutera, S., Seshadri, V., Croce, P., and Hochmuth, R. (1970). Capillary blood flow: Ii. deformable model cells in tube flow. *Microvasc. Res.*, 2(4):420–433.

[Tahiri et al., 2013] Tahiri, N., Biben, T., Ez-Zahraouy, H., Benyoussef, A., and Misbah, C. (2013). On the problem of slipper shapes of red blood cells in the microvasculature. *Microvasc. Res.*, 85:40–45.

[Thiébaud and Misbah, 2013] Thiébaud, M. and Misbah, C. (2013). Rheology of a vesicle suspension with finite concentration: A numerical study. *Phys. Rev. E*, 88(6):062707.

[Thiébaud et al., 2014] Thiébaud, M., Shen, Z., Harting, J., and Misbah, C. (2014). Prediction of anomalous blood viscosity in confined shear flow. *Phys. Rev. Lett.*, 112(23):238304.

[Tomaiuolo, 2014] Tomaiuolo, G. (2014). Biomechanical properties of red blood cells in health and disease towards microfluidics. *Biomicrofluidics*, 8(5):051501.

[Topper et al., 1996] Topper, J. N., Cai, J., Falb, D., and Gimbrone, M. A. (1996). Identification of vascular endothelial genes differentially responsive to fluid mechanical stimuli: cyclooxygenase-2, manganese superoxide dismutase, and endothelial cell nitric oxide synthase are selectively up-regulated by steady laminar shear stress. *Proc. Natl. Acad. Sci. USA*, 93(19):10417–10422.

[Topper and Gimbrone Jr, 1999] Topper, J. N. and Gimbrone Jr, M. A. (1999). Blood flow and vascular gene expression: fluid shear stress as a modulator of endothelial phenotype. *Mol. Med. Today*, 5(1):40–46.

[Tran et al., 2000] Tran, Q.-K., Ohashi, K., and Watanabe, H. (2000). Calcium signalling in endothelial cells. *Cardiovasc. Res.*, 48(1):13–22.

[Trozzo et al., 2015] Trozzo, R., Boedec, G., Léonetti, M., and Jaeger, M. (2015). Axisymmetric boundary element method for vesicles in a capillary. *J. Comput. Phys*, 289:62–82.

[Tsubota and Wada, 2010] Tsubota, K.-i. and Wada, S. (2010). Effect of the natural state of an elastic cellular membrane on tank-treading and tumbling motions of a single red blood cell. *Phys. Rev. E*, 81(1):011910.

[Veerapaneni et al., 2009] Veerapaneni, S. K., Gueyffier, D., Zorin, D., and Biros, G. (2009). A boundary integral method for simulating the dynamics of inextensible vesicles suspended in a viscous fluid in 2d. *J. Comput. Phys.*, 228(7):2334–2353.

[Vennemann et al., 2007] Vennemann, P., Lindken, R., and Westerweel, J. (2007). In vivo whole-field blood velocity measurement techniques. *Exp. Fluids*, 42(4):495–511.

[Vlahovska and Gracia, 2007] Vlahovska, P. M. and Gracia, R. S. (2007). Dynamics of a viscous vesicle in linear flows. *Phys. Rev. E*, 75(1):016313.

[Vlahovska et al., 2009] Vlahovska, P. M., Podgorski, T., and Misbah, C. (2009). Vesicles and red blood cells in flow: From individual dynamics to rheology. *Comptes Rendus Phys.*, 10(8):775–789.

[Wan et al., 2008] Wan, J., Ristenpart, W. D., and Stone, H. A. (2008). Dynamics of shear-induced atp release from red blood cells. *Proc. Natl. Acad. Sci. USA.*, 105(43):16432–16437.

[Wiesner et al., 1996] Wiesner, T. F., Berk, B. C., and Nerem, R. M. (1996). A mathematical model of cytosolic calcium dynamics in human umbilical vein endothelial cells. *Am. J Physiol. Cell Physiol.*, 270(5):C1556–C1569.

[Wiesner et al., 1997] Wiesner, T. F., Berk, B. C., and Nerem, R. M. (1997). A mathematical model of the cytosolic-free calcium response in endothelial cells to fluid shear stress. *Proc. Natl. Acad. Sci. USA*, 94(8):3726–3731.

[Yamamoto and Ando, 2011] Yamamoto, K. and Ando, J. (2011). New molecular mechanisms for cardiovascular disease: blood flow sensing mechanism in vascular endothelial cells. *J. Pharmacol. Sci.*, 116(4):323–331.

[Yamamoto et al., 2000] Yamamoto, K., Korenaga, R., Kamiya, A., and Ando, J. (2000). Fluid shear stress activates ca2+ influx into human endothelial cells via p2x4 purinoceptors. *Circ. Res.*, 87(5):385–391.

[Yamamoto et al., 2003] Yamamoto, K., Takahashi, T., Asahara, T., Ohura, N., Sokabe, T., Kamiya, A., and Ando, J. (2003). Proliferation, differentiation, and tube formation by endothelial progenitor cells in response to shear stress. *J. Appl. Physiol.*, 95(5):2081–2088.

[Yang et al., 2009] Yang, X., Zhang, X., Li, Z., and He, G.-W. (2009). A smoothing technique for discrete delta functions with application to immersed boundary method in moving boundary simulations. *J. Comput. Phys*, 228(20):7821–7836.

[Yin et al., 2012] Yin, X., Le, G., and Zhang, J. (2012). Mass and momentum transfer across solid-fluid boundaries in the lattice-boltzmann method. *Phys. Rev. E*, 86(2):026701.

[Yoshida and Nagaoka, 2010] Yoshida, H. and Nagaoka, M. (2010). Multiple-relaxation-time lattice boltzmann model for the convection and anisotropic diffusion equation. *J. Comput. Phys*, 229(20):7774–7795.

[Zawieja, 2005] Zawieja, D. (2005). Lymphatic biology and the microcirculation: past, present and future. *Microcirculation*, 12(1):141–150.

[Zhang and Misbah, 2018] Zhang, H. and Misbah, C. (2018). Lattice boltzmann simulation of advection-diffusion of chemicals and applications to blood flow: submitted in 2018. *Phys. Rev. E.*

[Zhang et al., 2018] Zhang, H., Shen, Z., Hogan, B., Barakat, A. I., and Misbah, C. (2018). Atp release by red blood cells under flow: Model and simulations: Submitted. *Biophys. J.*

[Zhang et al., 2012] Zhang, T., Shi, B., Guo, Z., Chai, Z., and Lu, J. (2012). General bounce-back scheme for concentration boundary condition in the lattice-boltzmann method. *Phys. Rev. E*, 85(1):016701.

[Zhao et al., 2012] Zhao, H., Shaqfeh, E. S., and Narsimhan, V. (2012). Shear-induced particle migration and margination in a cellular suspension. *Phys. Fluids*, 24(1):011902.

[Zhong-Can and Helfrich, 1989] Zhong-Can, O.-Y. and Helfrich, W. (1989). Bending energy of vesicle membranes: General expressions for the first, second, and third variation of the shape energy and applications to spheres and cylinders. *Phys. Rev. A*, 39(10):5280.

[Zou and He, 1997] Zou, Q. and He, X. (1997). On pressure and velocity boundary conditions for the lattice boltzmann bgk model. *Phys. Fluids*, 9(6):1591–1598.